ABSTRACT

COLLOIDAL QUANTUM DOT (CQD) BASED MID-WAVELENGTH INFRARED OPTOELECTRONICS

By
Shihab Bin Hafiz

Colloidal quantum dot (CQD) photodetectors are a rapidly emerging technology with a potential to significantly impact today's infrared sensing and imaging technologies. To date, CQD photodetector research is primarily focused on lead-chalcogenide semiconductor CQDs which have spectral response fundamentally limited by the bulk bandgap of the constituent material, confining their applications to near-infrared (NIR, 0.7-1.0 um) and short-wavelength infrared (SWIR, 1-2.5 um) spectral regions. The overall goal of this dissertation is to investigate a new generation of CQD materials and devices that advances the current CQD photodetector research toward the technologically important thermal infrared region of 3-5 μm, known as mid-wavelength infrared (MWIR).

In this dissertation, electronic and optoelectronic characteristics of Ag_2Se CQD based devices are analyzed by different device architectures with detailed analysis of detector performance parameters. The first part of the dissertation includes the report on the fabrication of solution-processed lateral photoconductive photodetectors. Significant photoresponse is demonstrated in MWIR with the lateral photoconductor at room temperature. The detailed analysis on the effect of ligand exchange as well as temperature and spectral dependent photoresponses is presented.

In the second device structure, vertically stacked quantum dot devices are demonstrated. In this device architecture, a barrier QD layer is placed in between mid-wavelength absorber intraband Ag_2Se QD layer. The insertion of barrier layer reduces dark

current significantly since $1S_e$ Ag_2Se QD-$1S_e$ PbS QD conduction offset serves as a potential barrier, blocking the transport of thermally generated electrons and holes. In addition, vertical device design improves detector performance parameters significantly at room temperature.

At the last part of the dissertation, development of p-n heterojunction diode devices is presented as third device structure. High performance detectors can be realized using a traditional p-n junction device design, however, the heavily-doped nature of intraband quantum dots present a new challenge in realizing diode devices. To address this challenge, an unique trait of blending two different QDs is employed to control electrical property. The fabricated p-n junction devices demonstrate reduced noise current density due to reverse bias operation, which shows improvement in the specific detectivity of the detector at room temperature.

Consequently, this dissertation presents the feasibility of uncooled, room-temperature photodetection in the MWIR with intraband silver selenide quantum dots that has the potential to impact numerous applications ranging from all-weather night vision, machine vision, biomedical imaging, to free-space optical communication.

COLLOIDAL QUANTUM DOT (CQD) BASED MID-WAVELENGTH INFRARED OPTOELECTRONICS

by
Shihab Bin Hafiz

A Dissertation
Submitted to the Faculty of
New Jersey Institute of Technology
in Partial Fulfillment of the Requirements for the Degree of
Doctor of Philosophy in Electrical Engineering

Helen and John C. Hartmann Department of
Electrical and Computer Engineering

August 2021

APPROVAL PAGE

COLLOIDAL QUANTUM DOT (CQD) BASED MID-WAVELENGTH INFRARED OPTOELECTRONICS

Shihab Bin Hafiz

Dr. Dong-Kyun Ko, Dissertation Advisor — Date
Associate Professor of Electrical and Computer Engineering, NJIT

Dr. Leonid Tsybeskov, Committee Member — Date
Distinguished Professor of Electrical and Computer Engineering, NJIT

Dr. Haim Grebel, Committee Member — Date
Professor of Electrical and Computer Engineering, NJIT

Dr. Hieu Pham Trung Nguyen, Committee Member — Date
Associate Professor of Electrical and Computer Engineering, NJIT

Dr. Ayaskanta Sahu, Committee Member — Date
Assistant Professor of Chemical and Biomolecular Engineering,
New York University, Brooklyn, NY

BIOGRAPHICAL SKETCH

Author: Shihab Bin Hafiz

Degree: Doctor of Philosophy

Date: August 2021

Undergraduate and Graduate Education:

- Doctor of Philosophy in Electrical Engineering,
  New Jersey Institute of Technology, Newark, NJ, 2021
- Master of Science in Nanoengineering,
  North Carolina A&T State University, Greensboro, NC, 2017
- Bachelor of Science in Electrical & Electronic Engineering,
  Bangladesh University of Engineering & Technology, Dhaka, Bangladesh, 2014

Major: Electrical Engineering

Presentations and Publications:

Journal Articles:

S. B. Hafiz, M. R. Scimeca, P. Zhao, I. J. Paredes, A. Sahu and D.-K. Ko, "Silver selenide colloidal quantum dots for mid-wavelength infrared photodetection," *ACS Applied Nano Materials*, vol. 2, no. 3, pp.1631-1636, 2019.

S. B. Hafiz, M. R. Scimeca, A. Sahu and D.-K. Ko, "Colloidal quantum dots for thermal infrared sensing and imaging," *Nano Convergence*, vol. 6, no. 7, pp. 1-22, 2019.

S. B. Hafiz, M. M. A. Mahfuz, M. R. Scimeca, S. Lee, S. J. Oh, A. Sahu and D.-K. Ko, "Ligand engineering of mid-infrared Ag_2Se colloidal quantum dots," *Physica E: Low-dimensional Systems and Nanostructure*s, vol. 124, pp. 114223, 2020.

S. B. Hafiz, M. M. A. Mahfuz and D.-K. Ko, "Vertically-stacked intraband quantum dot devices for mid-wavelength infrared photodetection*," ACS Applied Materials and Interfaces*, vol. 13, no. 1, pp. 937-943, 2020.

S. B. Hafiz, M. M. A. Mahfuz, S. Lee and D.-K. Ko "Mid-wavelength infrared p-n heterojunction diodes based on intraband colloidal quantum dots," submitted to *ACS Applied Materials and Interfaces* 2021.

M. S. Shawkat, S. B. Hafiz, M M. Islam, S. A. Mofid, M. M. A. Mahfuz, A. Biswas, H.-S. Chung, E. Okogbue, T.-J. Ko, D. Chanda, T. Roy, D.-K. Ko and Y. Jung, "Scalable van der waals two-dimensional PtTe2 layers integrated onto silicon for efficient near-to-mid infrared photodetection," *ACS Applied Materials and Interfaces*, vol. 13, no. 13, pp. 15542–15550, 2021.

L. Tsybeskov, M. Alam, S. B. Hafiz, D.-K., Ko,A. M. Bratkovsky, X. Wu and D. J. Lockwood, "Photoluminescence in PbS nanocrystal thin films: nanocrystal density, film morphology and energy transfer," *Journal of Applied Physics*, vol. 128, pp.134301, 2020.

N. Chen, M. R. Scimeca, S. J. Paul, S. B. Hafiz, Z. Yang, X. Liu, F. Yang, D.-K. Ko and A. Sahu, "High-performance thermoelectric silver selenide thin films cation exchanged from a copper selenide template," *Nanoscale Advances*, vol. **2**, pp. 368-376, 2019.

M. A. Hossain, S. Jeon, J. Ahn, J. Bang, H. K. Woo, S. B. Hafiz, D.-K. Ko and S. J. Oh, "Property engineering through nanomaterial chemical transformation of colloidal nanocrystal thin films," *Applied Surface Science* vol. 513, pp.145721, 2020.

T.-J. Ko, S. B. Han, E. Okogbue, M. S. Shawkat, M. Wang, J. Ma, T. S. Bae, S. B. Hafiz, D.-K. Ko, H.-S. Chung, K. H. Oh and Y. Jung, "Wafer-scale 2D PtTe2 layers-enabled kirigami heaters with superior mechanical stretchability and electro-thermal responsiveness," *Applied Materials Today*, vol. 20, pp.100718, 2020.

Conference Papers:

S. B. Hafiz, M. R. Scimeca, A. Sahu and D.-K. Ko "Mid-infrared colloidal quantum dot based nanoelectronics and nano-optoelectronics," *ECE Transactions* vol. 92, no. 1, pp. 11-16, 2019.

S. B. Hafiz, M. M. A. Mahfuz and D.-K. Ko, "Mid-wavelength infrared responsivity of colloidal quantum dot/organic hybrid photodetectors," *ECS Transactions*, vol. 97, no. 1, pp. 109-115, 2020.

S. B. Hafiz, M. M. A. Mahfuz and D.-K. Ko, "Intraband quantum dot barrier devices-optimization of energy level alignment," *ECS Transactions*, vol. 102, no. 1, pp. 45-51, 2021.

To my parents, Hafizur Rahman and Mahmuda Hafiz,
who encouraged and supported me all the way.

ACKNOWLEDGMENT

Foremost, I would like to express my deepest gratitude to my wonderful advisor, Dr. Dong-Kyun Ko, for his continuous support and guidance throughout my doctoral research. From the beginning of my time at New Jersey Institute of Technology, Dr. Ko showed patience, kindness, and encouragement towards me. He is an extremely supportive, passionate, and dedicated advisor that I could not have asked for more. He always supported me to explore new ideas and used to give guidance until I get one. I will always remember how dedicated he was with my research that he used to check on my updates almost every day in a week. This dissertation would not have been possible without his dedication and support. It is an honor for me to have been his student.

I would like to thank the rest of the dissertation committee members: Dr. Leonid Tsybeskov, Dr. Haim Grebel, Dr. Hieu Pham Trung Nguyen and Dr. Ayaskanta Sahu, for their valuable comments and suggestions.

I am thankful to Mohammad Mostafa Al Mahfuz for being a research colleague and a good friend during my time at Nanoelectronic Materials and Devices (NMD) lab.

I would like to acknowledge the Department of Electrical and Computer Engineering for providing teaching assistantship during my first year of doctoral study. I would like to thank National Science Foundation (Award No. 1809112) and Global Research Outreach program of Samsung Advanced Institute of Technology for funding.

Finally, my heartfelt thanks to my elder brother Abdullah Al Mamun for being always with me. I want to thank my parents, Hafizur Rahman and Mahmuda Hafiz, my wife, Sabrina Haque Jitu, other family members for their continuous support and

encouragement. Last but not least, I am grateful to the Almighty God for being with me all the way.

TABLE OF CONTENTS

TABLE OF CONTENTS
(Continued)

Chapter **Page**

TABLE OF CONTENTS
(Continued)

Chapter **Page**

TABLE OF CONTENTS
(Continued)

Chapter **Page**

LIST OF TABLES

LIST OF FIGURES

LIST OF FIGURES
(Continued)

Figure **Page**

LIST OF FIGURES
(Continued)

Figures **Page**

LIST OF FIGURES
(Continued)

LIST OF FIGURES
(Continued)

Figure **Page**

LIST OF FIGURES
(Continued)

Figure **Page**

LIST OF FIGURES
(Continued)

Figure **Page**

CHAPTER 1

INTRODUCTION

1.1 Infrared Spectral Range and its Applications

Discovery of infrared radiation (IR) by William Herschel extended our vison ability, which had been limited to the visible wavelength range [1]. Continuous investigation over the past 200 years has developed our deeper knowledge into the infrared and various infrared detectors have been developed to move our vision ability beyond the visible wavelength range.

In the early 20^{th} century, research in infrared technology advanced to a new dimension when military showed interest into infrared detection and imaging. Currently, infrared technology is finding different civilian applications in commercial, industrial, environmental, and communication sectors.

The infrared radiation is longer than visible light but shorter than radio waves having wavelength range from 800 nm to 100 μm. According to atmospheric transmission window, the infrared range is further subdivided into different regions: near-infrared (NIR: 0.8 μm - 1 μm), short-wave infrared (SWIR: 1 μm - 2.5 μm), mid-wave infrared (MWIR: 3 μm - 5 μm), long-wave infrared (LWIR: 8 μm - 12 μm) and far-infrared (FIR: 12 μm - 100 μm) [2, 3]. Figure 1.1 shows the infrared spectrum depicting the wavelength range.

The near-infrared (NIR) spectral window extends from 0.8 μm to 1 μm, which has applications in power generation, biomedical instrumentation, and remote sensing technology. Near infrared range in conjunction with visible wavelength range has solar cell application for power generation [4]. In biomedical instrumentation, pulse oximeter utilizes

a combination of near infrared (940 nm) and red LED to measure oxygen saturation in blood [5]. Self-driving vehicle utilizes light detection and ranging (LIDAR) technology as a remote sensing method, which typically operates in near infrared wavelength range [6]. In addition, near infrared has interest in biology and laser technology.

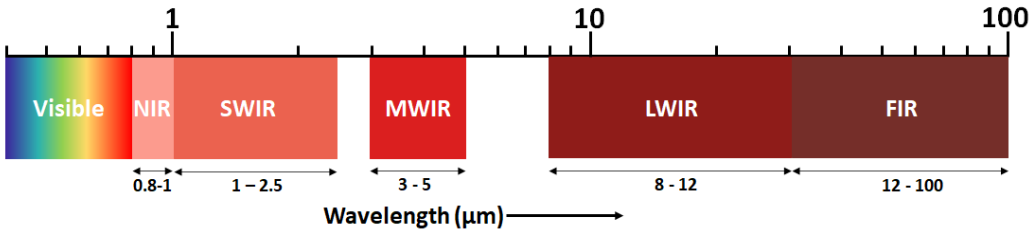

Figure 1.1 Illustration of different subdivisions of infrared spectral wavelength range. *Source:* [2, 3].

The short-wave infrared (SWIR) ranges from 1 µm to 2.5 µm. SWIR allows active imaging using external illumination source like visible wavelength range, where objects and bodies reflect light and act as secondary source. Additionally, the wavelength is longer in this spectral range compared to visible wavelength, which can penetrate through airborne obscurants such as smoke, mist, and fog. This spectral window also offers low dispersion and transmission loss for telecommunication applications at 1.3 µm and 1.55 µm [7].

The mid-wave infrared (MWIR) ranges in the atmospheric transmission window from 3 µm to 5 µm, which is depicted in Figure 1.2a. MWIR allows thermal or passive imaging without the need of using external illumination source like visible wavelength range or SWIR. Instead of utilizing reflection of secondary sources, MWIR detects black body emission of objects and bodies for thermal or passive imaging. The intensity of blackbody emission for an object is represented by Planck's law:

$$B\ (\lambda, T) = \frac{2hc^2}{\lambda^5} \frac{1}{e^{(\frac{hc}{\lambda kT})} - 1} \tag{1.1}$$

where *B (λ, T)* is the spectral irradiance in W.m^{-2} μm^{-1}, *h* is the Planck's constant, *c* is the speed of light, *λ* is the wavelength, *k* is the Boltzmann constant and *T* is the temperature.

Figure 1.2b shows that MWIR is more suited to detect emission of hot objects (500 K) than room temperature objects. MWIR has been traditionally used for military surveillance are finding growing number of applications in commercial, biomedical, and environmental applications.

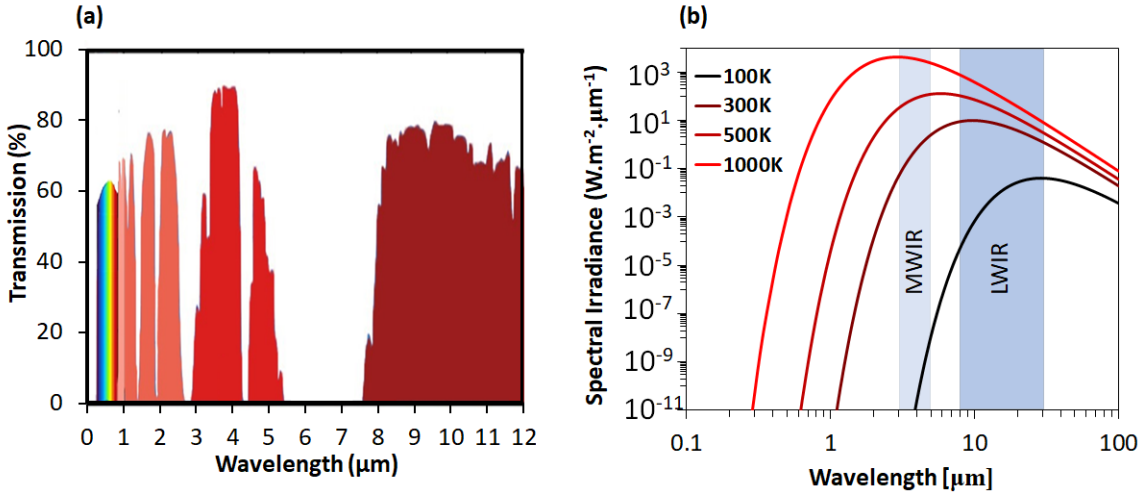

Figure 1.2 (a) Atmospheric transmission of the MWIR and LWIR spectral range for thermal imaging. (b) Spectral irradiance of blackbody at different temperatures.

The long-wave infrared (LWIR) ranges from 8 μm to 12 μm, which is particularly effective in detecting the human body as our body emission (300 K) has its Plank distribution maximum around 9 μm depicted in Figure 1.2b. The far-infrared (FIR) spectral window (12 μm - 100 μm) is used in astronomical applications as cold objects (<140 K) emit radiation in this wavelength range [8].

1.2 Emergence of Colloidal Quantum Dot

1.2.1 Quantum Confinement and Spectral Tunability of Colloidal Quantum Dot

Colloidal quantum dots (CQDs) have emerged as promising optoelectronic materials in recent years [9, 10]. The important property of CQD is that they exhibit tunable optical property due to size dependent quantum confinement. Colloidal quantum dots are strongly confined nanocrystals with diameters smaller than their exciton Bohr radius, which is represented by [11]:

$$a_0 = \frac{4\pi\epsilon_0\epsilon_r\hbar^2}{m_0 m_{eh}^* e^2} \tag{1.2}$$

where ϵ_0 is the permittivity of free space, ϵ_r is the dielectric constant of the material, ħ is the reduced planck constant, m_0 is the rest mass of an electron, $m_{eh}^* = m_e m_h/(m_e + m_h)$ is the reduced mass of electron and hole, and e is the elementary charge.

In a semiconductor material, incident photon can generate electron-hole pair, which is bonded by electrostatic Coulomb force, is known as exciton. The average distance between the photo-induced bound electron-hole pair is known as exciton Bohr radius. When the size of the quantum dot is smaller than the exciton Bohr radius, exciton can be considered as a particle in a box, creating discrete energy states.

In this model, these discrete states can be described quantitatively by using effective mass approximation [12], where the wavefunction of the quantum dot can be represented as a product of Bloch wavefunction and an envelope wavefunction. By considering a

spherical quantum dot of radius R ($R<a_0$), the envelope wavefunction can be derived, with spherical Bessel function (j_L) as one of its components. The discrete energies are represented by:

$$E_{n,L} = \frac{\hbar^2 \phi_{n,L}^2}{2m^* R^2} \tag{1.3}$$

where $\phi_{n,L}$ is the nth root of the spherical Bessel function of the Lth order, m^* is the effective electron and hole mass for conduction and valence band, respectively. Hence, the energy difference between first conduction band ($1S_e$) and valence band ($1S_h$) states determines the bandgap of the quantum dot, and it can be represented by:

$$E_{g,QD} = E_{g,bulk} + \frac{\hbar^2 \pi^2}{2m_e^* R^2} + \frac{\hbar^2 \pi^2}{2m_h^* R^2} = E_{g,bulk} + \frac{\hbar^2 \pi^2}{2m_{eh}^* R^2} \tag{1.4}$$

where, $E_{g,QD}$ is the bandgap of the quantum dot and $E_{g,bulk}$ is the bulk bandgap of the parent material. The difference between the QD band gap and the bulk bandgap is known as the confinement energy ($E_C = \hbar^2 \pi^2 / 2m_{eh}^* R^2$), where the confinement energy increases with decreasing QD size as a function of R^{-2}. The confinement energy also depends on electron and hole effective mass. Generally, the hole effective mass is greater than the electron effective mass. Hence, dispersion of the energy levels in the conduction band are higher than the valence band.

As an example, bulk PbS has an exciton Bohr radius of ~21 nm [13]. When the crystal size of PbS reduces to less than the exciton Bohr radius, strong confinement of both

the electron and hole wavefunctions takes place, which gives rise to discrete quantized energy states. Eventually, this quantum confinement effect results in size dependent optoelectronic properties in PbS quantum dot [14]. Figure 1.3 shows discrete energy states in quantum dot and tunable optical property in PbS quantum dot [15]. This tunable optical property has enabled various optoelectronic devices to date, including solar cells, photodetectors, and light-emitting diodes (LEDs).

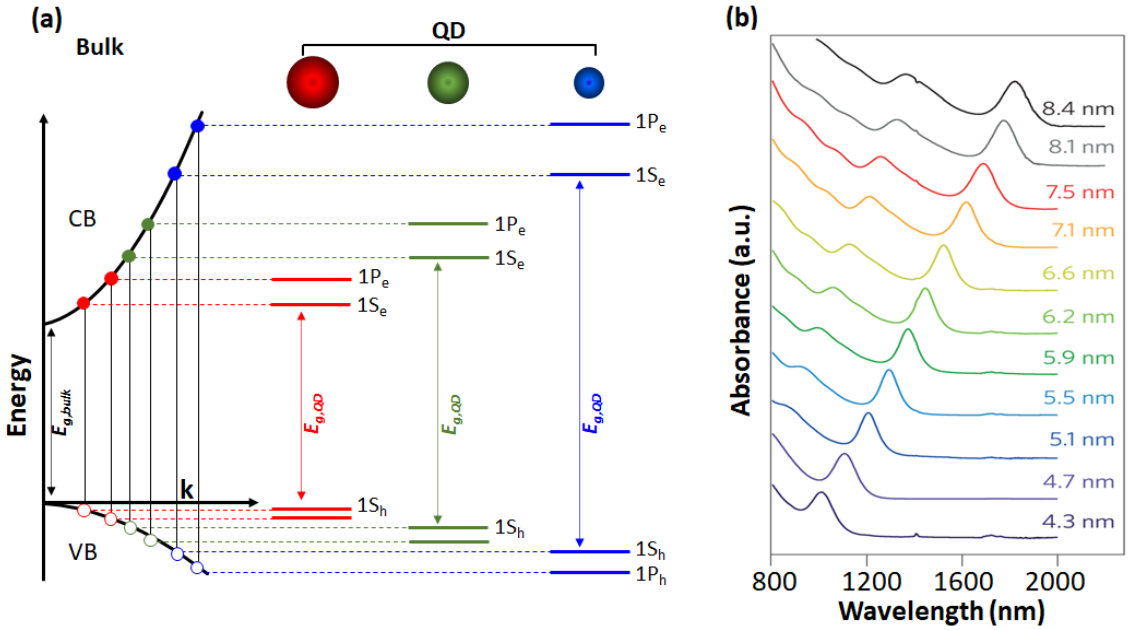

Figure 1.3 Spectral tunability of the colloidal quantum dot. (a) Compared to continuous energy bands of a bulk semiconductor, quantum dot of the same material exhibits discrete energy levels with increased bandgap due to size dependent quantum confinement. (b) Size dependent absorption spectra of PbS quantum dot.
Source: [12, 15].

1.2.2 Prospect of Colloidal Quantum Dot-Based Optoelectronics in Infrared Technologies

Optoelectronics engineered from colloidal quantum dots (CQDs) benefit from greatly simplified device fabrication procedure with dramatic reduction in cost compared to traditional bulk semiconductor devices [10]. The impact that CQD-based devices would bring is expected to be significant especially in the area of infrared sensing and imaging

which are currently dominated by epitaxial semiconductor technologies [16, 17, 18]. For example, HgCdTe has been a golden standard material for fabricating imaging chips, known as focal plane arrays (FPAs), operating in the mid-wavelength infrared (MWIR, 3-5 um) and long-wavelength infrared (LWIR, 8-14 um) spectral regions. However, despite its maturity, HgCdTe FPAs suffer from high cost of device-quality material growth and low FPA manufacturability. HgCdTe is a weakly bonded II-VI compound with high Hg vapor pressure making compositionally-uniform growth extremely difficult; in Hg1-xCdxTe, a 0.001 variation in the composition **x** is known to drastically change the spectral response [19]. In addition, HgCdTe have a large lattice mismatch with silicon and require high processing temperatures making it incompatible with silicon readout integrated circuit (ROIC). This has forced manufacturers to fabricate FPAs from two separate wafers, one bearing photodiodes and the other containing silicon ROIC, which are physically bonded (hybridized) together via indium bumps [20].Figure 1.4 shows a typical indium bump bonding process to bond photodiode array and silicon ROIC platform [21]. The complexity of multiple production steps simultaneously reduces yield and increases overall cost. Furthermore, the cryogenic cooling required in many infrared materials necessitate the use of Joule-Thompson cryostats and Stirling cycle coolers which are costly to implement, require high input power, and significantly increase the size and weight of the detector that limits their applicability.

Infrared CQD based photodetector can provide attractive solutions to overcome these limitations. Spectral response can be tuned simply by adjusting the CQD size and monolithic fabrication of FPA can be readily achieved via solution processing of CQDs ,compatible with a wide range of substrates, including silicon, thus enabling direct

integration with read-out electronic platforms for completing an imaging array [22] without the need of indium bump bonding. Recent study has achieved high performance with CQD based devices in infrared region. As an example, short-wavelength infrared (SWIR, 1–2.5 μm) photodiodes based on PbS CQD have achieved high detectivities of D*> 10^{12} Jones at room temperature which is comparable to commercial InGaAs detectors [22, 23, 24]. Recent demonstration of low-cost SWIR and MWIR imaging [25, 26] have heightened the interest in this new class of CQD-based FPAs and it is envisioned that the successful implementation of infrared CQD photodetector technology may parallel the broad impact brought by low-cost complementary metal-oxide-semiconductor (CMOS) visible cameras that are ubiquitously used today.

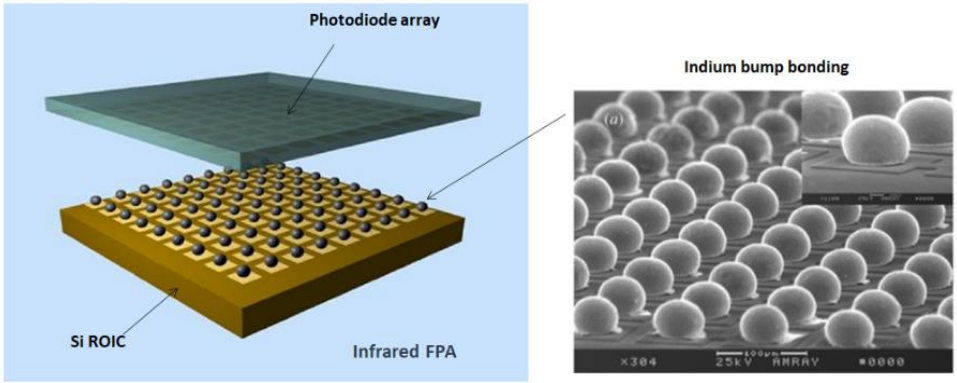

Figure 1.4 Indium bump bonding process involving photodiode array and silicon ROIC platform.
Source: [21].

1.3 Technological Advantage of CQD-Based Mid-Wavelength Infrared Photodetectors

The technological advantage of extending the spectral response toward longer thermal infrared lies in the fact that detectors do not require an illumination source for imaging (passive imaging) and have the ability to see through airborne obscurants such as smoke, mist, and fog [27]. Figure 1.5 shows a good example of MWIR imager's ability to provide

a clear image of the scene inside a smoke-filled tunnel compared to other wavelength range. An image obtained from a visible camera is completely clouded by smoke, whereas short wavelength infrared (SWIR) camera shows a reduced susceptibility to smoke but requires directed illumination to image distant objects in the scene. An MWIR camera does not need directed illumination and can effectively identify cars and human bodies through a smoke-filled tunnel utilizing thermal infrared.

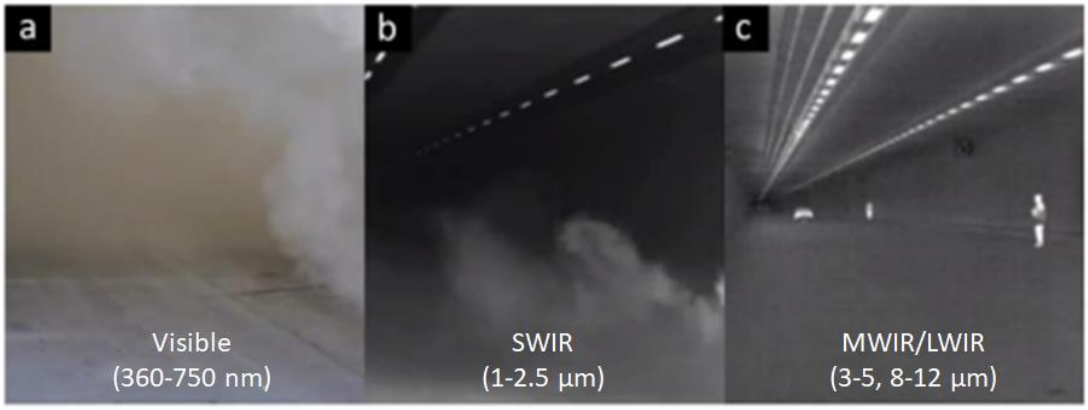

Figure 1.5 Imaging inside the tunnel filled with smoke using (a) visible, (b) SWIR, and (c) MWIR/LWIR cameras.
Source: [28].

These make thermal infrared detectors highly suited for first-responder and search-and-rescue, night driving, machine vision, and poor weather surveillance applications that require capabilities unmet by visible, NIR or SWIR spectral window. Other applications include industrial process control and preventive maintenance, environmental monitoring of hazardous chemicals [29], non-invasive measurements of temperature for tumor and blood flow [30], as well as free-space optical communications [31].

1.4 Current State of the Field

The majority of the infrared colloidal quantum dot research has been focused on lead chalcogenides: Pb (S, Se, Te). To extend the spectral response toward the longer infrared

wavelengths, narrower bandgap material is required. In this regard, CQDs derived from zero bandgap HgTe exhibiting quantum confinement-induced interband transition [32, 33] and self-doped HgSe CQDs allowing intraband transition [34, 35] are being investigated in mid wavelength infrared in recent years, as detailed in the following section.

1.4.1 HgTe CQD-Based Devices : Photoconductive Devices

HgTe is a semimetal and have the prospect of covering a large portion of the infrared spectrum through size-dependent quantum confinement when they are synthesized into CQDs. Currently, HgTe CQD is the only known colloidal nanomaterial that have been used to successfully demonstrate thermal infrared devices based on *interband* optical transition. The first MWIR photoconductive photodetector was reported by Guyot-Sionnest group [36]. The devices were fabricated by simply drop-casting HgTe CQDs on interdigitated electrodes and the as-deposited CQD film readily showed high electrical conductivity without ligand exchange due to CQD aggregation (Figure 1.6). Detailed characterizations [37] have shown that CQD films exhibit a property reminiscence of an intrinsic semiconductor with high carrier mobility around 0.5 cm^2/Vs and show efficient charge separation upon optical generation, supporting the observed high responsivity. The room temperature responsivity was reported to exceed 100 mA/W (10 V bias) for HgTe CQDs having 6 μm absorption cut-off and the highest specific detectivity of 2×10^9 Jones was obtained at 130 K (1KHz) with noise observed to be dominated by 1/f noise with large Hooge's parameter (α_H). The response time was below 100 ns, which is faster than required for imaging application. These works were followed by improving the colloidal synthesis to obtain CQDs with better size dispersion and colloidal stability [38]. The reduced aggregation implies that the CQD films now need to be ligand exchanged for efficient

carrier transport after film deposition. The HgTe CQD films ligand-exchanged with traditional organic ligands were investigated to have low carrier mobility (~ 10^{-4} cm^2/Vs) and showed degradation upon air exposure, such as the disappearance of intrinsic-like property, high dark current and slow photoresponse [39]. A proven strategy developed in CQD electronics to improve the carrier mobility is to employ inorganic-based ligands and this approach has been successfully applied MWIR CQD photodetectors as well. HgTe CQD film ligand-exchanged with As_2S_3-based ligands exhibited higher mobility than organic ligands, greater air stability, and ultimately lead to 30 times improvement in the detectivity (10^{10} Jones, 1 kHz, 230 K, CQDs with 3.5 μm absorption peak) compared to that of the aggregated CQDs, as shown in Figure 1.7 [39, 40]. As_2S_3 also have high transparency in the MWIR, making it a good candidate among other choices of inorganic ligands whereas typical organic ligands have strong vibrational modes in this wavelength range. Reducing the quantum confinement in HgTe CQD by increasing the size would enable photodetection in the LWIR. Indeed, with the advance in colloidal synthesis, photoconductive detectors employing ~ 20 nm HgTe CQDs have successfully demonstrated photoresponse extending up to 12 μm [32].

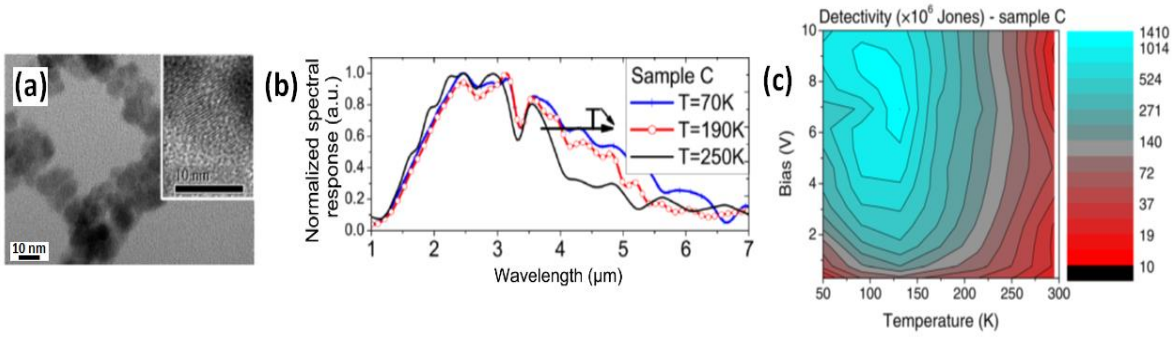

Figure 1.6 HgTe CQD-based photoconductive devices. (a) A TEM image of aggregated HgTe CQDs (6 μm absorption cut-offs) that was used to demonstrate photoconductive devices. Inset shows a high-resolution TEM image of a single CQD. (b) Normalized spectral response of these devices measured at varying temperatures. (c) The map of the specific detectivity measured as a function of temperature and applied bias.
Source: [37].

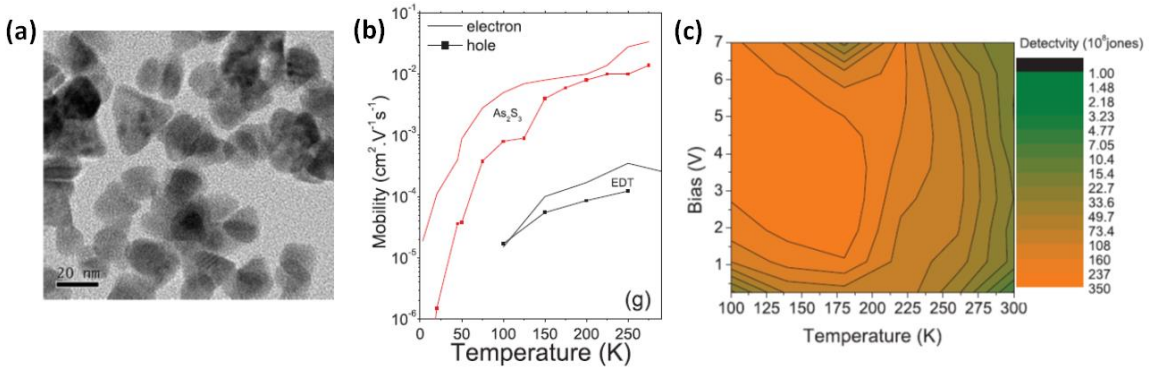

Figure 1.7 Photoconductive device based on HgTe CQDs prepared via improved synthesis. (a) A TEM image of HgTe CQDs prepared through improved synthesis method, showing reduced aggregation. (b) A plot of carrier mobility as a function of temperature obtained from CQD film ligand exchanged with inorganic As_2S_3-based ligand and traditional organic (ethanedithiol, EDT) ligand. (c) The map of detectivity (1 KHz) plotted against bias and temperature for 3 μm absorption cut-offs HgTe CQD device treated with As_2S_3-based ligand.
Source: [39, 40].

By leveraging the broad spectral tunability offer by HgTe CQDs, fabrication of 12 x 12 multicolor pixel detector on a single chip was demonstrated through poly(methyl methacrylate)-assisted transfer technique. Three different sizes of HgTe CQDs having absorption cutoff at 4.8, 6, and 9.5 μm were used to fabricate 200 x 200 μm pixel elements and the responsivities of all three pixels were reported to yield tens of mA/W across each

targeted infrared regions under room temperature operation [41]. This was further extended to a four-color detector, operating between 2 – 5 μm, with room temperature detectivity of four pixels reaching 10^9 Jones, which was also demonstrated on flexible polyethylene terephthalate (PET) substrates [42]. The first demonstration of MWIR imaging via HgTe CQD-based FPAs fabricated by solution-processing of CQDs on commodity ROIC were reported in 2016 [43]. Even with under-optimized CQD layer thickness and lack of anti-reflection coating, the mean detectivity at 95 K was reported to reach 10^9 Jones with noise equivalent differential temperature (NEDT) of 2.3 K. A feasibly of imaging in the LWIR using prototype HgTe CQD FPAs was also reported recently [44]. One promising strategy to increase the photoresponse of existing CQD devices is to enhance the optical absorption using optical nano-antenna. Predesigned gold nano-antenna arrays were patterned on the substrate prior to completing the photoconductive CQD device fabrication, which resulted in 3 times increase in the photocurrent compared to the one without antennas [45].

The HgTe CQDs are of high interest in both fundamental and practical aspects as its infrared optical property arises from quantum confinement of semimetallic bulk that has inverted band structure. As the research progresses, deeper understanding of the electronic fine structures are emerging which encourages a path toward precise engineering of CQD size, shape and surface for further device improvements and optimization [46].

1.4.2 HgTe CQD-Based Devices : Schottky Diode and p-n Heterojunction Diode Devices

The specific detectivity of an HgTe photoconductive device can be greatly improved by reducing the 1/f noise. The 1/f electrical noise component can be minimized if the photodetector operates in zero-bias photovoltaic mode as the dark current approaches zero. A Schottky diode fabricated by depositing Ag top contact on to ethanedithiol/HCl ligand-

exchanged HgTe CQD film have been demonstrated to show high response (~ 80 mA/W), attributed to the shorter carrier transport distance compared to that of the previous photoconductive devices, and the absence of 1/f noise, which ultimately led to higher detectivity of 10^{10} Jones at 140 K [33]. In these devices, the possibility that the rectifying junction may have been formed by Ag-diffused p-type HgTe and intrinsic HgTe CQD layers has been discussed. Higher device performance was observed when Ag_2Te CQD layer was added in between the intrinsic HgTe CQD layer and Ag contact. At 90K, this device exhibited a detectivity of 4 x 10^{10} Jones with photoresponse cut-off at 5.25 μm. Further analysis revealed that, at this low temperature, the photocurrent fluctuation from ambient background radiation exceeds the intrinsic noise of the device, indicating that the detector has reached background limited infrared performance (BLIP) regime. The rule-07, an empirical relationship that was originally created to be a design rule of thumb for HgCdTe systems has recently become a useful trend for device comparison [47]. The rule describes the dark current density as an exponential function of both cut-off wavelength (λ_c) and temperature (T) for optimized HgCdTe detectors and is given by the equation $J = 8367 \times \exp[-1.16\cdot(1.24q)/\lambda_c\cdot kT]$ A/cm^2. In this context, HgTe CQD photovoltaic devices show dark current density of 1.3 μA/cm^2 at 90K whereas HgCdTe would exhibit similar dark current level at 140K, indicating that further improvements are needed.

This Schottky diode study has inspired the development of next generation device that is based on p-n heterojunction diode. The device consist of ITO as a bottom contact (illumination side), ethanedithiol/HCl ligand-exchanged thick HgTe CQD layer, $HgCl_2$ treated Ag_2Te CQD inter-layer, thin Ag_2Te CQD layer, and Au top contact (electrode and back reflector), as shown in Figure 1.8 [48]. This device was reported to show detectivity

exceeding 10^{11} Jones below 100K and reached BLIP at 140K, a significant performance improvement compared to previous generation of devices. At 230K, a temperature accessible with compact thermoelectric coolers, the detectivity reached 10^9 Jones which exceeds the performance of microbolometers. The presence of $HgCl_2$ treated Ag_2Te CQD inter-layer has been discussed as a key to obtaining a strong and reproducible rectifying junction. This device has been further enhanced with an interference structure to achieve higher optical absorption and was used to demonstrate scanning thermal imaging with NEDT of 56 mK at 90K. The design of interference structure requires a top semitransparent contact, which was achieved with 5 nm Au, but simultaneously introduced a large series resistance and resulted in a photocurrent reduction at elevated temperatures. An alternate strategy is to employ plasmonic nanostructures for absorption enhancement. Three main parameters including diameter of the plasmonic discs, HgTe CQD layer thickness, and top Au layer thickness were optimized to enhance the plasmon resonance in MWIR region and to induce optical resonant cavity effect [49]. This approach has led to significant increase in the responsivity which were measured to be up to 1.46 A/W at 4.5 μm resonance wavelength. More importantly, above optical enhancement approaches were found to have minimal effect on the noise level of the device. To date, device that combine two approaches, plasmonic and interference (Figure 1.9), demonstrate the best performing device with detectivity of 10^{10} Jones at 220K and, when used for thermal imaging, the NEDT has been measured to be as low as 14 mK.

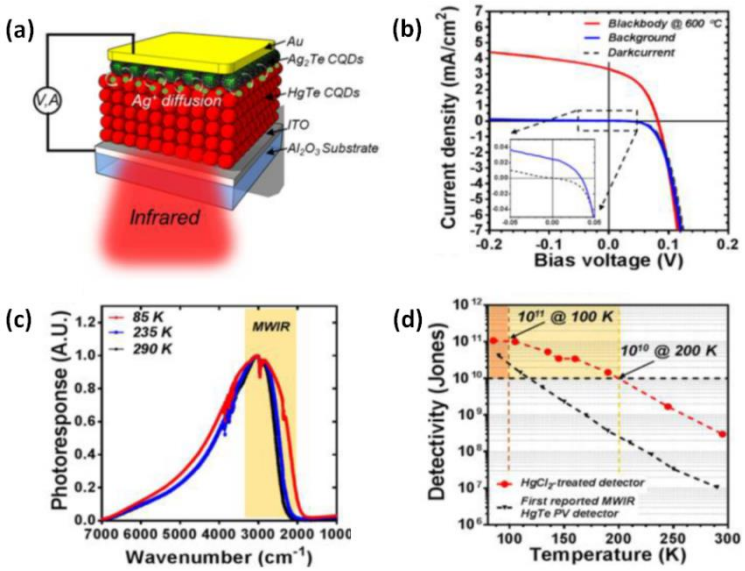

Figure 1.8 HgTe CQD-based p-n heterojunction devices. (a) A schematic of the device structure. (b) Current density-voltage characteristics obtained at 85K under dark, background radiation, and black body (600 °C) illumination. (c) The spectral photoresponse obtained at 85, 235, and 290 K. (d) The detectivity plotted as a function of temperature for the current heterojunction device (red) and the first-generation Schottky device (black).
Source: [48].

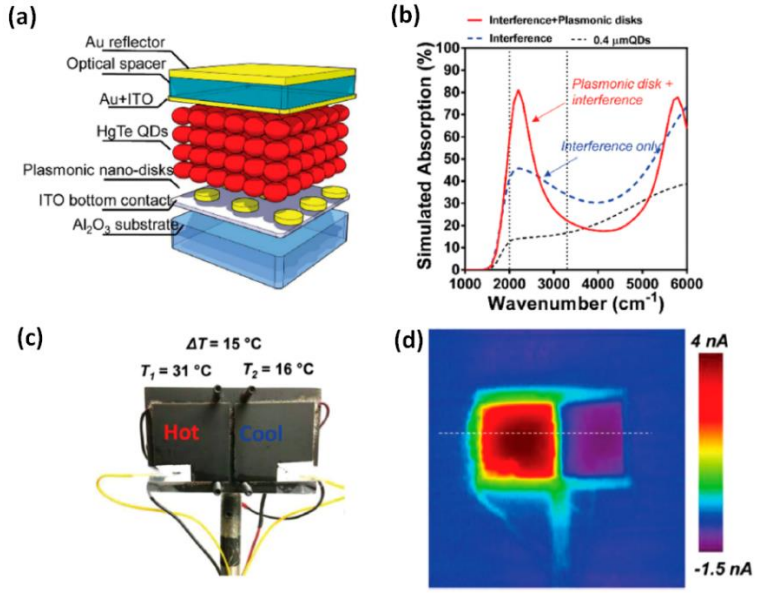

Figure 1.9 HgTe CQD-based p-n heterojunction device integrated with plasmonic disk array and interference structure. (a) A schematic of the device structure. (b) The spectral response of these devices with and without interference-enhanced plasmonic disc array. (c) Two Peltier cooler mounted on aluminum plate for scanning thermal imaging and NEDT testing. (d) The rainbow-colored imaging data obtained from (c).
Source: [49].

1.4.3 HgSe CQD-Based Devices : Photoconductive Devices

Many CQD-based optoelectronics devices studied so far rely exclusively on the interband optical transition. With the emergence of HgSe CQDs, which exhibit air-stable, n-type self-doping, intraband transition in CQDs has been harnessed for MWIR photodetection. The first demonstration of photoconductive photodetection using intraband HgSe CQD was reported by Guyot-Sionnest group (Figure 1.10a) [34]. Using CQD film (intraband absorption peak around 4.4 μm) ligand-exchanged with ethanedithiol, responsivity of 0.38 mA/W and detectivity of 2 x 10^9 Jones (500 Hz) at 80K have been measured with a perspective that the precise control of doping would lead to further performance enhancements. Similar to HgTe CQD device development, inorganic ligand exchange approach has been naturally extended to HgSe CQD MWIR devices. The HgSe CQD film ligand-exchanged with As_2S_3-based ligand has been reported to maintain n-type doping and exhibit field-effect mobility in the range of 50 -100 $cm^2V^{-1}s^{-1}$, leading to high responsivity of 0.8 A/W (Figure 1.10b) [35]. A specific detectivity of 10^8 Jones was measured at room temperature, which is comparable to the performance of commercial deuterated triglycine sulfate (DTGS) detectors, with 1/f noise being the dominant noise mechanism. Optimized doping is upmost importance in realizing high performance devices and has been discussed in various literatures [50, 51, 52] CQD films, after ligand-exchange, typically show modification in carrier concentration which is largely attributed to the bending/shifting in the energy level due to ligand-induced surface dipoles; when the $1S_e$ energy level is lower than O_2/H_2O redox potential, water act a reducing agent, making CQDs electron-rich in the ambient [50]. This theory is also consistent with the observation that intraband absorbance decreases with decreasing CQD size (stronger quantum confinement and thus, higher energy level position with respect to O_2/H_2O redox potential).

In devices, having unoptimized doping leads to large dark current. One recent approach to overcome this issue is to utilize HgSe/HgTe core/shell heterostructure CQDs [53]. Introduction of shell is typically known to result in a disappearance of intraband optical absorption [54, 55]. However, properly designed type-II band alignment in HgSe/HgTe structure give rise to intraband transition when the $1S_e$ state of HgSe core is positioned below the Fermi level of the whole CQD system. The CQD film composed of this heterostructure CQDs showed large reduction in the dark current and stronger temperature dependence in electrical conductivity with activation energy corresponding close to the intraband transition gap. The detectivity at 10 Hz was measured to be enhanced by 30 times compared to that of the device fabricated from HgSe core only CQDs (ethanedithiol ligand-exchanged). The rapid response time (below 50 μs) also confirms that the observed photoresponse are based on optoelectronic mechanism rather that bolometric thermal effects, which has been in question recently. Increasing the optical absorbance by using plasmonic structure, a same path taken in the development of HgTe CQD devices, was demonstrated using HgSe intraband CQDs as well [56]. The HgSe CQD film ligand-exchanged with As_2S_3-based ligands were integrated with Au plasmonic nanodisks to enhance intraband absorption at 4.2, 6.4, 7.2, and 9.0 μm, which resulted in 517, 288, 257, and 209 % improvements, respectively, in their responsivities.

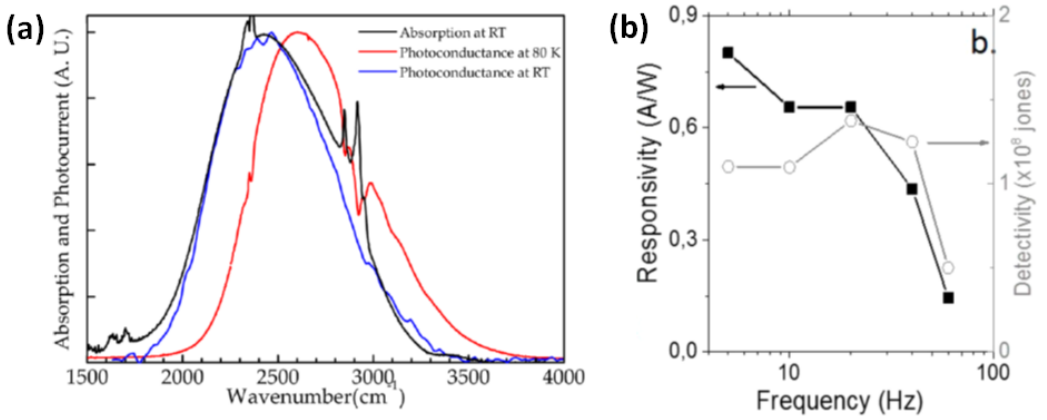

Figure 1.10 HgSe CQD-based photoconductive devices. (a) Absorption and photocurrent spectra obtained from HgSe CQD films ligand-exchanged with ethanedithiol. (b) A plot of responsivity and detectivity as a function of frequency measured from HgSe CQD films ligand-exchanged with As_2S_3-based ligands.
Source: [34, 35].

1.5 Prospect of Ag_2Se CQD for MWIR Photodetection

Although majority of research on MWIR has focused on Hg-based colloidal quantum dots, presence of mercury ion compounds in synthesis is considered as the major drawback of this technology. Mercury in any form is known to be poisonous, majorly affecting neurologic, gastrointestinal and renal organ systems, and poisoning can occur through inhalation, ingestion, and skin absorption. While CQDs are substrate bound, improper use and disposal of Hg-containing CQD devices could potentially lead to serious health and environmental concerns, especially when devices are deployed in a large scale [57]. Therefore, replacing the mercury elements with alternate non-toxic material will present significant impact in the mid-IR research and applications.

In addition, maintaining high detectivity while reducing the cooling requirement has been a collective goal in the infrared research community [58]. In traditional devices, the carrier lifetime shortens due to the onset of Auger process at high temperatures, which necessitates the use of cryogenic coolers for high performance operation [59]. This requirement for stringent cryogenic cooling has been a major impediment to their

widespread use in many emerging applications because these coolers are costly to implement, require high input power, and significantly increase the size and weight of the detector.

To address these challenges, intraband absorption in the infrared, in principle, can be achieved with many families of CQD materials under the condition that stable doping can be maintained in the ambient. One recently uncovered, non-toxic alternative to Hg-based CQDs is Ag_2Se CQDs. It has been studied that CQDs are synthesized in the tetragonal crystal structure, different from bulk, having an excess of silver, which gives rise to excess of electrons in CQDs. The stable presence of excess electrons leads to tunable intraband absorption in MWIR that can be adjusted as a function of CQD size. In these intraband QDs, it has been studied that Auger recombination can be greatly suppressed [60]. As an example of intraband HgSe CQD system, Auger process can take place through biexciton recombination producing hot hole or biexciton recombination producing hot electron (Figure 1.11). Here, the Auger transition rate is determined by the density of states, and expressed as

$$\Gamma = \frac{2\pi}{\hbar}\rho_f \; |< \mathrm{f}|\, \mathrm{V}\, |\mathrm{i} >|^2 \tag{1.5}$$

where Γ is the Auger transition rate, $\langle f|$ is an exciton final state, $|i\rangle$ is the initial biexciton or trion, V is a screened Coulomb interaction, and ρ_f is the density of resonant final states. For Auger relaxation, valence-conduction exciton determines the density of resonant final states in interband system, while $1S_e$ -$1P_e$ biexciton determines the density of resonant final

states in intraband system. In this regard, Figure 1.11a and Figure 1.11b shows large density of final states of hot electron and hot hole pathway for interband system. Figure 1.11c shows hot Auger electron but no hole pathway for intraband system defining low density of resonant final state. Therefore, Auger recombination is suppressed significantly in intraband CQD, allowing higher temperature operation of infrared photodetectors. Achieving high operation temperature constitutes an important milestone for infrared sensors and imagers as it can remove the cryogenic cooling requirement, allowing photodetectors to be manufactured with reduced size, weight, power consumption and cost (SWAP-C)

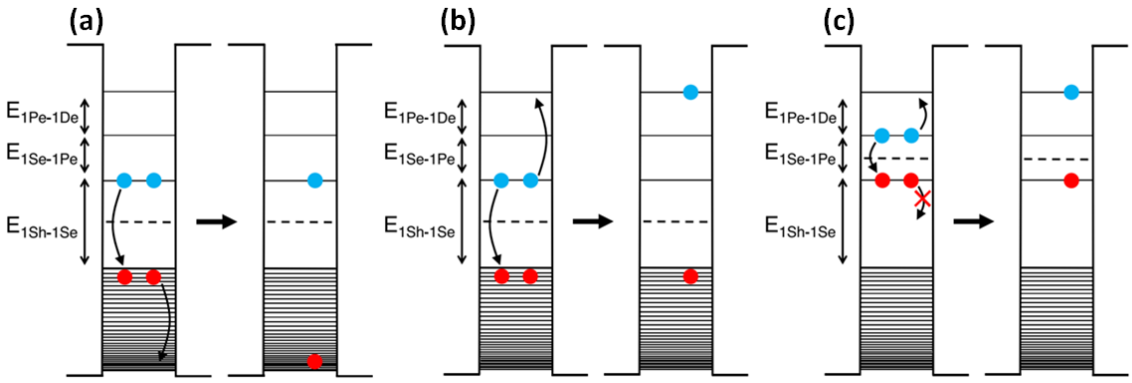

Figure 1.11 Schematics for Auger relaxation in intraband HgSe CQD, where electrons and holes are represented by blue and red, respectively (a) intrinsic particle, biexciton recombination producing hot Auger hole; (b) intrinsic particle, biexciton recombination producing hot Auger electron; (c) n-type particle, hot Auger electron with no hot hole pathway.
Source: [60].

1.6 Organization of the Dissertation

This dissertation presents research on Ag_2Se CQD for photodetection in MWIR at room temperature. In Chapter 2, synthesis of Ag_2Se CQD by hot injection method, properties of Ag_2Se CQD film and basic working principle of CQD based photodetection have been discussed. Chapter 3 demonstrates photodetection in MWIR at room temperature with

basic photoconductor device and challenges to improve carrier transport. In Chapters 4, absorption coefficient, carrier mobility and lifetime are investigated with different ligands and correlated with photodetector responsivity to provide insight on device performance. Chapter 5 outlines vertically stacked quantum dot barrier device with improved device performance, where suppression of dark current has been demonstrated due to insertion of barrier QD layer. In Chapter 6, p-n junction device is analyzed with an unique trait of binary CQD with improved device performance. Chapter 7 summarizes the dissertation and future direction of the MWIR photodetection with Ag_2Se CQD.

CHAPTER 2

INTRODUCTION TO SILVER SELENIDE CQD : SYNTHESIS, CHARACTERIZATION, AND DEVICE PHYSICS

2.1 Synthesis of Ag_2Se CQD by Hot Injection Technique

Colloidal quantum dot (CQDs) suspended in a solution are synthesized using inexpensive benchtop chemistry and solution processability of CQDs allows low-cost, large-area device fabrication [61]. This makes them a promising class of optoelectronic material for a wide array of technological applications. In this dissertation, studies are focused on chemically synthesized Ag_2Se QDs.

2.1.1 Hot Injection Technique

The formation of nanocrystal (NC) involves two steps of nucleation and growth. Synthesis of monodisperse colloidal nanocrystal with controlled size distribution is a crucial factor to observe quantum confinement, which is the prerequisite to build NC-based devices. For monodisperse nanocrystal, LaMer and Dinegar model describes that temporal separation of nucleation and growth is important (Figure 2.1) [62]. In this regard, the most common method is the hot injection technique, which provides rapid nucleation followed by a slow growth [63]. In a typical hot injection technique, one precursor solution is injected into a hot solvent and the temperature is further raised to the reaction temperature. At reaction temperature, second precursor solution is rapidly injected, which leads to supersaturation of the monomers over the critical point for nucleation within a short period of time. During the growth stage, monomers diffuse to the surface of the growing crystal and reacts with the surface. In growth stage, important feature to obtain monodisperse NCs is to reach

'size-focusing' regime. Typically, size-focusing regime is achieved in diffusion-controlled growth [64], where rate of size increase is given by

$$\frac{dr}{dt} \propto \frac{1}{r} \tag{2.1}$$

where r is particle radius. As a result, increase in particle growth leads to narrow size-distribution in diffusion-controlled growth. Hence, this technique develops separation between nucleation and growth for obtaining monodisperse NCs. In the hot injection technique, key factors controlling the size of the nanocrystal is determined by the reaction duration, injection temperature, and ratio of precursor solutions.

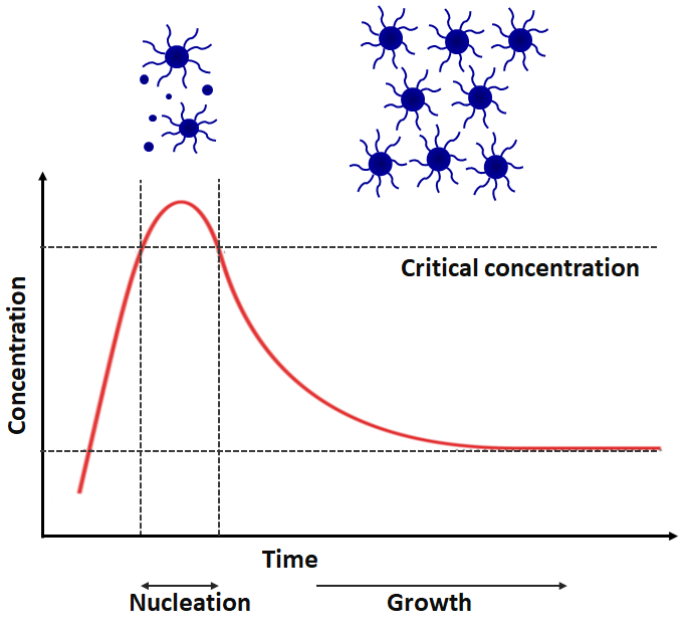

Figure 2.1 Separation of nucleation and growth during colloidal synthesis based on LaMer and Dinegar model.
Source: [62].

After the synthesis, unreacted precursors or excess ligands in the solvent act as impurities that limit charge transfer. Therefore, a purification step is an essential process to extract the nanocrystal from the reaction products to control efficient charge transport properties of the nanocrystal. Typically, this step takes place by adding polar solvent to the reaction mixture. The nanocrystals are precipitated by centrifugation and dispersed in non-polar solvent.

2.1.2 Synthesis of Ag_2Se CQD

Synthesis of high quality Ag_2Se nanoparticle has been reported recently [65], but the optical absorption was reported to be in near infrared region [66].The synthesis of monodisperse and single crystalline Ag_2Se CQD has been demonstrated by Sahu et al [67], exhibiting tunable absorption in the MWIR. In this dissertation, the Ag_2Se CQDs were synthesized by modifying this procedure based on hot injection technique, which is shown in Figure 2.2. Briefly, 15 mL of oleylamine was added to a reaction vessel and heated to 90 °C under vacuum for 1 hr. 2 mL of 1M TOP-Se that was prepared by dissolving Se power in TOP inside a nitrogen-filled glovebox was added and the temperature of the vessel was raised to 160 °C. Then, 2 mL of 0.5 M TOP-Ag, prepared though dissolving AgCl in TOP, was rapidly injected. Molar ratio of Ag : Se = 1 : 2 was used to prevent nucleation of Ag nanoparticles. The reaction was terminated after 3 sec by injecting 10 mL of butanol and quenching in a water bath to obtain CQDs with intraband absorption centered at 4.1 μm. As-synthesized CQDs were uniform in size and shape but size selective precipitation was conducted to remove the largest and smallest fractions of the CQD size distribution. The final CQDs were re-dispersed in a mixture of hexane and octane (10:1 in volume), which were colloidally stable up to a week. The synthesized Ag_2Se CQDs were

analyzed by transmission electron microscope (TEM), which indicates that CQDs are uniform in size and shape (Figure 2.2).

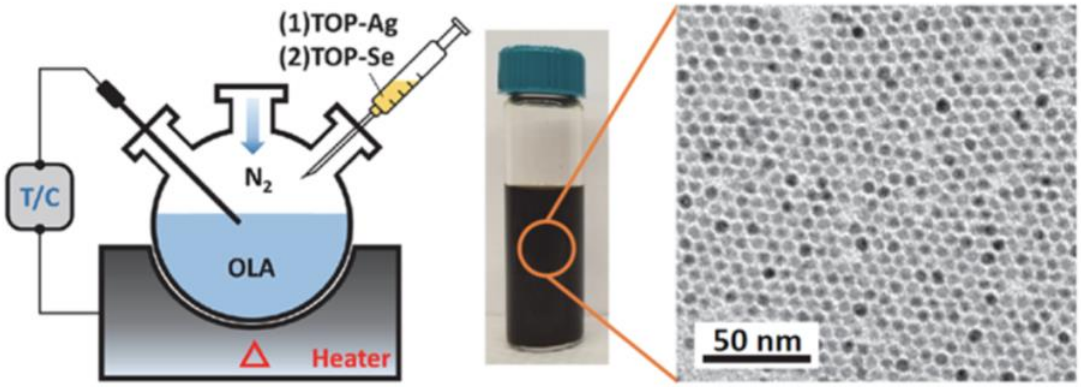

Figure 2.2 Schematic illustration of colloidal synthesis, sample Ag_2Se CQD solution, and a corresponding TEM image of CQDs. TOP-Ag, TOP-Se, OLA, and T/C denote silver chloride dissolved in trioctylphosphine, selenium dissolved in trioctylphosphine, oleylamine, and temperature controller, respectively.

Ag_2Se colloidal QDs can be synthesized to have absorption peak in the range of 4-8 μm just by controlling the CQD size. Size control of the CQDs was achieved through controlling growth temperature and time (4-5 μm absorption QDs), modifying Ag : Se precursor ratio (5-7 μm absorption QDs) and regrowth through additional precursor injection (>7 μm absorption QDs).

2.2 Characterization of Ag_2Se CQD

2.2.1 Material Characterization

In bulk, Ag_2Se are orthorhombic, narrow bandgap semiconductor with an energy gap of 0.15 eV at room temperature [68]. When synthesized as nanometer-sized crystallites below a nominal size of 40 nm, a new phase corresponding to tetragonal crystal structure is obtained [69]. Tetragonal Ag_2Se is reported to have a bulk bandgap of 0.07 eV [70, 71], which is among the narrowest of all known binary compound semiconductors.

To confirm the crystallographic structure of Ag_2Se CQD, X-ray diffraction (XRD) analysis was performed. XRD characterization in Figure 2.3a shows diffraction peaks that are different from the bulk (orthorhombic) which can be indexed to a tetragonal crystal structure [72].

As-synthesized Ag_2Se CQDs are found to have excess of electrons due to non-stoichiometric presence of silver[73]. These excess electrons fill up the first conduction energy level (hereafter denoted as $1S_e$), allowing optical transition between $1S_e$ and the second conduction energy level ($1P_e$). Energy-dispersive x-ray spectroscopy (EDSX) has been carried out for compositional analysis of Ag_2Se CQD. EDXS analysis in Figure 2.3b confirms that CQDs are composed of Ag and Se. Quantitative analysis estimate Ag:Se ratio of 3.5 – 4, a large excess of stoichiometric Ag, which is responsible for electron-rich character of CQDs [72].

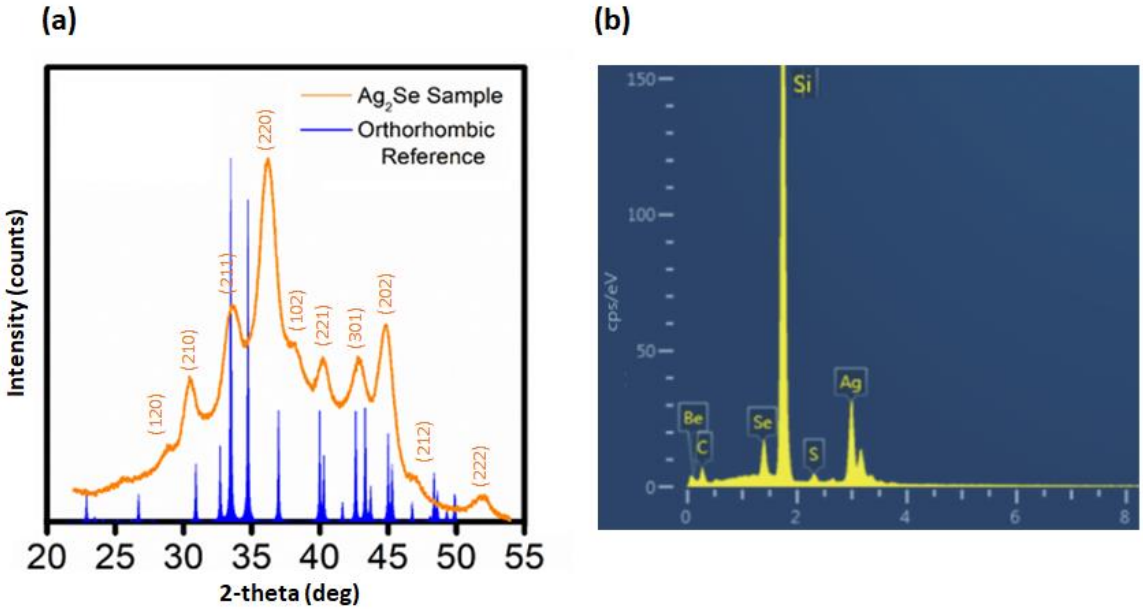

Figure 2.3 (a) X-ray diffraction (XRD) of Ag_2Se CQD exhibit tetragonal crystal structure compared to the bulk orthorhombic phase. (b) Compositional analysis of Ag_2Se CQD film by energy-dispersive x-ray spectroscopy (EDSX).

2.2.2 Thermoelectric and Electrical Characterization

To confirm electron-rich character of Ag_2Se CQD, thermoelectric and electrical measurements have been performed to examine the basic electronic property of the Ag_2Se CQD film. Thermoelectric measurement can unambiguously reveal the majority carrier type of a semiconducting film, regardless of the transport mechanism [74, 75]. Various temperature differences from $\Delta T = 0$ K to $\Delta T = 50$ K were applied across the CQD film that was deposited on glass substrate. Figure 2.4a shows the measured open-circuit voltage as a function of temperature difference, where the slope of the measured voltage vs. ΔT was calculated to obtain Seebeck coefficient of -20.44 ± 0.26 μV/K. The negative sign indicates the n-type character of the film and the small magnitude of the Seebeck coefficient hints to a fact that the film is heavily doped. This is consistent with previous reports that Ag_2Se CQD films are electron-rich [73, 76].

In addition, Field-effect transistor characterization has been widely used in the CQD electronics community to study carrier transport in films composed of CQDs [77]. Figure 2.4b shows the transfer characteristics of a bottom-gate/top-contact field-effect transistor fabricated from Ag_2Se CQD film (ligand exchanged with 1,2-ethanedithiol). The small gate response is an indicative of degenerate doping and higher drain current toward positive gate bias suggest that electrons are the majority carriers; both results are consistent with the material characterizations discussed previously. The gate current is also plotted to confirm that there were negligible leakage currents.

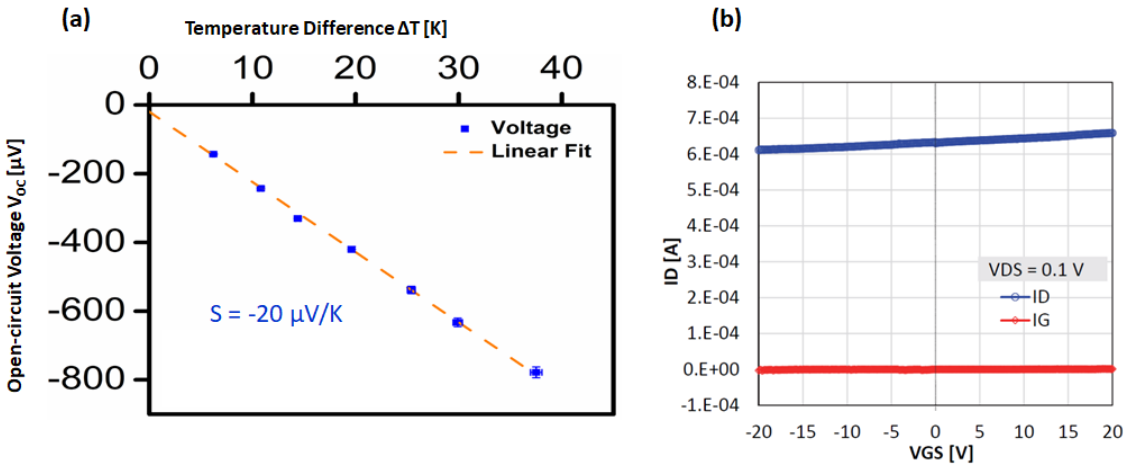

Figure 2.4 (a) Open-circuit voltage as a function of temperature difference for ligand exchanged Ag_2Se film. (b) Transfer characteristic of a field-effect transistor fabricated using Ag_2Se CQD film.

2.2.3 Optical Characterization: Intraband Transition and Tunable Optical Property

The presence of excess electrons reveals intraband transition for Ag_2Se CQDs, demonstrating its optical absorption in the mid-wavelength infrared. These excess electrons fill up the first conduction energy level (hereafter denoted as $1S_e$), allowing optical transition between $1S_e$ and the second conduction energy level ($1P_e$). Figure 2.5a shows illustration of the intraband transition. Figure 2.5b shows the Fourier transform infrared (FTIR) absorption spectra of Ag_2Se CQDs which can be tuned from 4 to 8 μm by varying the CQD size from 5.5 to 9.2 nm. Similar to traditional interband CQDs, the intraband CQDs also exhibit tunable optical properties since the size-dependent quantum confinement controls the intraband transition gap (energy gap between the first and second conduction energy levels).

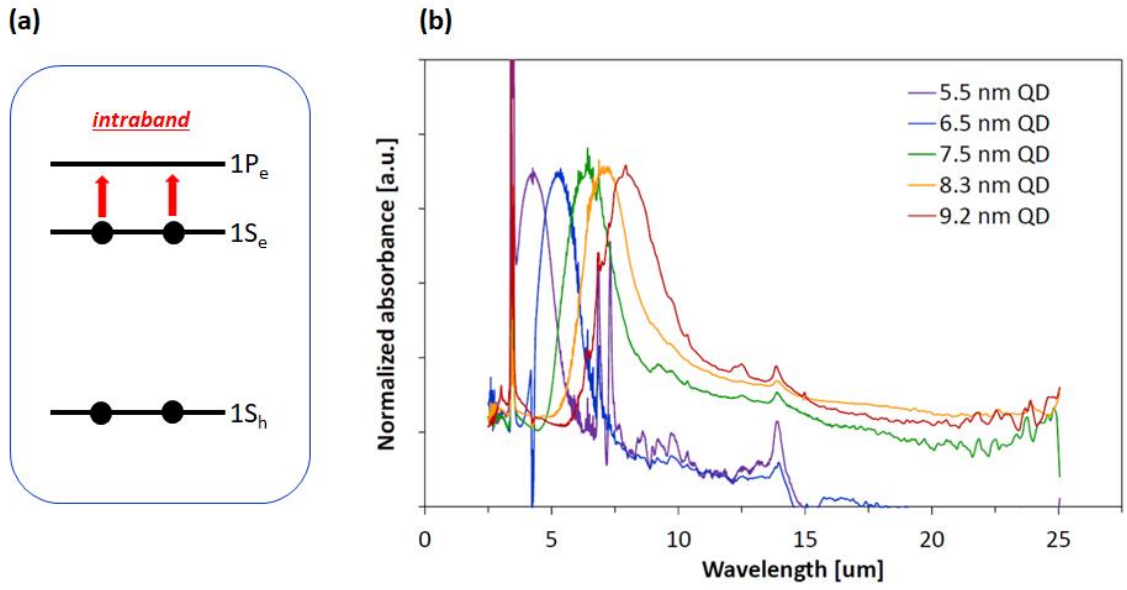

Figure 2.5 Optical characterization of Ag_2Se CQD (a) Schematic illustrating intraband transition in Ag_2Se CQD. $1S_h$, $1S_e$, and $1P_e$ denote first valence energy level, first conduction energy level, and second conduction energy level, respectively. (b) Optical absorption spectra of Ag_2Se CQDs of varying sizes, obtained through FTIR measurements.

2.3 Introduction to CQD Based Photodetection

2.3.1 Transport in CQDs and Ligand Exchange

The transport of charge carriers occurs through hopping process in CQD solid [78]. When illumination is used to generate charge carriers, they hop from one CQD to another CQD to give rise to photocurrent. At each step, the carriers must overcome a tunnel barrier, where the height of the barrier is governed by the barrier material and width is the inter-dot distance. In CQD solid, the barrier results from long ligands attached to the surface of CQD. The long surface ligands are very significant for colloidal quantum dot material, which provides stability for the colloidal solution [79]. Typically, the ligands are organic functional group, which bond to the nanocrystal surface, defining the height and width of the tunnel barrier [77]. For organic ligands, the typical value of the barrier height is around 2 eV, and length of the alkail chain determines the width of barrier as 2 nm. However, the

initial long ligand prevents quantum dots from aggregation in their solution, which are mainly isolating, hence detrimental to carrier transport. Therefore, ligand exchange procedure has been developed to reduce the ligand length to provide effective carrier transport and enhance film conductivity.

Figure 2.6 demonstrates ligand exchange procedure, which increases inter dot coupling by decreasing the ligand length. Typically, ligand exchange can be carried out either in solution phase before depositing quantum dot film, or in solid state phase after depositing quantum dot film. The solid state ligand exchange is the most common procedure, where long ligands get replaced by shorter ligands by dipping the quantum dot film in a solution of the shorter ligands. As an example, barrier width can be decreased to 0.3 nm after ligand exchange with 1,2-ethanedithiol. The process is completed by washing step to remove unreacted short ligands. The loss of long ligands creates crack in the film, which can be filled by repeating film deposition and ligand exchange to achieve specific thickness.

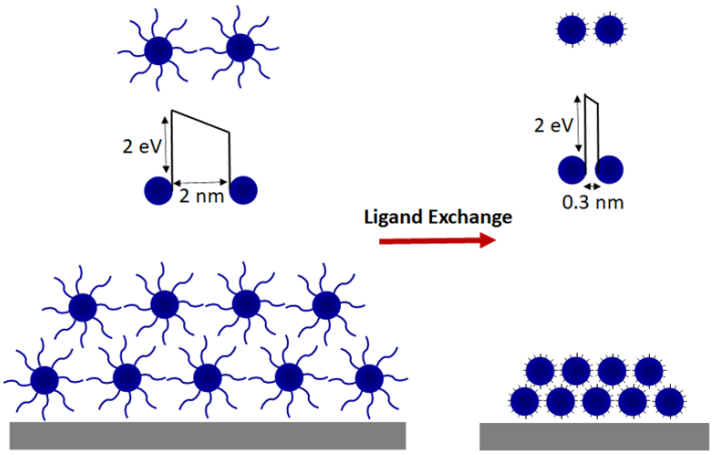

Figure 2.6 Schematic illustration of ligand exchange process. Top figure shows reduction of barrier width after ligand exchange. The bottom figure shows ligand exchange procedure increasing interdot dot coupling and conductivity in CQD film on a substrate.

2.3.2 Theory of Device Operation

CQD devices that form infrared sensors and imagers are largely classified into two groups: photoconductors and photodiodes. Both device structures share the same three fundamental steps of device operation. The first step is the optical absorption. Upon absorption of photons with appropriate energy, electron-hole pairs (EHPs) are generated inside the CQDs. For CQDs exhibiting interband optical transitions, electrons and holes are created at the first conduction ($1S_e$) and valence energy ($1S_h$) levels, respectively. For intraband CQDs, electrons and holes are created at the lowest unoccupied and highest occupied levels, respectively, inside the conduction (or valence) states. The number of photogenerated EHPs depends on the CQD film thickness, absorption cross-section of constituent CQD material and CQD packing fraction. The second step is the charge separation. The photogenerated EHPs stay in this excited state for a limited time and should be spatially separated before being annihilated through recombination (germinate recombination). In photoconductors, this is achieved through the assistance of applied bias (Figure 2.7a) and in photodiodes, built-in electric field formed at the junction plays a main role in charge separation (Figure 2.7b). The final step is the charge collection. The separated electrons and holes now need to be transported and collected at respective electrodes to give rise to the photocurrent. In photoconductors, the gap between the electrodes should be small to ensure that the time it takes for photogenerated carriers to reach the electrode (transit time) is shorter than the carrier recombination (non-germinate recombination) lifetime. In photodiodes, making the width of the quasi-neutral region shorter than the carrier diffusion length is an important criterion for efficient charge extraction. From an application perspective, CQD photoconductors are frequently reported

to have long-lived trapped charges. To maintain charge neutrality, the opposite charges circulate through the device many times giving rise to a photoconductive gain, making them suitable for high sensitivity sensor application in photon-starved environments [14, 23]. On the other hand, photodiodes exhibit faster response time and lower dark current, enough to be compatible with existing ROIC operation, enabling them to be used to form a 2D array for imaging at a high frame rate without motion blur or ghosting [43, 80].

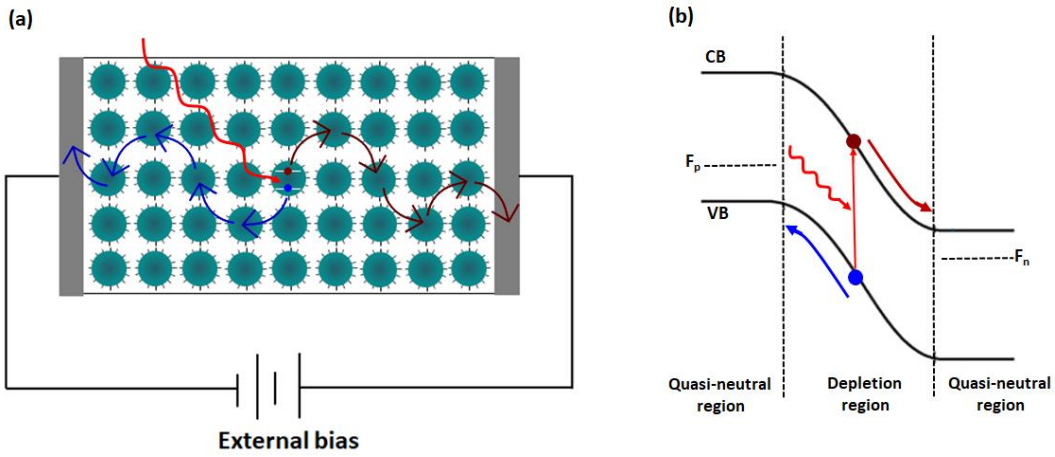

Figure 2.7 Schematic illustration of a photodetector devices (a) Photoconductor consisting of CQD film placed in between metal electrodes having Ohmic contacts. Illumination is provided to generate photocarriers, which are extracted by applying an external bias. (b) Photodiode consisting of p-type and n-type CQD films, where a depletion region is created at the junction. Generated photocarriers are immediately swept away due to built-in electric field.

2.3.3 Figures of Merit of Photodetectors

Responsivity: Responsivity is defined as the ratio of photocurrent generated to the incident optical power at a specific wavelength and is expressed by [23]

$$R(\lambda) = \frac{I_{Ph}}{P_{in}} \tag{2.2}$$

where I_{Ph} is the photocurrent in ampere and P_{in} is the optical power in watts. The responsivity depends on incident photon wavelength, applied bias voltage and modulation frequency.

External quantum efficiency (EQE): External quantum efficiency is defined as the ratio of charge carrier generation to the number of incident photon. The responsivity and external quantum efficiency are correlated as

$$EQE(\mu) = R(\lambda)\,\frac{hc}{q\lambda} = R(\lambda)\,\frac{1.24}{\lambda} \tag{2.3}$$

where *h* is the Planck's constant, *c* is the speed of light, *q* is the elementary charge and λ is the wavelength in micrometer.

Detectivity: Performance of a photodetector is characterized by the specific detectivity, given as

$$\mathrm{D}^* = \frac{RA^{1/2}}{i_n} \tag{2.4}$$

where *A* is the detector area, i_n is the noise current density, and *R* is the responsivity. Detectivity is the most important merit of figure of photodetectors, which can be used to compare photodetectors of different geometries. The unit of specific detectivity is expressed as cm $Hz^{1/2}\,W^{-1}$, also known Jones.

CHAPTER 3

PHOTOCONDUCTIVE PHOTODETECTORS BASED ON SILVER SELENIDE COLLOIDAL QUANTUM DOT FOR MID-WAVELENGTH INFRARED PHOTODETECTION

In this chapter, we demonstrate the fabrication of MWIR Ag_2Se CQD-based photoconductive photodetectors and investigate their detailed device characteristics. We investigate the effect of ligand exchange as well as temperature and spectral-dependent photoresponses. Our results suggest that further enhancement in performance could be achieved through accurate control of carrier concentration. In an alternate approach, photoconductive photodetectors with colloidal quantum dot/organic hybrid materials have been demonstrated in MWIR, utilizing a solution blend of Ag_2Se colloidal quantum dots and [6,6]-phenyl-C_{61}-butyric acid methyl ester (PCBM). With this investigation, Ag_2Se colloidal quantum dots may serve as a promising mid-wavelength infrared absorber for the development of thermal infrared sensors and imagers with low size, weight, power consumption, and cost.

3.1 Photodetection with Ag_2Se CQD Based Photoconductive Device

3.1.1 Fabrication of Ag_2Se CQD Based Photoconductive Device

The synthesized CQDs with ligand shell are dissolved in a solvent. Therefore, solution-based film preparation method, such as spin coating [81], dip coating [82], drop casting [83], can be used to prepare quantum dot film for photoconductive devices. In this work, the photodetector devices were fabricated by drop casting CQD solution onto Si/SiO_2 substrates patterned with interdigitated electrodes, which are made through conventional photolithography method. Briefly the surface of a Si/SiO_2 wafer having a thickness of 300

nm, is cleaned using O_2 plasma, followed by a rinse with isopropanol to remove impurities and residues. S1813 photoresist is spin coated and soft baked at 115 °C for 60 s. The substrate is exposed under UV though a pattern mask for 6 s. The photoresist is developed using a bath of MF319 for 50 s and the substrate is rinsed with DI water. A 5 nm Cr layer and a 45 nm gold layer has been deposited using a thermal evaporator. The lift-off process is performed by two subsequent baths in PG remover for 20 minutes at 95 ^oC. The electrodes are finally rinsed using isopropanol and dried by air flow. The channel length and total width of the electrode are 10 μm and 64.9mm, respectively.

To increase inter-dot coupling, solid state ligand exchange has been followed, where a layer-by-layer film deposition and ligand exchange (0.1 M 1,2-ethanedithiol in methanol) was carried out to achieve CQD film thickness around 60 – 80 nm. Device fabrication was completed by cleaning off the CQD films around the electrode area. Fabrication of solution based infrared CQD photoconductive photodetectors has been depicted in Figure 3.1.

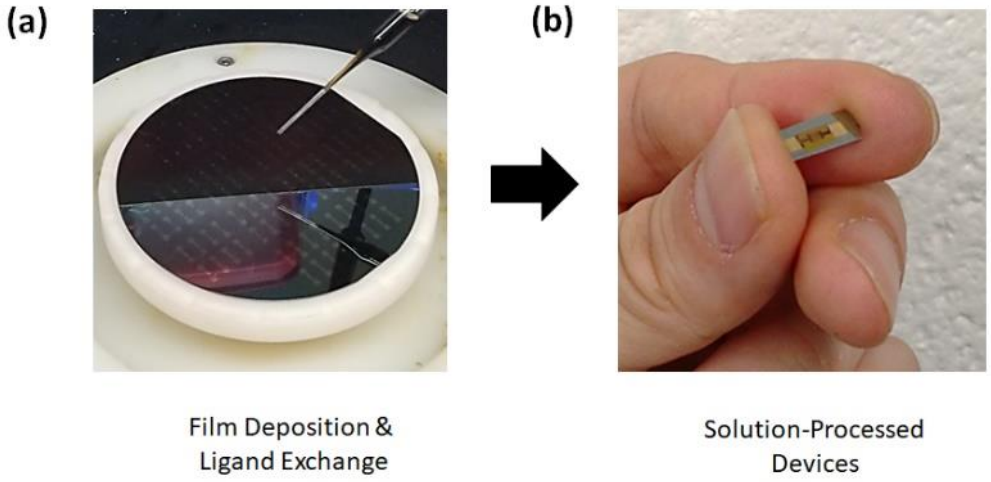

Figure 3.1 Fabrication of infrared CQD photoconductive photodetectors (a) CQD film deposition and ligand exchange steps performed at the wafer scale. (b) An example of a single completed device.

3.1.2 Optical Characterization

For the optical absorption characterization, CQD films were deposited on ZnSe disc and the absorption spectra were obtained using Thermo Nicolet 370 FTIR. Ligand-exchanged CQD films were prepared by dipping the CQD coated ZnSe disc in 0.1M 1,2- ethanedithiol (in methanol) and washing with copious amount of methanol.

3.1.3 Photoresponse Measurement Setup

The photocurrent measurement was carried out using a calibrated blackbody (900 ˚C, Newport 67030) as an illumination source. The light was modulated using an optical chopper and filtered through Ge to cutoff high energy photons. The photocurrent signal was measured using SR570 preamplifier and SR930 lock-in amplifier. The preamplifier also provided the bias to the device. The spectral responsivity was measured using the same method described for the photocurrent measurement but a set of band-pass filters with center wavelength (CT) varying from 2 to 7 μm were used in place of Ge filter. The calculated optical powers at each CT are shown in Figure 3.2 inset. The responsivity was calculated by dividing measured photocurrent with the optical power estimated for each filter. For the low temperature measurements, device was mounted inside the MMR Joule-Thomson refrigerator chamber outfitted with MgF_2 window and the temperature was controlled using MMR K2000.

The spectral irradiance of our calibrated black body (Newport 67030) was estimated using the following equation:

$$W(\lambda) = \frac{C_1}{\lambda^5 (e^{C_2/\lambda T} - 1)} \tag{3.1}$$

where C_1 and C_2 is the first and second radiation constant, respectively, λ is the wavelength, T is the temperature of the blackbody.

The optical power values used for each center wavelength has been corrected for source aperture, optical pass, optics, and detector area. The optical power incident on the device sensor area was calculated using the following equation [84]:

$$P = A.W.\frac{a^2}{4d^2}t.\eta \tag{3.2}$$

where A is the sensor area, W is the radiant emittance of the infrared light source, a is the diameter of the source aperture, d is the source aperture to device distance, t is the transmission of the optical path, and η is the amplification factor due to the concentration by parabolic mirror.

Schematics detailing the measurement setup and spectral irradiance of a black body (900 ˚C) and band pass filters have been depicted in Figure 3.2.

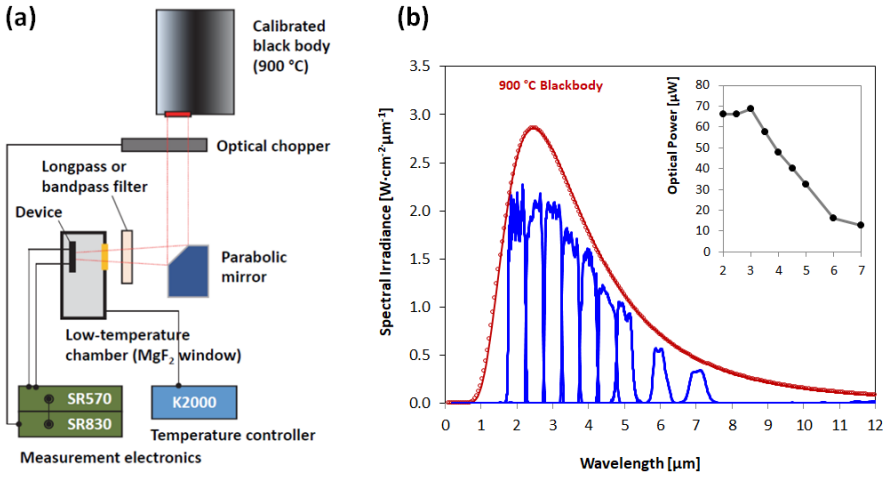

Figure 3.2 Schematics detailing the measurement setup (left) and spectral irradiance of a black body (900 ˚C) and band pass filters, with center wavelength varying from 2 to 7 µm (right). Inset shows the optical power calculated for each center wavelength.

3.1.4 Results and Discussion

We first set out to confirm optical property using Fourier transform infrared (FTIR) spectroscopy. Figure 3.3a shows the Fourier transform infrared (FTIR) spectra obtained from Ag_2Se CQD films before and after ligand-exchange with 1,2-ethanedithiol (EDT). The film composed of as-synthesized CQDs exhibit a strong intraband absorption peak centered at 4.1 μm and a rising absorbance from 2 μm to 1.7 μm detection edge which is assigned to interband absorption [73]. Other peaks around 3.5, 4.2, 6.8 μm arise from the vibrational signatures of C-H, CO_2, and trioctylphosphine (TOP), respectively. The amine capping ligands on the as-synthesized CQDs should exhibit a broad peak around 3 μm but the peak is buried under the intraband absorption in our spectrum. After the ligand exchange, intraband absorption peak weakens and becomes broader while the interband contribution strengthens. CQD films ligand-exchanged with EDT have previously demonstrated reduced electron concentration [50] and this effect is in agreement with our observations: reducing the concentration of excess electrons weakens the intraband absorption (since there are less number of electrons in the $1S_e$ state to transition to the $1P_e$ state) and enhances the interband (as there are more number of available states in the $1S_e$ state to accommodate electrons making transitions from the $1S_h$ state) absorption intensity. Figure 3.3b shows room-temperature photocurrent measurements from our photoconductive devices fabricated from EDT-ligand exchanged Ag_2Se CQD films, with and without illumination. The illumination was provided by a calibrated blackbody heated at 900 ˚C, filtered through 1.8 μm cut-off Ge long-pass filter, and chopped at 25 Hz for lock-in detection. Upon illumination, the device shows a distinct photoresponse with photocurrent corresponding to 88 nA at 0.2 V of applied bias. Increasing the bias would

increase the electric field across the electrode fingers that assist in charge separation and collection thereby increasing the magnitude of photocurrent, as shown in Figure 3.3b.

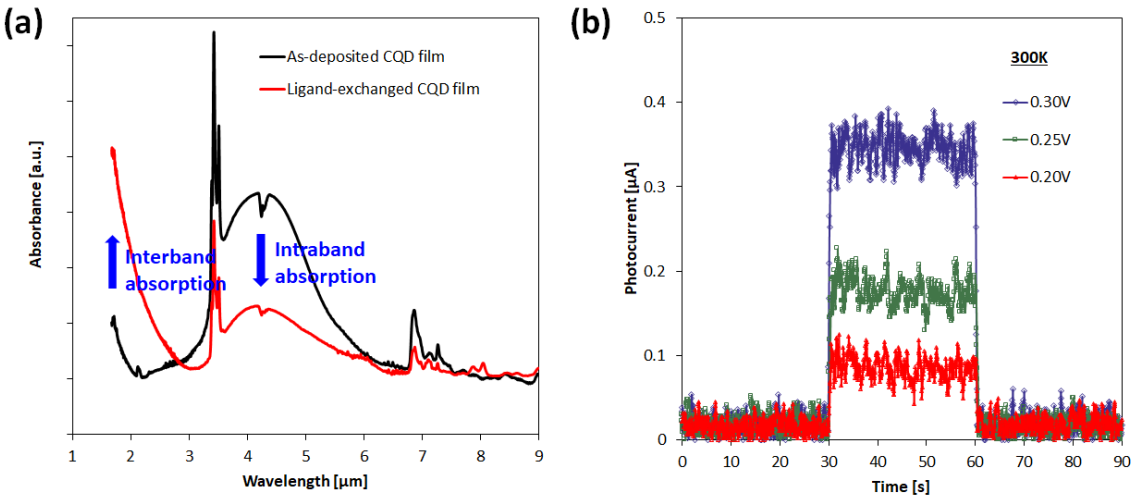

Figure 3.3 Optical absorption and basic photoconductivity characterization of Ag_2Se CQD film. (a) shows the FTIR spectra of Ag_2Se CQD film before and after EDT ligand exchange. (b) shows the room-temperature photocurrent characterization when infrared illumination was turned on and off. The illumination was provided by 900 ˚C blackbody filtered with germanium. Red, green, and blue data represent the measured photocurrent signal when 0.20, 0.25, and 0.30 V of bias, respectively, was applied.

To further investigate the spectral contribution to the photocurrent, various Fabry-Perot bandpass filters, having center wavelength (CT) varying from 2 to 7 μm, were used in place of the Ge filter. we employ a spectrally dense set of filters available to characterize the important 2 - 5 μm regions and stretched our measurement deeper into 7 μm**.** Compared to FTIR-based spectral photocurrent characterization approach [32, 34], this method enables us to obtain absolute responsivity values at each CT, as shown in Figure 3.4. We observe that the photoresponse arises dominantly from < 2.5 μm (interband) and a weak photoresponse contribution comes from 4 – 6 μm (intraband), which is consistent with the FTIR absorbance measurements discussed above. Increasing the applied bias increases the overall responsivity while maintaining the spectral shape, confirming that the photocurrents are induced optoelectronically from photons of each specified CTs. It is

worth noting that response arising from thermal bolometric effect does not show spectral discrimination and is expected to exhibit broad response across the entire infrared region which is not the case here in Figure 3.4a. Improvement in the optical absorbance hence enhancement in photoresponse in the MWIR can be achieved by increasing the doping concentration in the Ag_2Se film to have electrons filled fully up in $1S_e$ states [34]. In this optimal doping condition, there would be maximum number of electrons available in the $1S_e$ state to make transition to $1P_e$, leading to stronger MWIR absorbance. Electrically, this would also lead to the lowest dark current [85], as there are minimum number of empty state available in the $1S_e$ state for electrons can hop to, which are beneficial for achieving high detectivity.

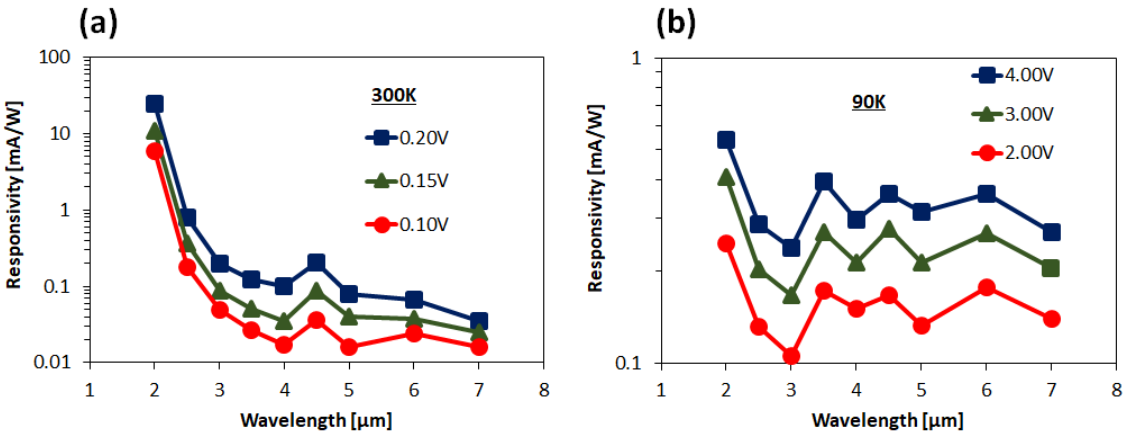

Figure 3.4 Measurement of spectral response of Ag_2Se CQD-based photoconductive photodetector. (a) and (b) show the spectral responsivity measured at various bias voltages at 300K and 90K, respectively.

To reduce the effect of thermal carriers at room temperature, we cool down the devices to further examine the device characteristics. Reducing the device temperature from 300 K to 90 K increases the electrical resistance of the CQD film by two orders of magnitude (1.2 kΩ to 100 kΩ, respectively. The spectral responsivity measured from the same device at 90 K is shown in Figure 3.4b. Two observations are noted: (1) a significantly

weakened interband photoresponse (< 2.5 μm), and (2) increased intraband contribution relative to interband. Note that since the electrical resistivity of the CQD film increases upon cooling, higher bias needs to be applied to extract the photocurrent. As such, the responsivity values obtained at 90 K and 300 K cannot be directly correlated. Thus, we compare the intraband photoresponse contribution relative to the interband in (2), by calculating the ratio between the responsivity at 4.5 μm and 2 μm from Figure 3.5b and 3.5c (the intraband / interband contribution ratio of 0.67 at 90 K is much higher than 0.01 at 300 K). These two observations can be understood in terms of carrier distribution and available optical transitions, and we propose a simplified model to explain in the following. A schematic of carrier distribution in our CQD films at 90 K is depicted in Figure 3.5a. The under-doped intraband CQD film, which is the case in our study, is represented as CQDs with one missing electron in $1S_e$. At 300 K, as illustrated in Figure 3.5b, the carrier population changes due to thermal generation of electron-hole pairs (open and closed red dots) across the $1S_e$ and $1P_e$ energy levels (we assume that thermal generation of carriers across $1S_e$-$1S_h$ states is negligible since this interband gap is much larger than kT). The allowed optical transition (blue arrow) in the intraband is now reduced while that in the interband is increased. Thus, increasing the device temperature will induce stronger interband photocurrent while reducing the intraband photocurrent, as observed in our experiments. This is a unique temperature characteristic of intraband CQD photoconductive devices. In contrast, devices that rely on interband transition in CQDs will show an opposite trend. As shown in Figure 3.5c, d (note that now CQD interband gap is responsible for MWIR absorption), increasing the temperature will weaken interband and strengthen (create) intraband photocurrent contributions.

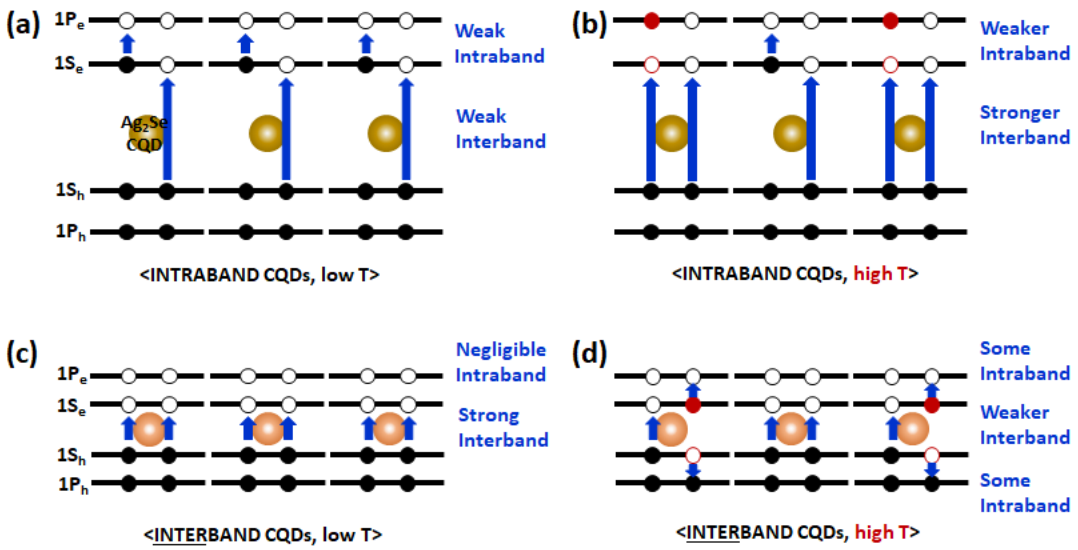

Figure 3.5 Schematics illustrating the carrier distribution and available optical transitions in intraband CQDs at (a) low and (b) high temperatures. The CQDs with a missing electron in the $1S_e$ state represent under-optimized doping condition. Open and closed red circles represent electron-hole pairs generated at elevated temperature. Blue arrows illustrate available optical transitions. As a comparison, (c) and (d) depicts carriers in typical interband CQDs at low and high temperatures, respectively. Note that interband gap is now the MWIR-absorbing gap.

To date, there is one prior study on the MWIR Ag_2Se CQD-based photoconductive devices, which reports responsivity of 8 μA/W at 25 K measured using 4.4 μm, 10 mW quantum cascade laser [76]. In comparison, our devices reach responsivity of 350 μA/W around 4.5 μm at 90 K under 4 V bias. The discrepancy arises from the differences in illumination intensity (40 μW vs. 10 mW), CQD synthesis (oleylamine-based synthesis vs. introduction of dodecanethiol during synthesis) which can lead to potentially entirely different Ag_2Se CQD systems with different carrier concentrations and surface effects, CQD film fabrication (effects of dodecanethiol on the ligand exchange), device geometry (difference in channel length and width), applied bias (4 V vs. unspecified bias), and measurement temperature (90 K vs. 25 K).

3.1.5 Conclusion

In summary, we report the fabrication and characterization of photoconductive photodetectors based on MWIR Ag_2Se CQDs. The optical absorbance and spectral photoresponse characteristics studied as a function of temperature suggest that the ligand exchange of the CQD film leads to reduced carrier concentration, yielding under-optimized responsivity. To enhance the responsivity, the device fabrication strategy should prioritize on increasing the electron concentration to prepare CQD films with the $1S_e$ level fully filled with carriers. Various methods including the use of electron-donating ligands and partial cation exchange in CQDs may lead to this improvement. With high responsivity and greatly reduced toxicity compared to Hg-based CQDs, Ag_2Se CQDs may open up many opportunities in the area of thermal infrared sensing and imaging.

3.2 Photodetection with CQD/Organic Hybrid Based Photoconductive Device

In this work, we report the fabrication and characterization of mid-wavelength infrared (MWIR = 3 – 5 μm) photodetectors based on [6,6]-phenyl-C_{61}-butyric acid methyl ester (PCBM) and Ag_2Se CQD blends. The Ag_2Se CQDs exhibit tunable optical absorption in MWIR via intraband (intersubband) optical transition [72, 86]. We chose PCBM as an electron transporting matrix material due to minimal molecular vibration signatures in the 3-5 μm region [87] and its high carrier mobility than the conjugated polymers. Also, our devices do not need the ligand exchange process which is typically required for CQD film-based devices. We note that this is of significant advantage since the strength of intraband optical absorption of Ag_2Se CQD is heavily dependent on the concentration of excess electrons present in a CQD, which is typically reduced after the ligand exchange due to de-doping effect [50, 86]. In addition, the hybrid approach presented herein may serve as a

promising strategy to minimizing the dark current in devices utilizing highly-doped intraband CQDs.

3.2.1 Device Fabrication and Characterization

PCBM solution was first prepared by dissolving 8 mg of PCBM in 0.5 mL of chlorobenzene. In a separate vial, Ag_2Se CQD solution was prepared by dissolving 12 mg of Ag_2Se CQD powder in 0.5 mL of chlorobenzene. Both were blended to create 1 mL of hybrid solution with a Ag_2Se CQD : PCBM weight ratio of 1.5 : 1. The amount of Ag_2Se CQDs was adjusted to prepare other hybrid solutions with varying weight ratios.

The films for both optical characterization and devices were deposited using spin-casting at 1000 rpm for 40 seconds, followed by annealing at 70 °C for 1 hour. For optical characterization, hybrid and pure PCBM films were deposited onto ZnSe disc. Photoconductive photodetector devices were fabricated by depositing hybrid and pure PCBM film onto Si/SiO_2 substrates with pre-patterned interdigitated electrodes (Cr/Au). The channel length and width were 10 μm and 64.9 mm, respectively. The film thickness was in the range of 50 – 100 nm.

The absorption spectra were obtained using Thermo Nicolet Avatar 370 FTIR spectrometer in transmission configuration. A calibrated blackbody (Newport 67030, 900 °C) coupled with 5 μm bandpass filter was used as an illumination source. The current was measured using Agilent 4155A semiconductor parameter analyzer.

3.2.2 Results and Discussion

We first performed optical characterizations of colloidal quantum dot/organic hybrid blend to examine the prospect for MWIR optoelectronics. Figure 3.6 shows the Fourier transform infrared (FTIR) spectra obtained from pure PCBM, Ag_2Se CQD, hybrid

PCBM/Ag_2Se CQD films. The film composed of pure PCBM (Figure 3.6a) shows characteristic peaks around 5.7, 7.0, and 8.7 μm (denoted with star symbol), which arise from the vibrational signatures of carbon to oxygen (C=O) double bonds, CH_2 bending, and oxygen to carbon (O–C) single bonds, respectively [87]. The absence of significant molecular absorptions in the MWIR makes PCBM a good candidate for near-transparent/electron-transporting medium. On the other hand, Ag_2Se CQDs (Figure 3.6b) exhibit a strong MWIR intraband absorption peak centered at 4.94 μm, which can be used as MWIR photoactive elements. The hybrid films (Figure 3.6c, Ag_2Se CQD : PCBM weight ratio = 15 : 1) shows the sum of both components where, on top of underlying PCBM molecular absorbance, MWIR absorption arising from Ag_2Se CQDs is still prominent.

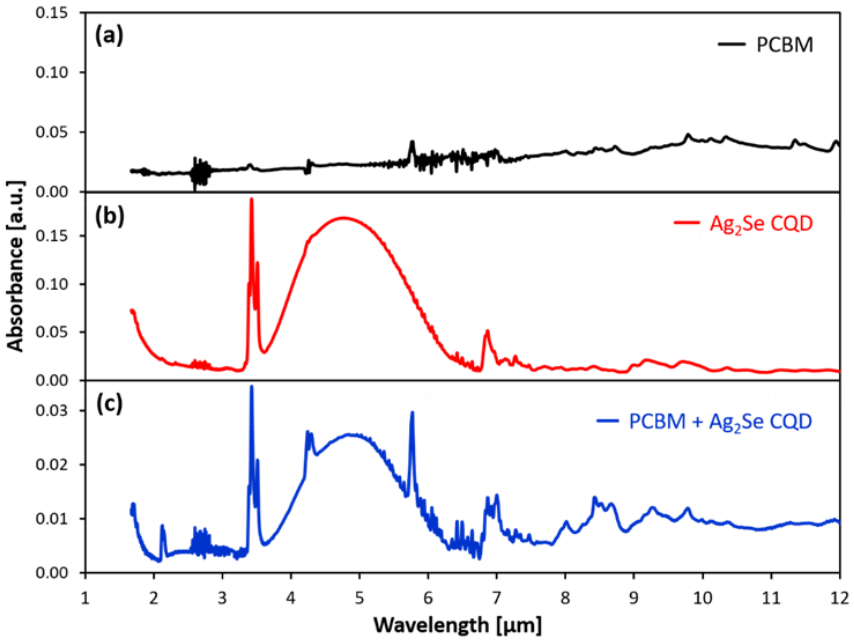

Figure 3.6 Optical absorbance characterization of (a) pure PCBM, (b) Ag_2Se CQD, and (c) hybrid PCBM/Ag_2Se CQD films. Star symbols denote characteristic peaks of PCBM which arise from the vibrational signatures of carbon to oxygen double bonds (~5.7 μm), CH_2 bending (~7.0 μm), and oxygen to carbon single bonds (~8.7 μm).

Along with the suitable optical properties, energy level alignment between the PCBM and Ag_2Se CQDs are critical in realizing functional devices. Energy levels of PCBM [88] and Ag_2Se CQD [76] has been previously measured using photoelectron spectroscopy and are plotted in Figure 3.7(a). After the formation of a hybrid film, an expanded view of conduction energy levels, which govern the transport of electrons, is shown in Figure 3.7(b). Under 5 μm MWIR irradiation, electrons occupying the first quantum-confined conduction energy level ($1S_e$) of Ag_2Se CQD is expected to photoexcite to the second quantum-confined conduction energy level ($1P_e$). Under bias, these photocarriers will be injected into the electron transporting PCBM through field emission and contribute to the photocurrent (4), as shown in Figure 3.7(c).

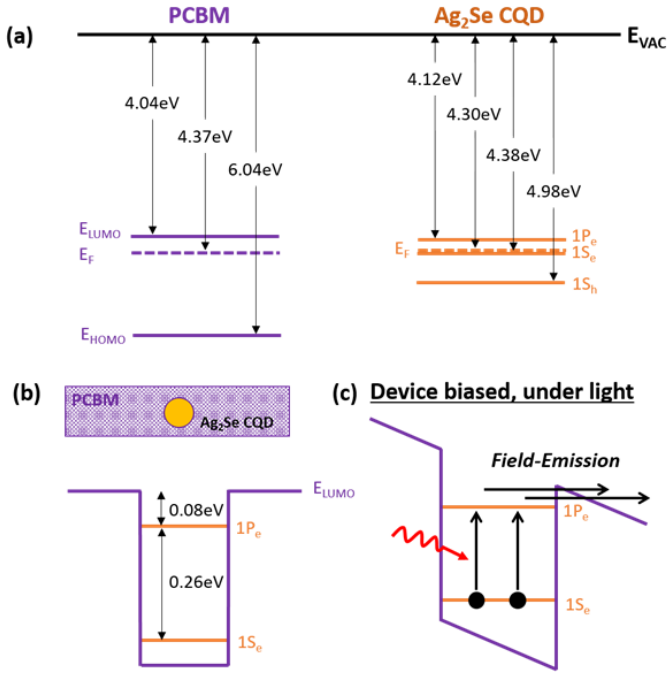

Figure 3.7 Schematic illustration of (a) energy level alignment between PCBM and Ag_2Se CQD. E_{LUMO}, E_{HOMO}, E_F, $1S_h$, $1S_e$, and $1P_e$ denote lowest unoccupied molecular orbital of PCBM, highest occupied molecular orbital of PCBM, Fermi energy level, first quantum confined valence energy level of Ag_2Se CQD, first quantum-confined conduction energy level of Ag_2Se CQD, and second quantum-confined conduction energy level of Ag_2Se CQD, respectively. (b) depicts an expanded view of conduction energy levels of hybrid blend and (c) conduction energy levels under bias and light.

Hybrid films with different Ag_2Se CQD : PCBM weight ratios, varying from 15 : 1 to 0.015 : 1, have been prepared to fabricate photoconductive photodetectors. Figure 3.8a shows a solution containing PCBM and Ag_2Se CQD blend (1.5 : 1). Transmission electron microscopy (TEM) images taken from hybrid films show a random, homogeneous distribution of Ag_2Se CQDs in PCBM with no observable phase segregation. The dark resistivity of the film has been measured as a function of Ag_2Se CQD loading, as shown in Figure 3.8c. Interestingly, we observe that the resistivity reduces with increasing CQD loading. The introduction of Ag_2Se CQDs inside PCBM would inhibit the transport of electron rather than enhancing it thus, the reduction in resistivity is expected to arise from the increase in electron concentration. While the increase in the majority carrier concentration with increasing CQD loading has been previously attributed to the interfacial charge separation of thermal carriers in TESAN-BT/CdSe CQD hybrids [89], more study is required to confirm the mechanism in our hybrid system.

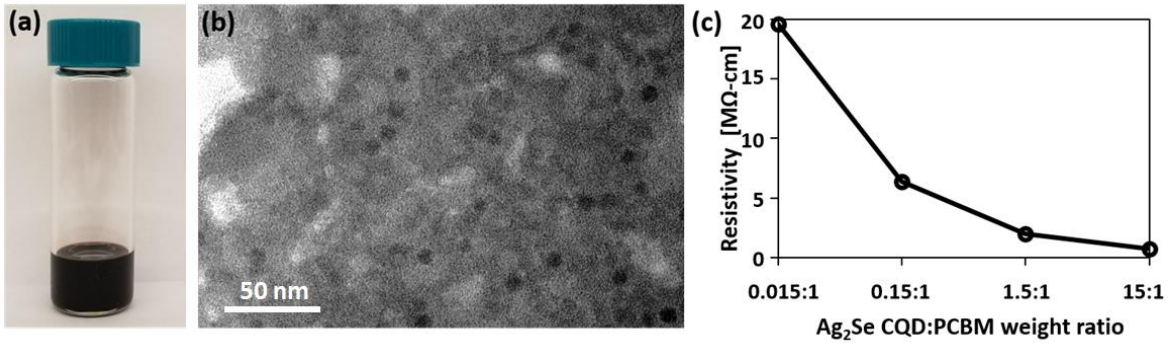

Figure 3.8 Photograph of (a) solution blend of PCBM/Ag_2Se CQD, (b) TEM image of as-deposited hybrid film, and (c) dark resistivity vs. Ag_2Se CQD loading plot.

Figure 3.9 shows the photoconductivity measurement obtained from films with increasing Ag_2Se CQD loading. While pure PCBM shows no change in the current before

and after 5 μm irradiation (Figure 3.9a), introduction of Ag_2Se CQDs in PCBM (Ag_2Se CQD : PCBM weight ratio = 0.75 : 1) induce observable changes in the current after irradiation (Figure 3.9b). Increasing the CQD loading further to 7.5 : 1 increases the magnitude of the response, as shown in Figure 3.9c. A close examination of Figure 3.9c data reveals two distinct temporal features: a sharp initial increase in the current followed by a slow saturating current. We assign the initial rapid change in the current as a response arising from optoelectronic effect (excess carrier generation through photoexcitation) and a slow saturating current as a response arising from thermal/bolometric effect (increased thermal population of carriers due to rise in temperature). Estimating the photocurrent solely from the optoelectronic contribution, the responsivity is calculated to be 0.2 mA/W (5 V bias) for 7.5 : 1 hybrid film. It is interesting to note that while pure PCBM shows no thermal/bolometric effect, the addition of Ag_2Se CQDs causes the thermal/bolometric effect to occur. The magnitude of the thermal/bolometric response also increases with increasing Ag_2Se CQD loading. Based on our measurement that 5 μm irradiation (optical power = 32.32 μW) gives approximately 1 °C increase in the device temperature, temperature coefficient of resistance (TCR) is estimated to be -1.8 $\%K^{-1}$ for 0.75 : 1 hybrid, which increases to -3.1 $\%K^{-1}$ for 7.5 : 1 hybrid films. Overall, incorporation of Ag_2Se CQD not only give rise to 5 μm optoelectronic response but also induce thermal/bolometric response. Further studies are on the way to elucidate the mechanism of CQD-induced thermal effect.

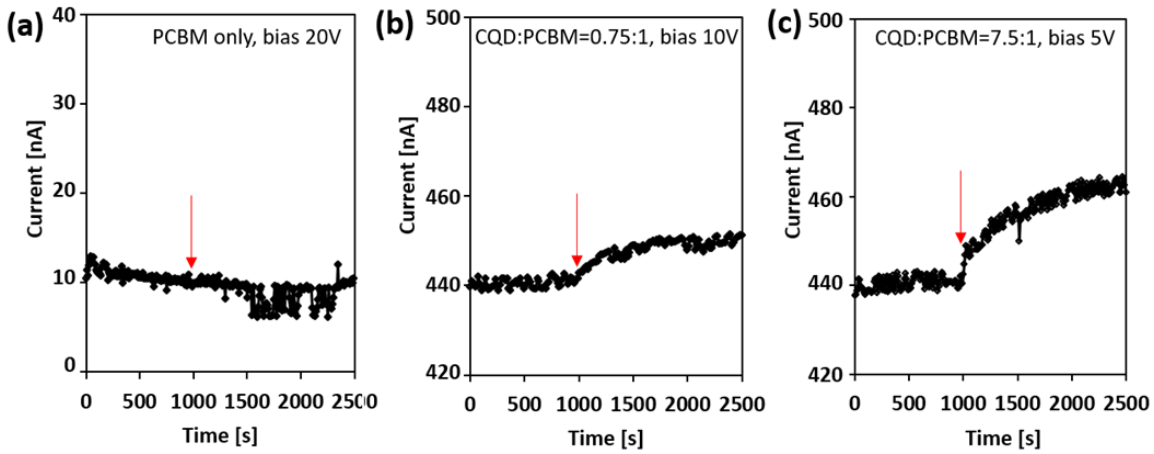

Figure 3.9 Photoconductivity measurement of (a) pure PCBM, (b) hybrid with Ag_2Se CQD : PCBM weight ratio = 0.75 : 1, and (c) hybrid with 7.5 : 1 weight ratio. Red arrows denote when the irradiation was on.

3.2.3 Conclusion

In summary, we have investigated the optical and electrical properties of PCBM/Ag_2Se CQD organic/inorganic hybrid films and fabricated photoconductive photodetectors to test the feasibility of MWIR detection. Both optoelectronic and thermal effects contribute to the 5 μm MWIR current response. The responsivity arising from optoelectronic effect was estimated to be 0.2 mA/W (room temperature, 5 V bias) while further optimizing Ag_2Se CQD concentration and film thickness could lead to higher values. The new hybrid film demonstrated in approach may open up many opportunities for low-cost optoelectronics in the MWIR where solution-processed material options are rare.

CHAPTER 4

LIGAND ENGINEERING OF MID-WAVELENGTH INFRARED SILVER SELENIDE COLLOIDAL QUANTUM DOTS

Irrespective of device types and structures (e.g. photoconductor, Schottky diode, or p-n junction diode), photodetection is governed by two fundamental steps of device operation: (1) optical absorption and (2) carrier separation and extraction [57]. The absorption coefficient of CQD film determines the magnitude of process (1) and the carrier mobility-lifetime product dictates the efficiency of process (2). It is well known that ligand exchange, a process where original long and bulky capping ligands are exchanged with a shorter one to create electrically conductive CQD films [10, 90], heavily influences these three key material parameters [50, 91] (absorption coefficient, carrier mobility, and carrier lifetime). However, there are no systematic ligand studies on the Ag_2Se CQD system reported to date. In this chapter, we characterize these parameters on films chemically treated with ligands selected from literatures that report the high-performance solar cells, photodetectors, transistors, and thermoelectrics. Based on these results, we fabricate photoconductive photodetectors from top candidate ligand-exchanged films and correlate the magnitude of mid-infrared responsivities to gain an insight into the material property-device performance relationship.

4.1 Device Fabrication and Characterization

Ag_2Se CQD films were fabricated on ZnSe (for optical measurements) discs or on Si/SiO_2 substrates (for device measurements). Drop casting was used to deposit a film and subsequent ligand exchange was performed. For As_2S_3, 0.8 M ligand exchange solution was prepared by dissolving As_2S_3 powder in polypropylamine. The solution was then diluted in ethanol and ligand exchange has been performed by dipping CQD films in the

diluted solution and washed with pure ethanol, following the previously reported protocol [39]. For ethanedithiol (EDT), ammonium thiocyanate (NH_4SCN), tetrabutylammonium iodide (TBAI), and ethylenediamine (EDA) ligand exchange, solution containing 0.1 M EDT, 0.15 M NH_4SCN, 0.02 M TBAI, and 0.1 M EDA, all in methanol, were prepared for dipping and the sample film was washed with pure methanol after the exchange process. A layer-by-layer film deposition and ligand exchange was repeatedly performed to create a thick CQD film.

For optical characterization, the absorption spectra were obtained using a Thermo Nicolet 370 FTIR spectrometer in transmission configuration. The CQD film thickness was measured using atomic force microscopy (Bruker Dimension Icon AFM). The carrier concentration and mobility of the ligand exchanged CQD films were measured by Hall effect measurement system, using a 0.5 T fixed magnet in a 4-probe chamber (H-5000, MMR Technologies). A standard van der paw configuration was used. Agilent 4155 semiconductor parameter analyzer was used to measure the current as a function of time.

Photoconductive photodetector devices were fabricated by depositing CQD film formed via layer-by-layer CQD deposition and ligand exchange, onto Si/SiO_2 substrates with pre-patterned interdigitated electrodes (Cr/Au). The channel length and width were 10 μm and 64.9 mm, respectively. A calibrated blackbody (Newport 67030, 900 °C) coupled with 5 μm bandpass filter was used as an illumination source. The photocurrent was measured using SR570 preamplifier and SR930 lock in amplifier. A Joule-Thomson cooling chamber (MMR Technologies) was used to cool the device down to 90K.

We start with a brief discussion on our characterization approaches. First, we characterize the optical absorption coefficient of ligand-exchanged Ag_2Se CQD film following the previously reported procedure on HgTe CQD film [92]. The absorption coefficient (α) is calculated from the percent transmission ($\%T$) of the film measured using Fourier transform infrared spectroscopy (FTIR) and film thickness (t) estimated using atomic force microscopy (AFM) as:

$$\alpha = \frac{2.303 * log_{10}(\frac{100}{\%T})}{t} \tag{4.1}$$

where, the $\%T$ obtained from each CQD film is shown in Figure 4.1 and Table 4.1 summarizes the results of α.

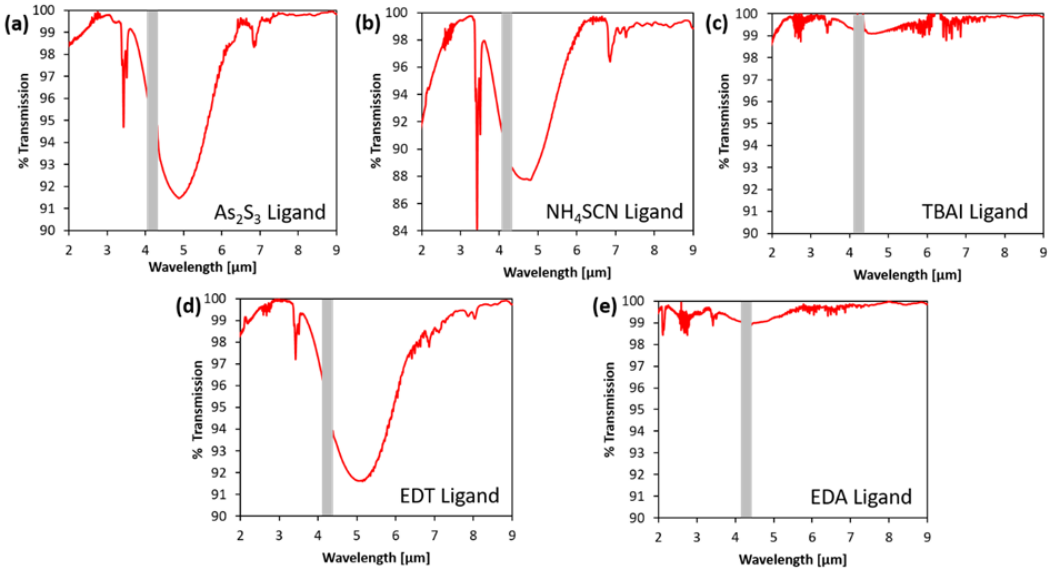

Figure 4.1 Percent transmission obtained using FTIR measurement on Ag_2Se CQD films treated with (a) As_2S_3-based metal-chalcogenide complex, (b) NH_4SCN thiocyanate, (c) atomic halide TBAI, (d) standard organic EDT, and (e) organic EDA ligands. Peaks around 4.25 μm (2350 cm^{-1}) that arise from background CO_2 are omitted for clarity.

Table 4.1 Summary of Absorption Coefficient Measurement Results of Ag_2Se QD Film Treated with 5 Candidate Ligands

Ligand Types	% of Transmission at 5 μm peak [%]	Film thickness [cm]	Absorption Coefficient [cm^{-1}]
Metal-Chalcogenide Complex (As_2S_3)	91.5	$(460 \pm 30) \times 10^{-7}$	$(1.9 \pm 0.1) \times 10^{3}$
Thiocyanate Ligand (NH_4SCN)	84.1	$(180 \pm 20) \times 10^{-7}$	$(4.5 \pm 0.3) \times 10^{3}$
Halide Ligand (TBAI)	99.1	$(420 \pm 10) \times 10^{-7}$	230 ± 10
1,2-Ethanedithiol (EDT)	91.6	$(88 \pm 5) \times 10^{-7}$	$(9.5 \pm 0.5) \times 10^{3}$
Ethylenediamine (EDA)	99	$(230 \pm 20) \times 10^{-7}$	440 ± 40

Field-effect transistor (FET) characteristic measurement has been used a common way to characterize the carrier mobility of a CQD film [77, 93]. However, due to the heavily-doped nature of the Ag_2Se CQD film, FETs show negligible gate response, making mobility value extraction challenging, as we have reported in our previous study [72]. We estimate the carrier mobility (and concentration) of our CQD film using Hall effect measurements. Performing Hall effect measurement on systems exhibiting hopping conduction is known to yield anomalous Hall signs [94][95]. Especially for film having low carrier mobility ($<<$ 1 $cm^2V^{-1}s^{-1}$), reliable measurement becomes difficult since induced Hall voltage typically becomes much lower than the large offset background voltage [96]. Such was observed in our EDT treated CQD film yielding random positive and negative Hall signs. On the other hand, strongly coupled CQD film that shows band-like conduction have been reported with reliable mobility values, in close agreement with

mobility values extract from FET analysis [97, 98, 99]. Indeed, in our Ag_2Se CQD films treated with As_2S_3 and NH_4SCN, high and reliable mobility values were measured with consistent negative Hall signs (majority carrier electrons). Table 4.2 summarizes the Hall effect measurement results obtained from each ligand-exchanged CQD film. * Denotes anomalous Hall mobility value arising from possible QD fusion. † Denotes Hall effect measurement that did not yield reliable results due to the low carrier mobility as Hall voltage becomes extremely low. This typically occurs when carrier mobility in the film is well below 1 $cm^2V^{-1}s^{-1}$ whereby extracting Hall voltage from large offset background becomes difficult [77]. The majority carrier type of electron for EDT ligand-exchanged film has been determined using Seebeck measurement in our previous Chapter 3 [72]. Anomalously high mobilities observed in TBAI and EDA sample films are possibly due to CQD fusion, which are discussed later in detail.

Table 4.2 Summary of the Hall Effect Measurement Results of Ag_2Se QD Film Treated with 5 Candidate Ligands

Ligand Types	Sheet Resistance [Ω/sq]	Carrier Density [cm^{-3}]	Mobility [$cm^2V^{-1}s^{-1}$]	Majority Carrier
Metal-Chalcogenide Complex (As_2S_3)	1.08×10^6	1.68×10^{16}	11.3	Electrons
Thiocyanate Ligand (NH_4SCN)	1.11×10^4	8.85×10^{17}	19.4	Electrons
Halide Ligand (TBAI)	1.52×10^2	3.75×10^{18}	439*	Electrons
1,2-Ethanedithiol (EDT)	3.87×10^5	Not measurable†	<< 1†	Electrons
Ethylenediamine (EDA)	1.26×10^3	1.93×10^{17}	1030*	Electrons

As for the carrier lifetime measurements, the lifetime of photogenerated carriers in CQDs are typically obtained from time-resolved photoluminescence (PL) measurements. However, this becomes challenging for CQDs having very narrow energy gap with intrinsically low luminescence efficiencies, especially for CQD films that are ligand-exchanged [100]. Also, this PL lifetime does not represent the carrier behavior in CQD film under biased operation (when carriers are under transport). Carrier lifetimes extracted from transient photocurrent measurement yield more relevant information about the CQD films used in devices and hence was the method performed in this study. All ligand-exchanged Ag_2Se CQD films were characterized by a long decay transient, i.e. photocurrent decay occurring < 100 ms constitute less than 6% of overall photocurrent decay whereas, majority of 94% photocurrent decay occurs at a timescale of tens of seconds (Figure 4.2). Thus, we extract the carrier lifetime using long time traces. Sample CQD films were cooled to 90 K and a calibrated blackbody with Ge filter, which cuts off photons with wavelength shorter than 2 μm (thus, only using mid-wavelength and long-wavelength IR photons), was used as a photoexcitation source. Photocurrent transient decay and data fitting to calculate carrier lifetime are shown in Figure 4.2. For TBAI- and EDA-treated CQD films, due to the significant reduction in MWIR absorbance after ligand exchange, photocurrent transients could not be obtained.

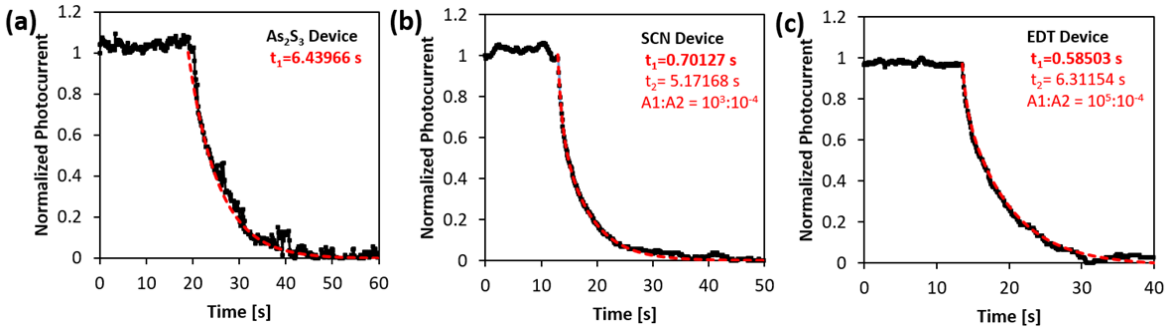

Figure 4.2 Transient photocurrent decay data obtained from photoconductive devices fabricated from (a) As_2S_3, (b) NH_4SCN, and (c) EDT treated CQD film at 90K. The data in (a) can be fitted to a single exponential function with characteristic lifetime of t_1 while (b) and (c) are fitted to a biexponential equation having t_1 and t_2 lifetimes with pre-exponential factors of A1 and A2, respectively.

4.2 Property Characterization of Ag_2Se CQD Films Ligand-Exchanged with Various Ligands

Based on these characterization approaches, the following describes the analysis results on Ag_2Se CQD films treated with 5 selected ligands, along with a rationale behind the choice of each ligand.

4.2.1 Metal-Chalcogenide Complexes Based on As_2S_3

Our first ligand choice is the molecular metal chalcogenide complex $(NH_4)_3AsS_3$ which replaces the parent oleylamine ligand attached on the CQD surface to inorganic As_2S_3 capping shell. The metal chalcogenide ligands have been widely reported to yield high field-effect mobilities due to the reduction in transport energy barriers compared to the standard organic ligands [101]. Notably, mobility values exceeding 400 $cm^2V^{-1}s^{-1}$ have been demonstrated for CdSe CQD films with composition-matched Cd_2Se_3-based capping ligands [102]. As_2S_3-based capping ligand used in this study, in particular, is transparent in the mid-infrared [35] whereas typical organic ligands have characteristic mid-infrared absorption signatures, which adds to a significant motivation for our study. Indeed, in our Ag_2Se QD films, high electron mobility of $\approx$ 10 $cm^2V^{-1}s^{-1}$ is observed. In fact, this is

consistent with the previous report on HgSe QDs where ligand exchange to As_2S_3 yields electron mobility of 90 $cm^2V^{-1}s^{-1}$ with highest detectivity of 10^8 Jones reported to date for intraband CQD-based devices [35]. The optical absorption coefficient ($\approx 10^3$ cm^{-1}) is also comparable to HgTe QDs (3×10^3 cm^{-1}) [92] which is currently the leading mid-infrared CQD (interband) material.

The photocurrent decay obtained from Ag_2Se CQD films treated with As_2S_3 complex ligands can be fitted to a single exponent with a carrier lifetime of $\tau_1 = 6.4$ s (Figure 4.2a), the longest lifetime of all films investigated. Such long characteristic time constants, up to tens of seconds, have been widely observed in CQD-derived films [80, 103] and has been assigned to originate from deep trap states. Combined with the mobility value, As_2S_3 ligand exchanged films show the highest carrier mobility-lifetime product of 72.3 cm^2/V.

4.2.2 Thiocyanate Ligand: NH_4SCN

Our second ligand is the thiocyanate (NH_4SCN) ligand, which has also been studied to exhibit high field-effect mobility of 27 $cm^2V^{-1}s^{-1}$ [99], a high value reminiscent of a band-like transport. Applying this ligand to our Ag_2Se CQD films results in both high electron mobility (19.4 $cm^2V^{-1}s^{-1}$) and high absorption coefficient ($\approx 10^3$ cm^{-3}), making it one of the top candidates to pursue further as photodetector devices.

A bi-exponential equation with characteristic carrier lifetime of $\tau_1 = 0.7$ s and $\tau_2 = 5.2$ s gives an accurate fitting to the photocurrent decay (Figure 4.2b), indicating an energetic distribution of trap states [103]. However, the pre-exponential factor (weight) of long τ_2 lifetime component is negligibly small (10^{-7} times smaller than τ_1 component) than τ_1. Based on predominant τ_1 lifetime value, CQD films treated with NH_4SCN show the

highest mobility among the list of ligands (excluding anomalous values) resulting in a carrier lifetime product of 13.6 cm^2/V.

4.2.3 Atomic Halide Ligand: TBAI

Atomic halide ligands (tetrabutylammonium iodide, TBAI), which is the third choice of our study, have been frequently employed in fabricating CQD solar cells to yield high photovoltaic efficiencies [104, 105]. The high efficiencies have been studied to arise from improved surface passivation compared to the organic ligand counterparts, owing to their small sizes (I^- ion) and hence reduced steric hindrance. Employing this ligand to Ag_2Se CQDs, however, unexpectedly led to a large reduction in MWIR absorbance (Figure 4.1c). Reductions in optical absorbance after ligand exchange have been previously observed in HgSe CQD films, originating from dedoping effect [50]. Reducing the number of electrons populating the first conduction state $1S_e$ will weaken the $1S_e$ to $1P_e$ (second conduction state) optical transition, thereby reducing the corresponding absorbance. However, this is not in agreement with the electron density measured in our TBAI ligand exchanged CQD films (Table 4.2), which shows higher electron concentration than As_2S_3 and NH_4SCN treated films. An alternative explanation is the occurrence of CQD fusion after TBAI ligand exchange. In fact, the observation of atomic ligand exchange-induced CQD fusion is not new and has been previously reported as a novel method of creating epitaxially-connected CQD superlattice films [106, 107]. A significant fusion in Ag_2Se CQD film may lead to a near-complete relaxation of quantum confinement, which will wash away the distinct absorption feature in the mid-infrared. In addition, phase change from tetragonal to orthorhombic is possible, if the fusion results in a grain size larger than 38 nm [69]. The occurrence of CQD fusion is also supported by anomalously high carrier mobility of 439

$cm^2V^{-1}s^{-1}$ that resembles the magnitude observed in bulk Ag_2Se thin-films. Polycrystalline Ag_2Se thin-films have been reported to have high electron mobility, reaching 1000 $cm^2V^{-1}s^{-1}$ even at carrier concentration in the excess of 10^{18} cm^{-3} [108, 109]. Overall, both optical and electronic property characterization results points to an occurrence of CQD fusion. More chemical, structural, and morphological studies are currently on the way to elucidate the detailed mechanism. On the other hand, due to an orders of magnitude reduction in MWIR absorption, photocurrent decay measurement was not possible. It is concluded that while these films yield very high carrier mobilities, small absorbance in the MWIR spectral region renders them ineffective for use in photodetection.

4.2.4 Standard Organic Ligand: EDT

The fourth ligand is 1,2-ethandithiol (EDT) which has been used widely in the CQD device community as a standard, compact organic ligand [82, 110]. While this ligand yields the highest absorption coefficient ($\approx$ 9 x 10^3 cm^{-1}), the carrier mobility is below our measurement limit of DC Hall effect [96]. This indicates that the mobility is significantly below << 1 $cm^2V^{-1}s^{-1}$. The closest system is the intraband HgSe CQD film which has a reported mobility of 6 x 10^{-4} $cm^2V^{-1}s^{-1}$ with identical EDT treatment [34]. The photocurrent transient decay data obtained from EDT-treated Ag_2Se CQD film shows a carrier lifetime of τ = 0.58 s (Figure 4.2c), a similar timescale to NH_4SCN treated films.

4.2.5 Organic Ligand with Different Functional Group: EDA

The final ligand is ethylenediamine (EDA). In comparison to the standard EDT ligand that demonstrates the amine-to-thiol ligand exchange, EDA enables us to investigate amine-to-amine ligand exchange. The significant reduction in absorption coefficient and anomalously high value of electron mobility (1030 $cm^2V^{-1}s^{-1}$) suggest that CQD fusion and

film microstructural changes may be taking place in EDA-treated CQD film, similar to that of TBAI ligands. Due to absence in MWIR absorption, photocurrent decay measurement was not possible. The negligible absorption in the mid-infrared makes this ligand ineffective for photodetector applications.

4.3 Measurement of Device Characteristics of Ag_2Se CQD-Based Photodetectors

Based on above property characterizations, photoconductive photodetector devices of As_2S_3, NH_4SCN, and EDT ligand-exchange CQD films were fabricated for MWIR responsivity characterization. The measurement was performed by illuminating the CQD film at 5 μm (resonating with the CQD absorption peak) and measuring the photocurrent using lock-in technique. Figure 4.3 shows the device responsivity measurement results obtained at 90 K.

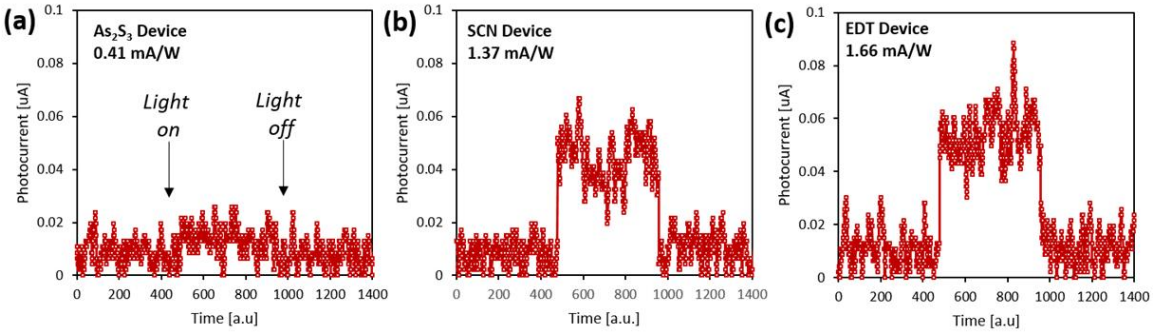

Figure 4.3 Photocurrent measurement data of (a) As_2S_3, (b) NH_4SCN, and (c) EDT treated CQD devices obtained using 5 μm MWIR illumination at 90 K.

4.3.1 Devices Based on As_2S_3 Treated CQD Film

The device made from Ag_2Se CQD films treated with As_2S_3-based ligands, which is expected to show the best device performance, exhibit the lowest responsivity of 0.41 mA/W of the three candidate devices. As the carrier mobility-lifetime product is the highest, this device is expected to have the highest carrier collection efficiency. The observed low photocurrent indicate that a different recombination mechanism is present,

other than non-germinate recombination that photocarriers experience during transport. Other recombination mechanisms frequently discussed in CQD system are the monomolecular (germinate) recombination where photogenerated exciton recombine at the single CQD level before splitting into separate electron and hole photocarriers. This can occur if the ligand exchange creates large density of defects at the CQD surface. The low absorption coefficient (α = 1.9 x 10^3 cm^{-1}) combined with high rate of monomolecular recombination due to defective surface may thus lead to the lowest amount of photocarriers initially. The reason behind why As_2S_3 specifically induces monomolecular recombination active surface defects is unclear and require further study.

In photoconductive devices, the driving force for exciton separation is provided by the external applied bias. Increasing the bias would enable charge separation to occur more effectively thereby minimizing the monomolecular recombination. However, we have found that Ag_2Se CQD devices can operate only at small bias ranges, typically < 4 V (4000 V/cm), and increasing the bias irreversibly damages the CQD film due to high diffusive nature of Ag+ ions that compose the CQDs. This seems to be the limitation of current generation Ag_2Se CQD devices. For a comparison, PbS CQD have shown to operate up to 100 V bias (2 x 10^5 V/cm, while not practical) to demonstrate high responsivity [81]. If high biasing was possible in Ag_2Se CQD, it is anticipated that a regime change from germinate to non-germinate recombination will occur and thus, As_2S_3 treated device would exhibit the top responsivity. Hybrid ligand strategy have been previously demonstrated in CQD solar cell research with great success [111]. Following the first ligand exchange, which effectively reduces the inter-CQD spacing to enhance the carrier mobility, a second ligand exchange is performed (second ligand is usually smaller than the first ligand) with

a purpose of improving the surface passivation. This strategy could be adopted, if appropriate atomic-sized ligand can be identified that can remedy the surface defects while preserving the MWIR absorbance.

Reflecting the fact that these CQD films show long characteristic carrier lifetimes, a photoconductive gain mechanism may be present that may lead to a greatly amplified responsivity [80]. In our As_2S_3 treated CQD devices, the transit time ($\tau_{tr} = L^2/\mu V_{SD}$) of 4.42 x 10^{-8} s can be estimated from the carrier mobility (μ = 11.3 $cm^2V^{-1}s^{-1}$), channel length (L = 10 μm), and source-drain bias (V_{SD} = 2 V). Taking the carrier lifetime of 6.4 s, a high gain on the order of 10^8 can be theoretically reached. However, this would not be measured through the lock-in detection technique employed here. The optical chopping frequency of 15 Hz indicate that the illumination repeats on/off cycle every 0.06 second, much before the photocurrent rises to a higher saturation value which is expected to take at least several seconds (Figure 4.2). While the photoconductive gain would lead to a greater photodetector sensitivity, the slow time response typically makes them impractical for many fast sensing or imaging applications.

4.3.2 Devices Based on NH_4SCN Treated CQD Film

The devices fabricated from CQD treated with NH_4SCN have lower carrier-lifetime product but higher absorption coefficient than As_2S_3-treated CQD devices. The measured MWIR responsivity is also higher (1.37 mA/W). If monomolecular recombination is the dominant mechanism in these devices as well, it is expected that higher absorption coefficient is primarily responsible for the observed higher responsivity.

4.3.3 Devices Based on Standard Organic EDT Treated CQD Film

With similar carrier lifetime to SCN devices, organic EDT treated CQD device exhibit the highest responsivity of 1.66 mA/W. This is surprising, reflecting the fact that the mobility is expected to be << 1 $cm^2V^{-1}s^{-1}$. This suggests that while carrier collection is not as efficient, the photocarrier separation and thus the extent of surface passivation is greater than SCN and As_2S_3 treated CQD devices. The largest absorption coefficient (9.5×10^3 cm^{-1}) combined with better surface passivation could be accounted for the high responsivity observed in this study. This again suggests that the separation of photocarriers, rather than carrier collection efficiency, is the limiting factor of our Ag_2Se CQD devices.

Table 4.3 summarizes the infrared responsivity at 5 μm. The magnitude of the device responsivity is the order of EDT > NH_4SCN > As_2S_3. Our finding is in stark contrast to commonly studied MWIR HgTe and HgSe CQD devices, where top device performance is obtained from As_2S_3 treated devices due to high carrier mobility-lifetime product (maximum carrier collection efficiency) [35, 100]. The correlation between the material property characterizations and device performance results suggests that having maximum optical absorption and minimum monomolecular recombination (thus, maximum generation of photocarriers) is an important factor that determines the ultimate responsivity of our current generation of Ag_2Se CQD device.

Table 4.3 Summary of Absorption Coefficients, Mobility-Lifetime Products, and Infrared Responsivities of Ligand Exchanged Ag_2Se CQD Films

Ligand Types	Absorption Coefficient [cm^{-1}]	Mobility-Lifetime Product [cm^2/V]	Responsivity at 5 μm [mA/W]
Metal-Chalcogenide Complex (As_2S_3)	$(1.9 \pm 0.1) \times 10^3$	72.3	0.41
Thiocyanate Ligand (NH_4SCN)	$(4.5 \pm 0.3) \times 10^3$	13.6	1.37
1,2-Ethanedithiol (EDT)	$(9.5 \pm 0.5) \times 10^3$	N/A	1.66

4.4 Conclusion

In summary, we have investigated five candidate ligands for intraband Ag_2Se CQDs film and characterized three key properties that determine the performance of photodetector devices. These results were correlated with MWIR responsivities obtained for device fabricated from respective ligand-exchanged CQD films. Based on the analysis between the material property and device performance, we discuss that having maximum optical absorption and minimum monomolecular recombination (thus, maximum generation of photocarriers) is an important factor that determines the ultimate responsivity of our current generation of devices. Due to limited bias operation range of Ag_2Se CQD-based devices, the future effort should focus on improving the surface passivation. Hybrid ligand approach may point the way to this improvement.

CHAPTER 5

VERTICALLY STCAKED QUANTUM DOT BARRIER DEVICES WITH IMPROVED DETECTOR PARAMETERS

In this chapter, we present the first vertical intraband QD heterojunction barrier devices composed of Ag_2Se/PbS/Ag_2Se QD stacks. To date, MWIR intraband QD photodetectors have only been studied as lateral photoconductive devices [35, 112], while advancing the device toward a vertically stacked structure can have great implications in their applications. Specifically, vertically stacked QD devices can enable direct integration of intraband QD technology with existing silicon read-out integrated circuits for fabricating focal plane arrays without hybridization [22, 25]. From a scientific point of view, the vertical structure enables the incorporation of complex heterostructure QD layer stacks that can be used to modulate carrier distribution and dynamics for improved detector performance.

In this chapter, Section 5.1 describes the advantage of using a barrier layer in QD based devices. Section 5.2 presents colloidal synthesis of Ag_2Se QDs with improved synthetic yield and discuss the device fabrication in which ligand exchange duration is found to be a critical parameter in creating MWIR-responsive QD films. In Section 5.3, we carry out device characterization to understand carrier transport in QD stacks containing a barrier layer, measure the key detector performance parameters, and compare our results with other MWIR QD research reports. In the last Section 5.4, we demonstrate optimization of energy level alignment to improve detector performance parameters.

5.1 Advantage of Using a Barrier Layer in QD Based Devices

Our vertical device design that incorporates PbS QDs as a barrier layer was inspired by the nBn (n-type/barrier/n-type) infrared photodetector design [113] that has been adapted for InSb [114], HgCdTe [115], and InAs/GaSb superlattices [116]. The primary advantage of using a barrier layer in intraband QD-based devices is two-fold. First, the thin films composed of Ag_2Se QDs have been studied to have high electron concentration [86, 117], giving rise to an extremely high dark conductivity that is detrimental to high sensitivity photo detection. By introducing a potential barrier, dark conductivity can be significantly reduced. An ideal barrier structure that minimizes dark conductivity would be the one that is composed of both electron and hole barriers (resembling the p-i-n structure [118]) to block the transport of thermally generated electrons and holes, respectively, while providing an unimpeded flow of photocarriers. Here, we demonstrate the concept of hole barrier as it is immediately available using PbS QDs-a standard semiconductor QD that has been widely used in various QD optoelectronic applications [23, 119, 120]. Second, implementing nBn barrier device structure greatly simplifies the device fabrication procedure. The fabrication is identical to creating a simple vertically stacked photoconductor via layer-by-layer QD deposition but with an inclusion of an additional QD layer that serves as a potential barrier.

5.2 Synthesis, Device Fabrication and Ligand Exchange Duration

5.2.1 Improvement in QD Synthesis Yield

Compared to the lateral photoconductor devices, which require 2-3 QD film depositions, fabricating a vertically stacked device requires a large quantity of QDs to complete 20-30 layers of QD depositions. Thus, improving the existing QD synthesis yield was the first

step toward achieving vertical devices since previously reported procedures [86, 87] suffer from very low synthetic yields (typically less than 3 mg for 25 mL volume reaction for QDs with sizes smaller than 5.5 nm or MWIR absorption peak less than 4.2 μm). It has been previously studied that pure tertiary phosphine chalcogenides, which are commonly used as precursors for metal chalcogenide QD synthesis, are rather unreactive with the metal precursors [121, 122]. A small addition of secondary phosphines, such as diphenylphosphine (DPP), is known to dramatically increase the synthetic yield. This has been discussed to be universal to all phosphine-based syntheses [121]. Following this protocol, we have added a small amount of DPP (TOP/DPP = 30:1 in volume) to our synthesis and observed 10-fold increase in our 5.5 nm Ag_2Se QD synthesis yield (50 mg for 55 mL volume reaction) without sacrificing the QD size uniformity. Figure 5.1a shows a transmission electron microscopy (TEM) image of the as-synthesized Ag_2Se QDs with an average size of 5.5 nm and size dispersion of approximately 35%. PbS QDs, which will be used as a barrier layer, were synthesized following the previously reported protocol [123], and the TEM image (average size = 5 nm, size dispersion = 20%) of the sample is shown in Figure 5.1b. Figure 5.1c shows the Fourier transform infrared (FTIR) spectrum of Ag_2Se QDs, which shows a distinct intraband absorption peak at 4.2 μm. Other characteristic peaks around 3.4, 4.4, and 6.8 μm correspond to vibrational modes of C-H, CO_2, and trioctylphosphine (TOP), respectively. PbS QDs show interband absorption peak centered at 1200 nm, as shown in Figure 5.1d.

5.2.2 Device Fabrication

To fabricate the device, we started with a sapphire substrate prepatterned with a Ag electrode that serves as a bottom Ohmic contact. The Ag_2Se QD layers were then deposited

by repeating layer-by-layer QD deposition and 1,2-ethanedithiol (EDT) ligand exchange procedure [82, 90] to create an electronically coupled QD film. After 10 rounds of Ag_2Se QD layer deposition, a PbS QD barrier layer (4-5 depositions) was deposited following the identical procedure used for Ag_2Se QDs. The QD device layer was completed by adding another 10 layers of Ag_2Se QDs. Optimization of the QD spin-coating process was critical in achieving a crack-free QD film. For the top contact, 120 nm of Ag with two finger electrodes was deposited using a shadow mask. In conjunction with the bottom electrode, this defines the device optical area of 200 × 200 μm, as shown in Figure 5.2a. The device cross-section, examined using a scanning electron microscope is shown in Figure 5.2c. The total QD layer thickness was approximately 300 nm (120 nm Ag_2Se, 60 nm PbS, and 120 nm Ag_2Se QDs).

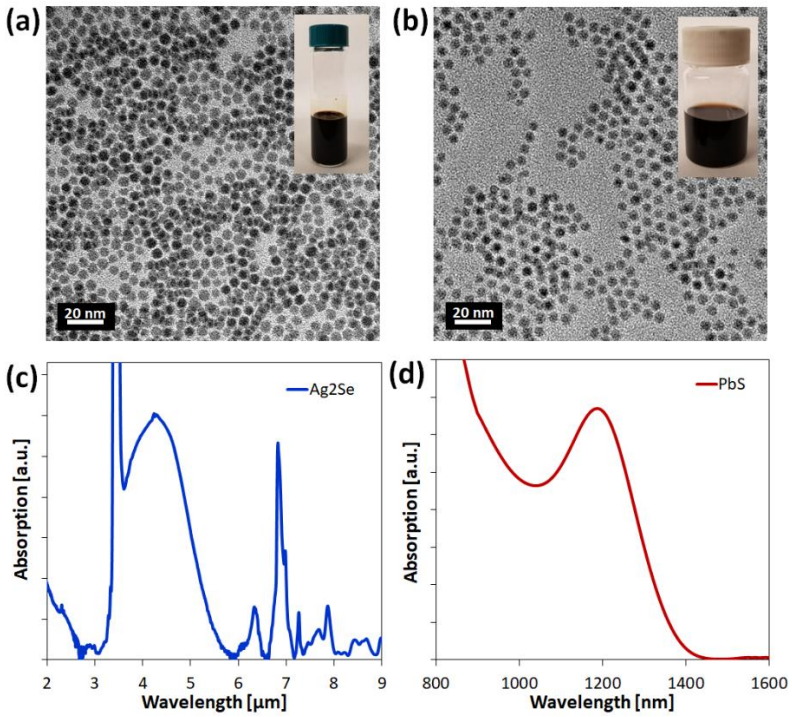

Figure 5.1 Characterization of Ag_2Se and PbS QDs. (a) TEM image of Ag_2Se QDs, (b) TEM image of PbS QDs. The insets in (a,b) show photographs of the synthesized Ag_2Se and PbS QDs suspended in an organic solvent, respectively. (c,d) Optical absorption spectra of the as-synthesized Ag_2Se and PbS QDs, respectively.

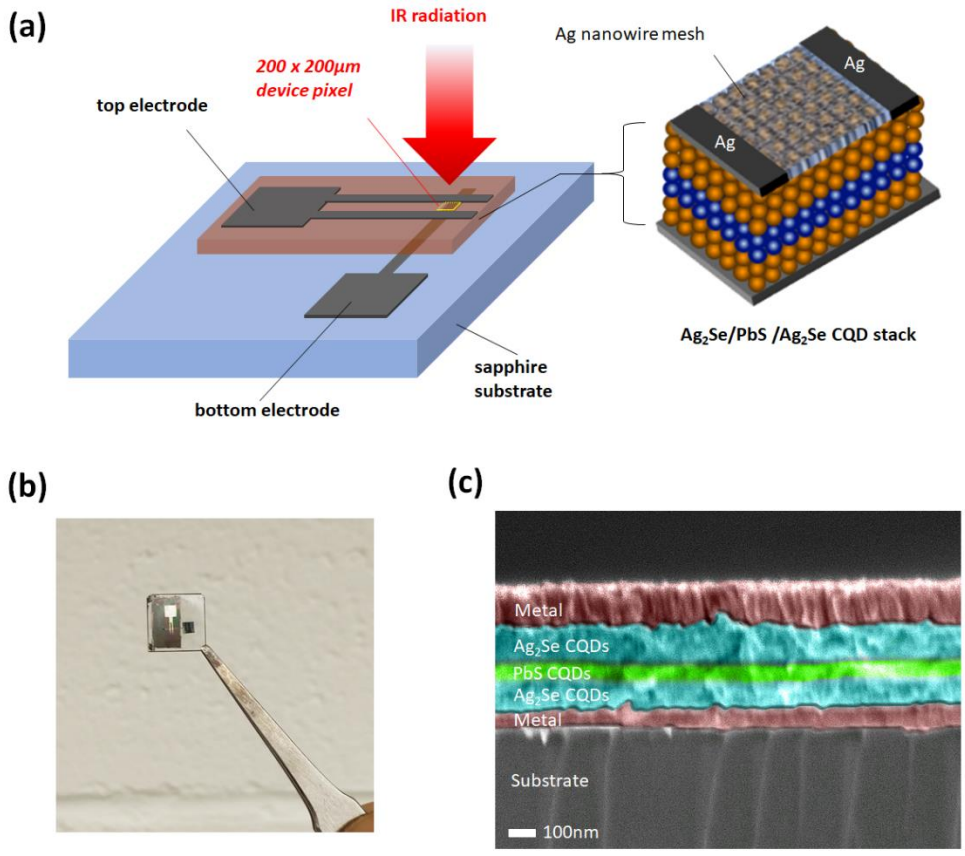

Figure 5.2 Fabrication of vertically stacked QD barrier devices. (a) Schematic of the device structure. (b) Photograph of a fabricated device. (c) False color cross-sectional SEM image of the device showing the sapphire substrate, bottom contact (Ag), QD layers, and top contact (Ag).

To increase the carrier collection in this top-via opening, Ag nanowires [124, 125] were spin-coated using diluted nanowire solution and processed to enhance the nanowire-to-nanowire electrical connection (junction soldering), before depositing the Ag top contact. Here, the nanowire layer serves as an infrared transparent contact. To prepare the nanowire (NW) network film, 0.5 % silver nanowire solution in isopropyl alcohol (diameter × length, 115 nm × 20-50 µm) was used. Ag NW solutions were spin-coated on sapphire substrate to determine optical transmission and sheet resistance, as a function of NW concentration (dilution). Here, percent transmission is determined from FTIR measurement (Thermo Nicolet 370) while sheet resistances were measured using MMR

four probe chamber coupled with Agilent 4155A semiconductor parameter analyzer in a van der Pauw configuration. The sheet resistance of NW network film is majorly determined by the contact resistance at the nanowire-nanowire junction which can be improved by junction welding. We employed capillary force-induced welding of Ag NWs to improve contact resistance [126]. In this method, capillary force is provided by applying moisture to the NW network in which water droplets accumulate to fill up the gap between NWs at the junction. Water evaporation induces an attractive force during drying, which welds NWs to improve the contact of the NW-NW junction. Here, we applied moisture by exposing the Ag NW film to water vapor for 3-5 s and drying for 30 s in air. We observe 70-80% transmission in MWIR (3-5 μm) with sheet resistance varying from 29 Ω/sq to 290 Ω/sq, depending on the dilution of Ag NW solution, as shown in Figure 5.3. Dilution of 10 was used for device fabrication, exhibiting 73% transmission in MWIR with a low sheet resistance of 29 Ω/sq.

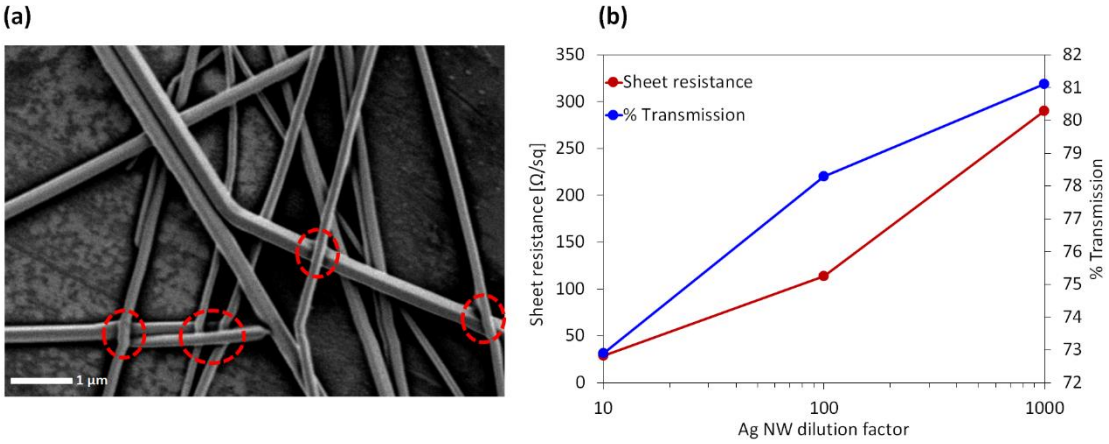

Figure 5.3 (a) SEM image of welded Ag NW-NW junction (red circle) after applying moisture. (b) sheet resistance and percent transmission of Ag NW network as a function of NW concentration in isopropyl alcohol.

5.2.3 Dependency on Ligand Exchange Duration

A critical step in fabricating a MWIR-responsive QD device was optimizing the EDT-ligand exchange duration which was found to have a narrow temporal window. We carried out a systematic investigation of the QD ligand exchange by fabricating a series of devices with ligand exchange duration varying from 0 to 80 s and measuring the device responsivity by illuminating the devices with 4.5 μm radiation. As shown in Figure 5.4a, the infrared responsivity rises and decays rapidly around 10 to 50 s, where a peak is reached at 30 s. Outside this region, around 0 s, QDs in the device are not sufficiently coupled, leading to a device resistance on the order of tens of MΩ. Above 60 s, optical absorption in the MWIR weakens due to reduced electron concentration [50, 86]. In this regard, Figure 5.4b shows optical absorption spectra of Ag_2Se QD film with 1,2-ethanedithiol (EDT) ligand exchange duration varying from 15 to 80 s. The optical absorbance increases and peaks at 30 s, followed by a gradual decrease for prolonged exposure to EDT. At 80 s, the intraband absorbance at 4.5 μm is nearly absent. Similarly, we observe a complete absence of device MWIR responsivity above 60 s. The ligand exchange of Ag_2Se QD films seems to involve a complex interplay [117] of surface chemistry, optoelectronic property, and physical microstructure of the QD film, as discussed more in the next section.

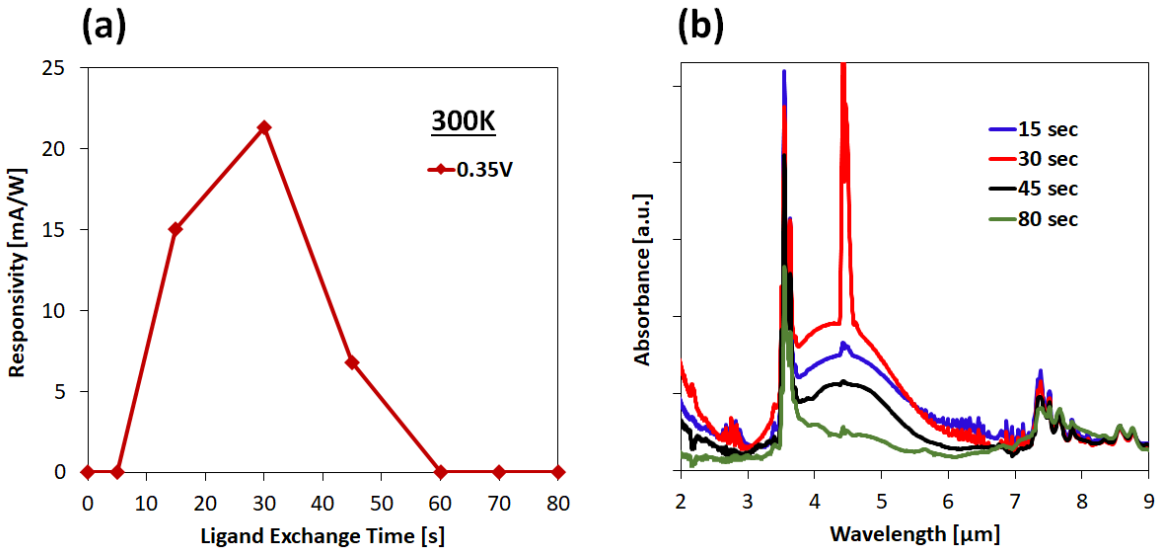

Figure 5.4 (a) Responsivity at 4.5 μm plotted as a function of EDT ligand exchange duration. (b) Optical absorption spectra of Ag_2Se QD film with different durations of EDT ligand exchange.

5.3 Device Characterization

Prior to the photodetector characterization, we carried out basic electrical measurements of our fabricated devices. Figure 5.5a shows the energy-level diagram estimated from prior photoemission spectroscopy measurement reports on similarly sized PbS [127] and Ag_2Se [76] QDs where, in degenerated-doped intraband Ag_2Se QD, $1S_e$ serves as a valence level (ground state) and $1P_e$ serves as conduction level (excited state). An energy-level offset is created by PbS QD, which creates a potential barrier (denoted as Φ_B) for electrons under dark conditions. This is evident in Figure 5.5b where the device resistance increases by 800% through the insertion of the PbS QD barrier layer.

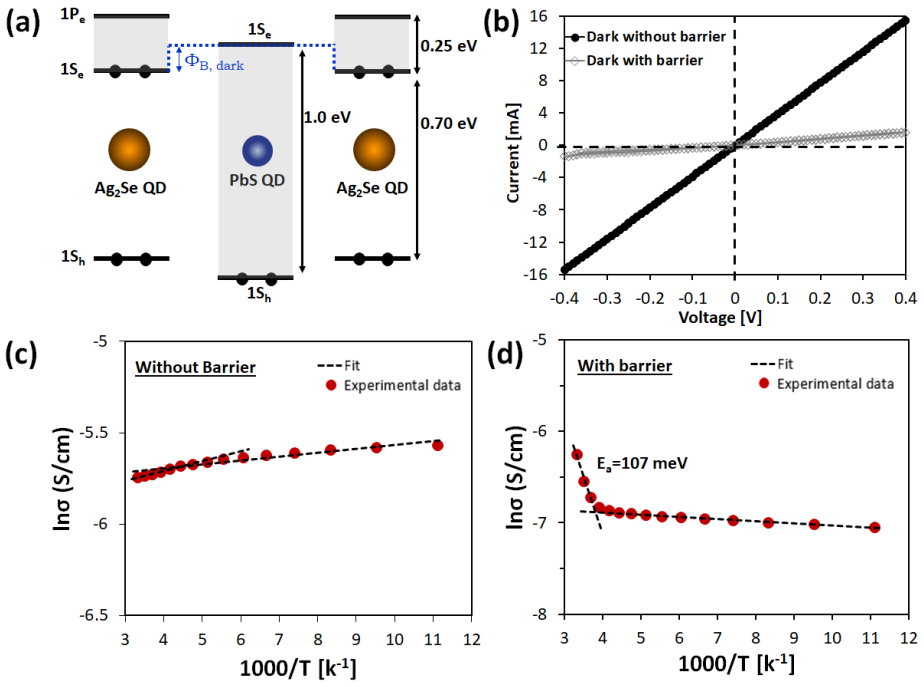

Figure 5.5 Electrical characterization of Ag_2Se/PbS/Ag_2Se QD nBn devices. (a) Schematic of the energy-level alignment of Ag_2Se/PbS/Ag_2Se QD. $1S_h$, $1S_e$, and $1P_e$ denote first valence energy level, first conduction energy level, and second conduction energy level, respectively. The blue dotted line shows the $1S_e$ Ag_2Se QD-$1S_e$ PbS QD conduction offset which serves as a potential barrier (denoted as Φ_B, extracted from our measurements to be 107 meV) for electrons under dark. (b) Current-voltage characteristics obtained under the dark from devices with and without a PbS QD barrier layer. (c,d) Temperature-dependent dark conductivity obtained from device without and with a barrier layer, respectively.

The uniqueness of nBn device design arises from the fact that the metal contact properties do not change with the insertion of the barrier layer since the metals are in contact with the bottom and top n-Ag_2Se QD layers even for barrier devices. This is in agreement with the data in Figure 5.5b, where the dark current-voltage (I-V) characteristics of devices with the barrier layer maintain Ohmic behavior, similar to the I-V obtained from devices without the barrier layer (metal-Ag_2Se QDs-metal photoconductor). In comparison, if the device was designed to be nB or Bn structure, a new metal-barrier layer contact will be formed, and it has been reported that silver (metal) and PbS QDs form Schottky contacts [128]. To better understand the carrier transport in these devices,

temperature-dependent conductivities were measured, as shown in Figure 5.5c. In a typical semiconductor QD film, the conductivity can be expressed as [129]

$$\sigma = q\, N_C \exp\left[\frac{-(E_C - E_F)}{KT}\right] \mu_o \exp\left(\frac{-E_\mu}{KT}\right) \exp\left(-\frac{E_\Phi}{KT}\right) \tag{5.1}$$

where q is the elementary charge, N_C is the effective conduction density of states, E_C is the conduction level, E_F is the Fermi level, and μ_0 is the mobility prefactor. Following this equation, there are three thermal activation energies: (E_C - E_F) related to carrier generation, hopping mobility term E_μ, and E_Φ associated with the presence of potential barrier (for barrier devices). In heavily doped n-type intraband QDs, (E_C - E_F) term can be neglected since the Fermi energy level is positioned close to (or above) the conduction level. Furthermore, for devices without a barrier, shown in Figure 5.5c, a positive slope from 300 to 230 K is observed. This implies that thermally activated hopping is not the transport mechanism. It is plausible that QD necking (while maintaining quantum confinement) may have taken place during the ligand-exchange process [61, 130]. This indicates that the activation energy of hopping mobility, which arises from energy site variations (QD size nonuniformity) [131, 132] can be neglected. The slope from 300 to 230 K in Figure 5.5d is then predominantly related to the energetic height of the potential barrier in nBn devices. From this measurement analysis, the height of the electron potential barrier in the dark is estimated to be Φ_B = 107 meV as denoted in Figure 5.5a. At around 250 K, we observe a change in the slope in Figure 5.5c which is also observed in devices with the barrier (Figure 5.5d). This is expected to be associated with the change in the charge transport mechanism in Ag_2Se QD layers at low temperatures and warrants further study [78, 133].

Photocurrent measurements were conducted by illuminating the device with a calibrated blackbody heated at 900 °C. The blackbody radiation was chopped at 15 Hz and filtered through Ge which only allows mid- to long-wavelength infrared photons (wavelength longer than 1.8 μm) to pass through. The device photocurrent was measured using a preamplifier and lock-in technique. Figure 5.6a shows the photocurrent measured from our QD nBn devices at room temperature. A distinct photoresponse was observed with a photocurrent corresponding to 0.23 μA at 0.35 V of applied bias. It should be noted that, for devices without the barrier, photocurrent measurement was not possible due to the high electrical conductivity (3.2×10^{-3} Scm^{-1}) of the device.

To investigate the detailed photoresponse in the technologically important atmospheric transmission window of 3-5 μm, spectral responsivity measurements were carried out using a set of Fabry-Perot band-pass filters, having center wavelengths (CTs) varying from 2 to 7 μm. Figure 5.6b shows the spectral responsivity of our Ag_2Se/PbS/Ag_2Se QD nBn devices measured without cooling. A good agreement in the spectral shape of our responsivity data and optical absorption of Ag_2Se QDs indicates that the measured photoresponse arises from our Ag_2Se QDs.

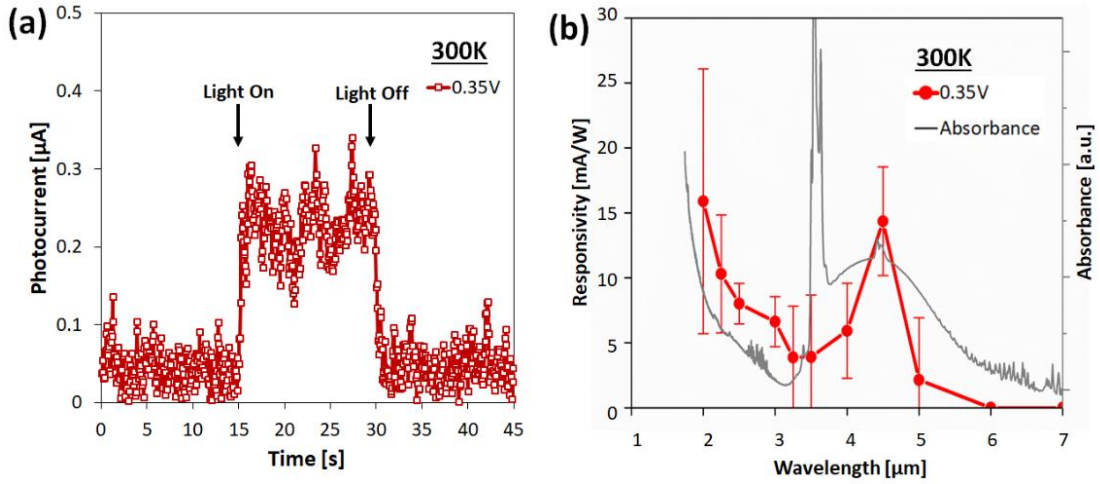

Figure 5.6 Photodetector characterization of Ag_2Se/PbS/Ag_2Se QD nBn devices. (a) Photocurrent measurements carried out using Ge-filtered 900 °C blackbody illumination. (b) Spectral responsivity measured from barrier devices. The data plot was obtained from 5 devices, and variations are represented with error bars. Optical absorbance spectra of Ag_2Se CQD film after ligand exchange is overlaid with the spectral response plot. All measurements were conducted at room temperature 300 K with 0.35 V bias at 15 Hz.

Compared to our previous work on planar photoconductive photodetectors [86], the room-temperature responsivity at 3-5 μm was improved by approximately 70 times. This is mainly attributed to the shorter distance (300 nm) that the photogenerated carriers have to travel in vertical QD-stack devices compared to the 10 μm transport gap in planar photoconductors. The peak responsivity of 13.3 mA/W was measured at 4.5 μm, which corresponds to an external quantum efficiency (EQE) of 0.36%. It is expected that EQE can be improved by increasing light absorption, which can be achieved by developing thicker Ag_2Se QD films or employing other optical trapping strategies [56]. Performance of a photodetector is characterized by the specific detectivity ($D^* = RA^{1/2}/i_n$), where A is the detector area, i_n is the noise current density, and R is the responsivity. The i_n of our QD barrier device was measured using a closed shield at 300 K with a spectrum analyzer where a low-noise preamplifier was used to apply a bias of 0.35 V. The measured value at

15 Hz with 1 Hz bandwidth was 10^{-9} $AHz^{-1/2}$, which is similar to the earlier report on intraband HgSe QD photoconductors [35]. Recent literature on HgSe QDs with improved size dispersion reports in as low as 1 $pAHz^{-1/2}$ measured at 80 K [112]. With the responsivity of 13.3 mA/W at 4.5 μm, our device exhibits a specific detectivity of 3×10^5 Jones at 300 K.

5.4 Optimization of Energy Level Alignment

In the previous section, the electron barrier formed by PbS QD layer was sufficiently high to inhibit the dark current, but the height was not optimized with respect to Ag_2Se QDs. The ideal alignment would be the one shown in Figure 5.7, where the first quantum confined conduction energy level ($1S_e$) of PbS QD coincides with the second quantum confined conduction energy level ($1P_e$) of Ag_2Se QD. This alignment will not only result in a smaller dark current but also increase the photocurrent as the transport barrier for photoexcited electrons are minimized. In QD-based system, energy level alignment can be readily achieved through adjusting the size-dependent quantum confinement via controlling the QD size. We demonstrate this optimization by increasing the size of Ag_2Se QD while keeping the PbS QD size constant thereby moving the $1P_e$ of Ag_2Se QDs closer to $1S_e$ of PbS QDs.

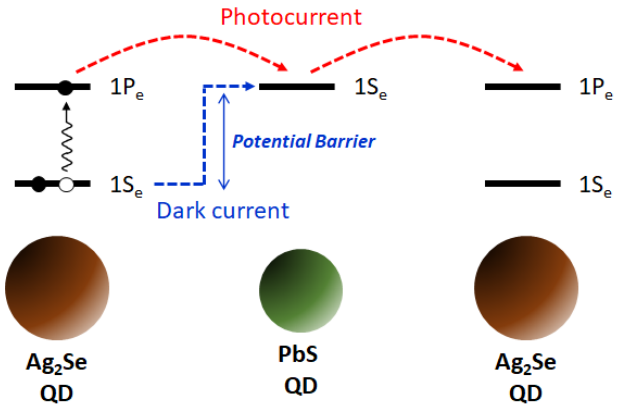

Figure 5.7 Schematic illustration of optimum energy level alignment between Ag_2Se and PbS QDs. $1S_e$ and $1P_e$ denote first conduction energy level and second conduction energy level of respective QDs.

Here, we have synthesized Ag_2Se QDs with absorption peak centered at 4.7 μm modifying previously reported procedure [67, 86]. Compared to the barrier devices fabricated with Ag_2Se QD with absorption peat at 4.2 μm [134], the use of Ag_2Se QD with absorption peak at 4.7 μm leads to the optimization of energy level alignment, which results in 14% improvement in the dark resistivity (Figure 5.8a). While the improvement in the dark resistivity is small, we observe a large enhancement in the infrared response in the device with energy level alignment optimization. Figure 5.8b shows the spectral response of our Ag_2Se/PbS/Ag_2Se QD barrier device measured at room temperature. A good agreement in the spectral shape of our device spectral responsivity data and the optical absorption of Ag_2Se QD (Figure 5.8b) indicates that photocurrent majorly arise from Ag_2Se QDs. Compared to the previous generation of QD barrier devices [134], mid-wavelength infrared responsivity across 3-5 μm was approximately enhanced by 6.3 times. This is mainly attributed to the minimization of transport barrier for photoexcited electrons. A peak responsivity occurs at 4.5 μm with a value of 84.1 mA/W and the corresponding external quantum efficiency (EQE) is 2.32 %. The noise current density of our device was also

measured at room temperature. The measured value at 15 Hz with 1 Hz bandwidth was 10^{-9} $AHz^{-1/2}$ and the resulting specific detectivity (D^*) is 2.6 x10^6 Jones. This is approximately 570 % improvement compared to QD barrier device without energy level alignment optimization.

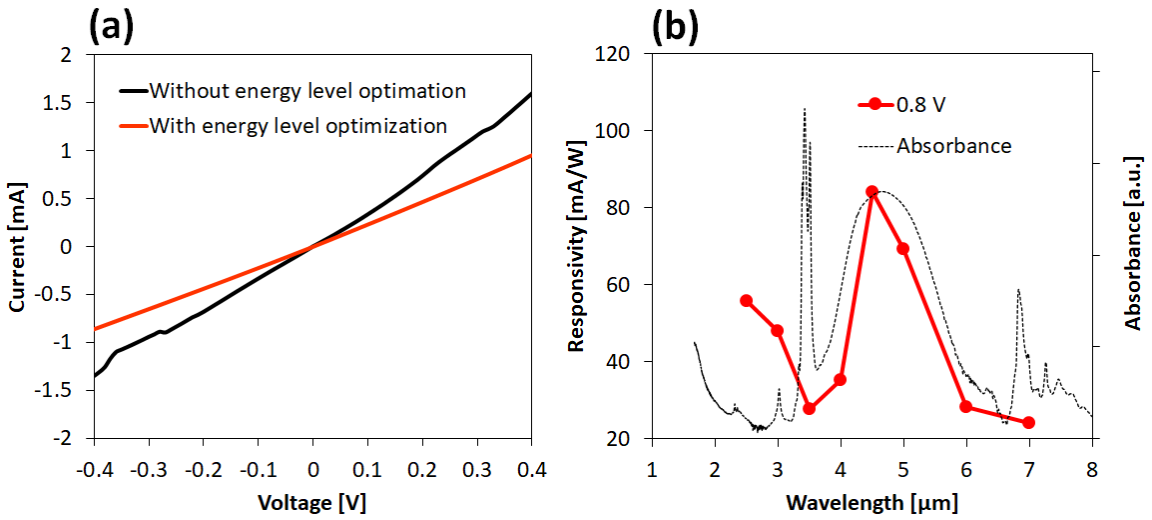

Figure 5.8 (a) Current-voltage characteristics for Ag_2Se/PbS/Ag_2Se QD barrier device with and without energy level alignment under dark. (b) Spectral responsivity obtained from Ag_2Se/PbS/Ag_2Se QD barrier device with energy level alignment. The measurements were conducted at room temperature 300 K with 0.8 V bias at 15 Hz. Optical absorbance spectra of Ag_2Se QD is overlaid for comparison.

Table 5.1 summarizes the performance parameters of our current generation QD barrier devices, along with the comparison to other representative research works. Here, T, λ_{peak}, R, i_n, and D^* denote measurement temperature, peak wavelength, responsivity, noise current density, and specific detectivity, respectively. In addition, we have included the performance of the interband HgTe QD devices (photoconductor and photodiodes), which is currently the leading MWIR QD material.

Table 5.1 Summary of Photodetector Performance Parameters of Ag_2Se /PbS/Ag_2Se QD Barrier Devices and Comparison to Other Representative Research Works

T [K]	QD material (type of absorption)	λ_{peak} [μm]	R [mA/W]	i_n [pAHz$^{-1/2}$]	D^* [Jones]	Device Structure
85	HgTe (interband)	4.5	1620	0.07	$4x10^{11}$	photodiode
138	HgTe (interband)	4	81	0.7	$1.1x10^{10}$	photodiode
80	HgTe (interband)	4.8	230	0.1	$5.4x10^{10}$	photoconductor
300	HgSe (intraband)	6	800	10^3	10^8	photoconductor
80	HgSe (intraband)	5	0.13	1	$2.6x10^7$	photoconductor
80	HgSe (intraband)	4.4	0.1	0.1	$1.5x10^9$	CQDIP
300	Ag_2Se (intraband)	4.5	84.1	10^3	$2.6x10^6$	barrier device

Source: [33, 35, 49, 112. 135, 136].

5.5 Conclusion

In summary, we have presented the QD synthesis, device fabrication, and detector characterization of vertically stacked nBn devices using intraband Ag_2Se QDs as the MWIR absorber and PbS QDs as a barrier layer. More improvements are anticipated by having complementary electron and hole barriers [113] or by incorporating other advanced device designs such as multiple quantum wells that can be fabricated by stacking alternating QD layers vertically [136]. Hence, the QD stack device demonstrated here provides a versatile platform, and its impact may outreach many areas of optoelectronics, including emitters and lasers.

CHAPTER 6

P-N HETEROJUNCTION DIODES BASED ON INTRABAND QUANTUM DOTS

High performance detectors can be realized using a traditional p-n junction device design, however, the heavily-doped nature of intraband quantum dots present a new challenge in realizing diode devices. In this chapter, we utilize a trait uniquely available in colloidal quantum dot material system to overcome this challenge: the ability to blend two different types of quantum dots to control the electrical property of the resulting film. We present the preparation of binary mixture of quantum dot films – intraband Ag_2Se quantum dots as mid-wavelength infrared absorbers and interband PbS quantum dots that acts to reduce the number of free carriers – and the fabrication of p-n heterojunction diodes with strong rectifying characteristics. The peak specific detectivity at 4.5 μm was measured to be 10^7 Jones at room temperature which is orders magnitude improvement compared to the previous generation of intraband quantum dot detectors based on photoconductor or barrier device designs.

6.1 Intraband CQD Based p-n Diode : Potential and Challenges

Using intraband CQDs, high performance infrared sensing device can be fabricated by forming a p-n junction device – a traditional diode device design where built-in electric field established at the junction assist in photoexcited carrier separation and collection [57]. The primary advantage of utilizing p-n diode design lies in the fact that, under typical reverse-biased operation, the dark current is fed by the minority carriers [137]. Compared to photoconductive [72, 86] and barrier device [134, 138] designs, where the majority carriers are responsible for the dark current, p-n junction diode is hence expected to show

significant reductions in the magnitudes of the dark current and noise current density. However, the intraband CQDs also present a new and unique challenge when they used to construct p-n junction devices. To achieve maximum photocarrier collection efficiency, the photodiode is designed such that the depletion region is formed predominantly toward the infrared absorber film where the photoexcited carriers are created upon illumination. The basic semiconductor physics tells us that the width of this depletion region is inversely proportional to the film's carrier concentration [137]. However, since the first conduction energy level ($1S_e$) is occupied with electrons in intraband CQDs, the film exhibit high number of electron carrier concentration (degenerately n-doped) thereby greatly reducing the depletion width formed inside the intraband CQD film. Also, in an electrical point of view, the device will consist of p^+ (heavily-doped p-type layer to induce the formation of depletion region toward to opposite n-type layer) and n^+ (degenerately-doped n-type intraband CQD layer) materials which will rather form a tunnel diode (Esaki diode) [139] that will exhibit high leakage current when reverse-biased, with a weak rectifying characteristic.

Herein, we utilize a trait uniquely available in colloidal quantum dot material system to overcome this challenge. We take advantage of the ability to easily blend two different types of CQDs to control the electrical property of the resulting film. Specifically, we form a mixture of mid-wavelength infrared (MWIR) absorbing intraband Ag_2Se CQDs and interband PbS CQDs that acts to blocks the transports of ground state electrons and holes while providing an unimpeded flow of photoexcited electrons, as depicted Figure 6.1. Using this binary CQD approach, the number of free carriers are greatly reduced (ground state electrons and holes become immobile) which is evidenced by the orders of

magnitude increase in the dark resistivity in Figure 6.2 (binary CQD film: $2x10^5$ Ω·cm vs. Ag_2Se CQD-only film: $1x10^3$ Ω·cm). Also, in junction with ZnO nanoparticle film, which is a layer commonly used to form p-n junction with PbS CQDs in many CQD solar cell studies [13], this binary CQD film will exhibit strong rectifying I-V characteristics. It is worth noting that the unique binary CQD approach presented here can be modified to allow/block the flow of dark/photo carriers by changing the CQD size or employ different types of CQDs [136].

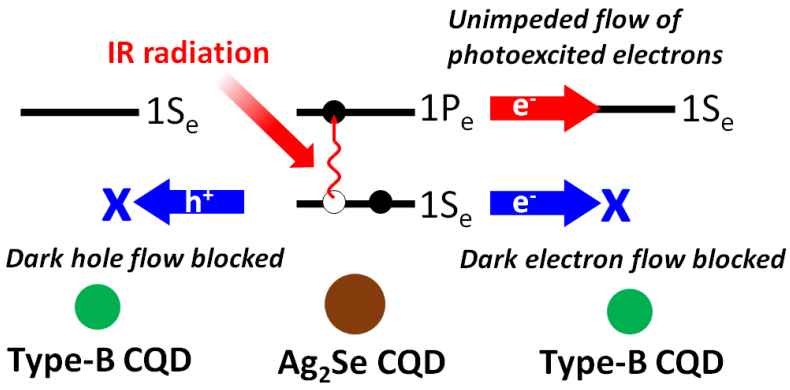

Figure 6.1 A schematic depicting the mechanism whereby creating a binary CQD mixture leads to an increase in dark resistivity while the flow of photoexcited electrons are unimpeded.

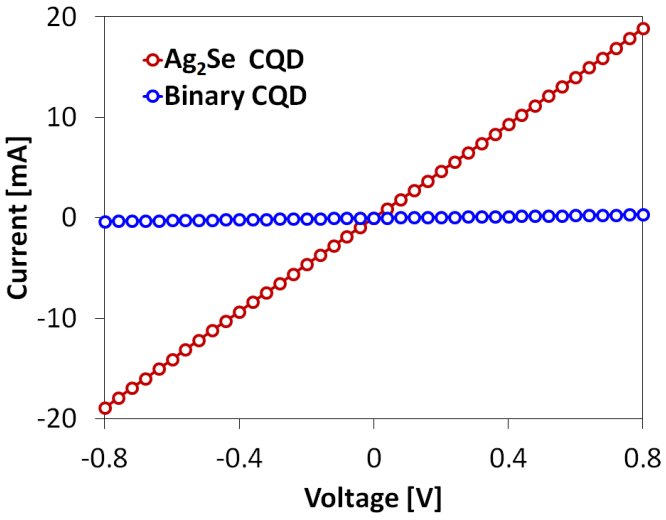

Figure 6.2 Current-Voltage characteristics of photoconductive devices made from binary CQD and Ag_2Se CQD-only film.

6.2 Results and Discussion

6.2.1 Optical Characterization of Binary CQD

Based on our previous study on the energy level alignment between Ag_2Se and PbS CQDs [134, 138], Ag_2Se CQD with average size of 5.5 nm and PbS CQD with average size of 3 nm should create a binary CQD system with decreased dark free carriers (Figure 6.1). First to prepare the CQD materials, Ag_2Se and PbS CQDs were synthesized following previously reported hot-injection protocols [134]. Figure 6.3a shows the mid-infrared optical absorption of films made from as-synthesized Ag_2Se, PbS, and mixed (optimized mixture ratio of $N_{Ag2Se} / N_{PbS} = 0.04$, see more details in Figure 6.7b) CQDs obtained using Fourier transform infrared (FTIR) spectroscopy. The PbS CQDs capped with oleic acid shows absence of absorption in 3.5 – 6 μm spectral range which makes them a good candidate for use in binary CQD approach to modify the film's electrical property. The characteristic peaks around 6.5 μm (1528 cm^{-1}) and 7.2 μm (1398 cm^{-1}) arise from CO_2 and 7.8 μm (1285 cm^{-1}) peak originates from C-O stretch of the oleic acid ligand. The Ag_2Se CQD film show a distinct intraband absorption peak centered at 4.2 μm which optically resides within the transparent window of PbS CQDs. Other characteristic peaks around 3.4, 4.4, and 6.8 μm arises due to vibrational modes of C-H, CO_2, and trioctylphosphine (TOP), respectively. The film composed of binary PbS/Ag_2Se CQD mixture shows the sum of PbS and Ag_2Se absorption, where MWIR absorption peak at 4.2 μm arising from Ag_2Se CQD is still predominant. Figure 6.3(b) shows optical spectra in the visible to near infrared spectral region obtained from the same CQDs. The PbS CQD shows an absorption peak at 1000 nm which is in agreement with the CQD size of 3 nm [140]. On the other hand, Ag_2Se CQDs show a continuous increase in absorbance with decreasing wavelength as the

density of states increase with increasing energy. The binary CQD mixture sample shows a spectra that combines the optical absorption arising from Ag_2Se and PbS CQDs.

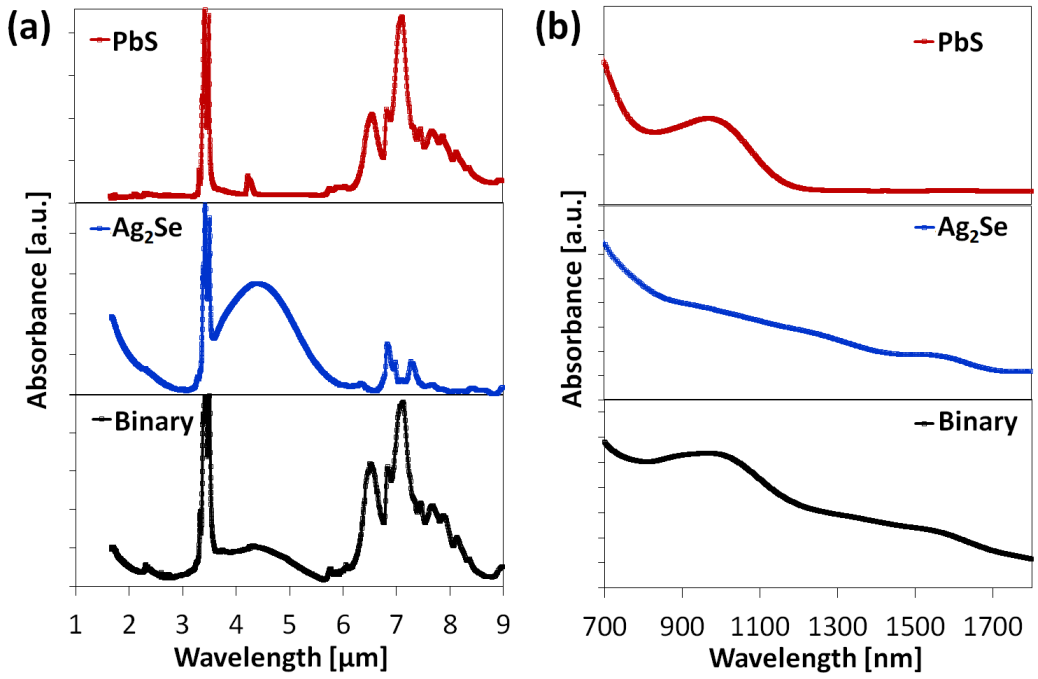

Figure 6.3 Optical absorbance characterization of as-synthesized PbS, Ag_2Se and PbS/Ag_2Se mixture CQDs using (a) Fourier transform infrared (FTIR) and (b) visible-near Infrared spectroscopies.

6.2.2 Design and Fabrication of p-n Heterojunction Diode

Design and fabrication: To fabricate the device, Cr/Au electrode is first pre-patterned on a glass substrate using a shadow mask to form a bottom contact. Then, a thin layer of MoO_x (15 nm) is deposited by thermal evaporation. MoO_x has been frequently used in PbS CQD solar cell devices to improve contact between PbS CQD and the metal electrode [141, 142]. We adopt this approach in our devices since our binary CQD layer majorly composes of PbS CQDs in which Ag_2Se CQDs are embedded sparsely as MWIR absorbers or sensitizers. Next, binary PbS/Ag_2Se CQD layer was deposited using spin-casting and a ligand-exchange procedure using 1,2-ethanedithiol (EDT) was carried out to improve the electronic coupling between CQDs [90]. The thickness of binary CQD layer was increased

by repeating this step 10-12 times to create a 200 nm-thick film. It is worth noting that, ligand exchange duration is not a critical processing parameter for binary CQD devices. Devices fabricated from pure Ag_2Se CQDs, in contrast, showed a narrow temporal window that exhibits the maximum MWIR responsivity [134]. This can be understood reflecting the fact that the majority component of our binary CQD film is PbS CQDs. To form a p-n junction, ZnO nanoparticles were synthesized following the literature report [143, 144] and spin-casted on top of binary CQD layer with a thickness of 80 nm. To complete the device, Al top contact having two finger electrodes was deposited through a shadow mask. The top opening created by the fingers defines our device's optical area of 200 x 200 μm. A schematic illustration of this upward-looking photodiode is shown in Figure 6.4a and the cross-sectional scanning electron microscope (SEM) image of the device is shown in Figure 6.4b. Figure 6.5a shows the energy level alignment of our binary CQD p-n junction device materials before contact. After contact, ZnO - PbS CQD n-p junction [145] will establish a built-in electric field ($\vec{E}$) toward the binary CQD layer where the Ag_2Se CQDs reside in (Figure 6.5b). Under bias and with infrared illumination, photoexcited electrons generated from the Ag_2Se CQDs will cascade down toward the Al cathode, bearing a resemblance to the operation of epitaxial quantum dot infrared photodetectors (QDIPs) [146, 147] as illustrated in Figure 6.5c.

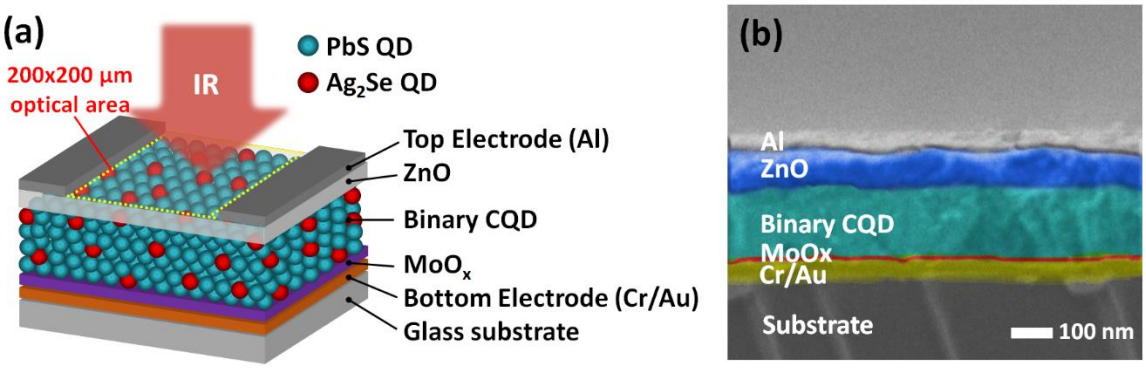

Figure 6.4 Fabrication of p-n junction diode using binary CQD. (a) Schematic illustration of device structure which consists of glass substrate, bottom contact (Cr/Au), MoO_x layer, PbS/Ag_2Se CQD mixture layers, ZnO nanoparticle layer, and top contact (Al). (b) shows a false color cross-sectional SEM image of the fabricated device.

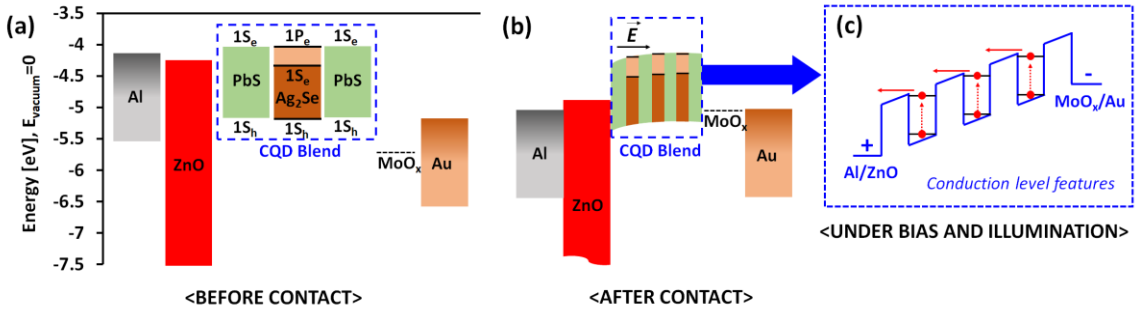

Figure 6.5 Schematic of the energy-level diagram of Au/MoO_x/CQD blend/ZnO/Al p-n junction device. (a) shows the energy level alignment before contact. $1S_h$, $1S_e$, and $1P_e$ denote first valence energy level, first conduction energy level, and second conduction energy level, respectively. (b) shows the equilibrium energy level diagram after contact. $\vec{E}$ denotes the built-in electric field. (c) depicts the conduction level features of binary CQD system under bias and with infrared illumination.

Synthesis of ZnO nanoparticles: ZnO nanoparticles were synthesized by following the literature method [143, 144]. In this procedure, 1.4 g of zinc acetate dihydrate ($Zn(CH_3COO)_2 . 2H_2O$) was dissolved in 60 mL methanol and the solution was transferred to a three-neck flask at 65 °C. Then, 0.70 g of potassium hydroxide (KOH) was dissolved in 30 mL methanol and the solution was added drop wise to the zinc acetate solution for about 5 min with constant stirring. A milky white solution was obtained after stirring the mixture for 2 h 30 min at 65 °C. The mixture was naturally cooled for 1 h. Finally, the ZnO

nanoparticles were precipitated by centrifugation and dissolved in 5 mL chloroform to prepare a optically-transparent solution.

Figure 6.6 shows Fourier transform infrared (FTIR) spectrum of ZnO nanoparticle film prepared on a KBr card. The broad peak at 3-3.5 μm (peak 1) comes from hydroxyl (OH) group [148]. Other characteristic peak at 6.7 μm (peak 2) , 7.7 μm (peak 3) and 8.1 μm (peak 4) arise due to the presence of C-H stretch, primary and secondary alcohol, respectively [149]. The absorbance of Ag_2Se CQD film is overlaid to show that the primary 4.2 μm absorbance peak of Ag_2Se CQDs reside outside the major absorbance peaks produced by ZnO nanoparticle film.

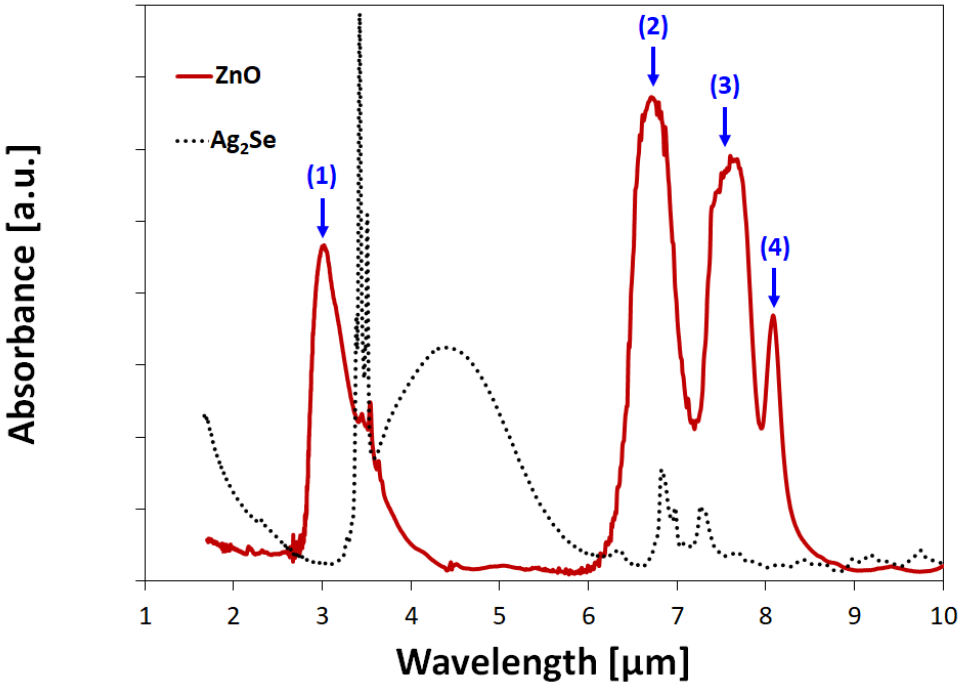

Figure 6.6 Fourier transform infrared (FTIR) spectrum of ZnO nanoparticle film. The absorbance of Ag_2Se CQD film is overlaid.

Binary CQD Mixing Ratio (N_{Ag2Se} : N_{PbS}): We fabricated p-n junction diode devices with varying binary CQD mixture ratio. To determine the mixture ratio, the weight of the Ag_2Se

and PbS CQD were measured, denoted respectively as W_{Ag2Se} and W_{PbS}, in gram (g). The weight of the CQD is represented by (Weight = Volume X Density). Then, the weight of the CQD can be represented as:

$$W_{Ag2Se} : W_{PbS} = (N_{Ag2Se} \text{ X } V_{Ag2Se}) \text{ X } D_{Ag2Se} : (N_{PbS} \text{ X } V_{PbS}) \text{ X } D_{PbS} \quad (6.1)$$

where, W_{Ag2Se}: Measured weight of the Ag_2Se QD in the mixture; W_{PbS}: Measured weight of the PbS QD in the mixture; N_{Ag2Se}: Total number of Ag_2Se QDs; N_{PbS}: Total number of PbS QDs.

Considering volume of a single quantum dot ($V_{Ag2Se}={}^{4}/_{3}\,\pi({}^{D}/_{2})^{3}$), where D is the diameter of the quantum dot. Volume of a single Ag_2Se QD (V_{Ag2Se}) is calculated to be 8.71×10^{-20} cm^3 with considering a diameter of 5.5 nm. Similarly, Volume of a single PbS QD (V_{PbS}) is calculated to be 1.72×10^{-20} cm^3 considering a diameter of 3.2 nm. Using bulk density values of D_{Ag2Se}: Density of Ag_2Se (8.22 g/cm^3) and D_{PbS}: Density of PbS (7.61 g/cm^3), we use equation (6.1) to obtain CQD number ratio as follows:

$$N_{Ag2Se} : N_{PbS} = \frac{W_{Ag2Se}}{W_{PbS}} \times \frac{(V_{PbS}) \times (D_{PbS})}{(V_{Ag2Se}) \times (D_{Ag2Se})} \quad (6.2)$$

6.2.3 Electrical Characterization

Prior to the photodetector performance characterizations, we carried out basic electrical measurements of our p-n junction diode devices, under dark, with varying binary CQD mixture ratio. The ratio of $N_{Ag2Se} / N_{PbS} = 0.25$, for example, denotes a CQD film having

25 Ag_2Se CQDs per 100 PbS CQDs. A series of current-voltage (I-V) characteristics were obtained (Figure 6.7a) and were fitted to a standard diode equation [150]

$$I = I_o \left\{ \exp\left[\frac{q}{nkT}(V - IR_s)\right] - 1 \right\} + \frac{V - IR_s}{R_{sh}} \tag{6.3}$$

where n is the ideality factor, I_o is the dark saturation current , R_s is the series resistance, and R_{sh} is the shunt resistance. We extract four key diode parameters as summarized in Table 6.1.

Table 6.1 Summary of Diode Parameters Extracted from I-V Characteristics

N_{Ag2Se}/N_{PbS}	**Ideality Factor (n)**	**Saturation Current I_o (A)**	**Shunt Resistance R_{sh} (Ω)**	**Series Resistance R_s (Ω)**
0	3.2	3.0×10^{-10}	1.7×10^{5}	4.7×10^{2}
0.01	3.8	5.0×10^{-8}	7.6×10^{4}	2.6×10^{2}
0.04	3.2	5.2×10^{-8}	2.7×10^{3}	0.9×10^{2}
0.1	3.7	9.5×10^{-8}	2.2×10^{3}	1.6×10^{2}
0.16	3.4	4.0×10^{-6}	1.5×10^{3}	0.4×10^{2}
0.25	3.8	8.0×10^{-6}	0.9×10^{3}	0.5×10^{2}

First, we observe that all diodes exhibit ideality factor (n) larger than 3. While n typically varies between 1 and 2, $n > 3$ is also frequently reported in diodes with non-ideal electrical contacts [151]. The existence of p-n junction and another opposing junction, for example, created at the metal-p contact can induce $n > 3$ because the extracted value of n becomes a summation of two ideality factors arising from each individual junctions [152, 153]. This indicates that, in our device, there is a presence of additional junction created at Al/ZnO or binary CQD/MoO_x-Al junction or both and require further contact optimization to improve the diode. In regard to the reverse saturation current I_0, we observe a distinct

trend where increasing Ag_2Se CQD loading (increasing N_{Ag2Se} / N_{PbS} ratio) increases the magnitude of I_0. The value I_0 is indicative of how much recombination there are in the p-n junction device [154, 155]. This suggests that as we increase the number of Ag_2Se CQDs in the binary CQD film, Ag_2Se CQD itself or the surface defects associated with Ag_2Se CQD increases the rate of carrier recombination inside the device. This, in turn, influences the optimum binary CQD mixture ratio that yields the highest MWIR peak responsivity in our diode devices, as shown in Figure 6.7b. The Figure 6.7b shows the peak 4.5 μm responsivity of our diode device as a function of N_{Ag2Se} / N_{PbS} ratio. At N_{Ag2Se}:N_{PbS} = 0, the absence of MWIR-absorbing Ag_2Se CQD induces zero photocurrent at 4.5 μm. As we increase the Ag_2Se CQD loading, the peak responsivity increases because more Ag_2Se CQDs will produce larger number of photoexcited carriers upon infrared illumination. However, as we increase the Ag_2Se CQD loading further, increase in the photocarrier generation will compete with the increase in the carrier recombination. It is observed that for N_{Ag2Se} / N_{PbS} > 0.04, the peak responsivity starts to decrease, suggesting that the carrier recombination arising from Ag_2Se CQDs starts to overweight the optical generation. Hence, we observe a peak at N_{Ag2Se} / N_{PbS} = 0.04 which we define as the optimum binary CQD mixture ratio for MWIR detection. Another important diode parameter of a p-n junction is the shunt resistance R_{sh}, which arises from the presence of electrical shunt path (current leakage) through the p-n junction [156]. In our devices, high R_{sh} is observed for pure CQD film (N_{Ag2Se} / N_{PbS} = 0) and R_{sh} decrease with increasing Ag_2Se CQD loading. This can be understood reflecting the fact that, in our binary CQD system, as more Ag_2Se CQDs are introduced, the probability of Ag_2Se CQDs creating a direct percolation path (a highly conductive path since Ag_2Se CQDs are degenerately n-doped) are more frequently

created inside the film. Figure 6.8 shows appearance of shunt current path with increasing Ag_2Se CQD loading in the binary CQD blend. When N_{Ag2Se}:N_{PbS} is low, Ag_2Se CQD is sparsely distributed inside the binary CQD film but as the Ag_2Se CQD loading increase, the probability of creating a direct shunt path (high conductive path since Ag_2Se CQD is degenerately-doped n-type) between the top n-type ZnO and bottom metal contact. The filament created in the binary CQD will serve as effective shunt component that penetrate directly through the p-n junction diode because this conduction path is consist of n-type ZnO / n-type Ag_2Se CQD / metal contact. Further increase in Ag_2Se loading (N_{Ag2Se}:N_{PbS} = high) creates more number of shunt current path. Lastly, the series resistance R_s is indicative of additional series resistance component present in the device, typically arising from high contact resistances [154]. For R_s, we do not observe any particular trend with Ag_2Se CQD loading and all the devices show a magnitude of R_s around 10^2 Ω.

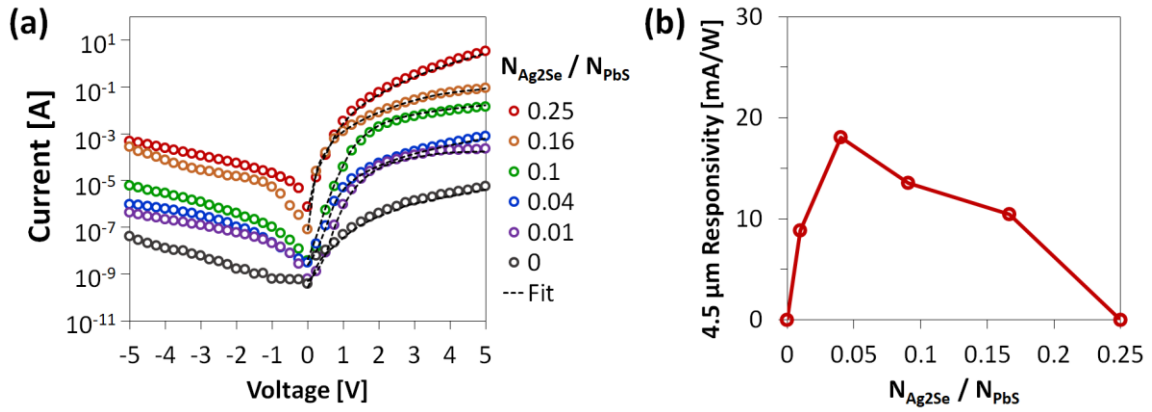

Figure 6.7 Electrical characterization of binary CQD p-n junction diodes. (a) A series of dark I-V characteristics obtained from diodes with different binary CQD mixing ratio. The open symbols are experimental data, while the dashed lines are the fittings based on the diode equation. (b) Responsivity at 4.5 µm plotted as a function of binary CQD mixing ratio.

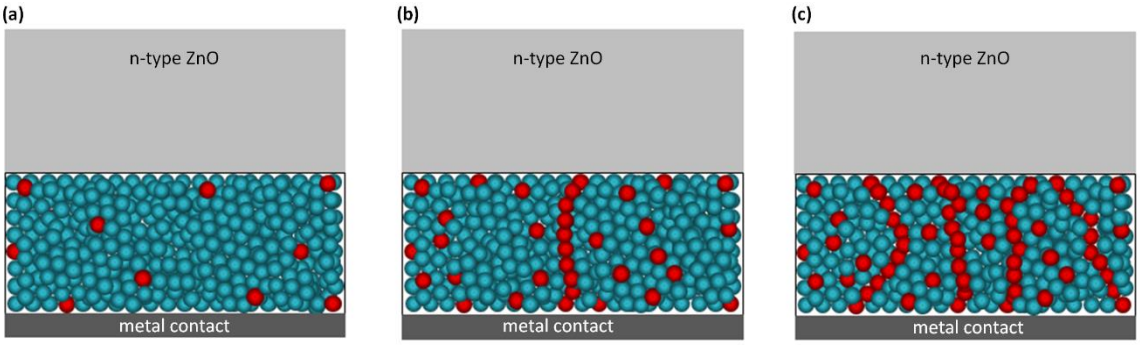

Figure 6.8 Schematic illustration of the evolution of shunt current path created by increasing Ag_2Se CQD loading for (a) N_{Ag2Se}:N_{PbS} = low, (b) N_{Ag2Se}:N_{PbS} = medium, and (c) N_{Ag2Se}:N_{PbS} = high. Red spheres represent Ag_2Se CQDs and cyan spheres represent PbS CQDs.

6.2.4 Photodetector Characterization

Using diode device with the optimum binary CQD mixing ratio identified in Figure 6.7b (N_{Ag2Se} / N_{PbS} = 0.04), we characterized the detector performance parameters using the infrared illumination provided by calibrated blackbody heated at 900 °C, filtered through a Ge which cuts of photons with wavelength smaller than 1.8 μm. Figure 6.9a shows the diode I-V characteristics obtained under dark and under infrared illumination conditions. The dark I-V shows a strong rectifying characteristics with on/off ratio of 6×10^3 at $\pm$5 V. Upon illumination, the device showed a distinct increase in the reverse-biased current with a photovoltage of 250 meV. Figure 6.9b shows the spectral responsivity of the device collected at room temperature by replacing the Ge filter with a set of band-pass filters with center wavelengths varying from 2.5 – 7 μm and measuring the photocurrent using a lock-in technique. The magnitude of photocurrent (~ 0.2 μA) estimated from the difference between the dark and light curve at reverse bias of – 2.0 V, closely matches with the photocurrent (~ 17 μA) calculated by integrating the area under the curve of spectral photocurrent data extracted from responsivity spectra at corresponding bias of – 2.0 V. The peak responsivity is obtained at 4.5 μm with the magnitude of the responsivity increasing

with increasing reverse bias and reaches a value of 19 mA/W at – 4 V. The noise current density (i_n) is measured to be 4.91 x 10^{-11} $AHz^{-1/2}$ (in 1 Hz bandwidth) using a spectrum analyzer. Using these values, specific detectivity is calculated to be 7.8 × 10^6 Jones at 300K. This is 30 times increase over our previous generation of barrier devices [134]. This improvement is mainly attributed to the reduced dark current and noise current density, an advantageous device property offered by reverse-biased p-n junction diodes.

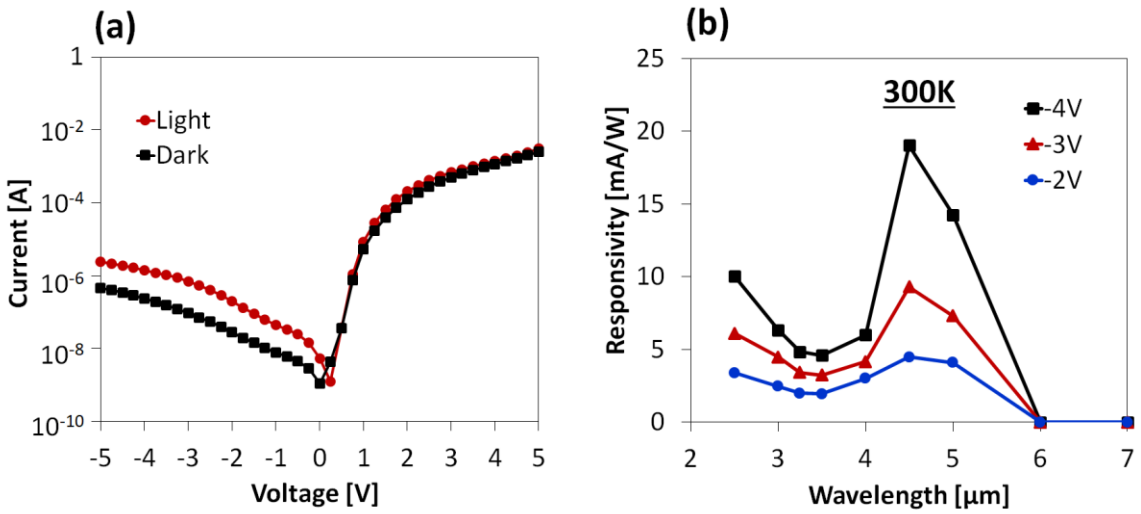

Figure 6.9 Detector performance characterization of binary CQD diode devices with optimized CQD mixture ratio. (a) shows the I-V characteristics of the device under dark and under infrared illumination. The illumination was provided by 900 °C calibrated blackbody with Ge filter. (b) shows the spectral responsivity measured at various bias voltages. All devices were measured at room temperature 300K.

6.3 Conclusion

In summary, we have demonstrated intraband CQD-based photodiodes exhibiting a strong rectifying characteristic and reduced dark current and noise current density, with MWIR detectivity reaching 10^7 Jones without cooling. This was enabled by our binary CQD approach which helped to overcome the issue arising from degenerately-doped nature of intraband Ag_2Se CQDs. Further improvements in the device performance are anticipated

through optimizing the contact properties and investigating various surface capping ligands that can enhance the CQD passivation or carrier mobilities [101, 157, 158, 159].

CHAPTER 7

SUMMARY AND FUTURE WORK

Existing thermal infrared sensing and imaging technologies are primarily dominated by epitaxial technologies that are ill-suited for wide-scale adoption due to high cost of material preparation, complex device fabrication process and requirement for cryogenic cooling. Specifically, epitaxial technologies are expensive method for single-crystal growth, and are incompatible with mature silicon technology that prohibits monolithic device fabrication resulting in low production yield and high cost. Additionally, the requirement for cryogenic cooling is costly to implement, require high input power, and significantly increases the size and weight of the detector that limits their wide-scale applicability.

Consequently, this dissertation presents intraband colloidal quantum dot-based photodetector to overcome these limitations. The intraband colloidal quantum dots (CQDs) are a new family of semiconductor CQD material that utilizes optical transitions between the first ($1S_e$) and the second ($1P_e$) quantum confined energy levels. The optical gap of $1S_e$-$1P_e$ can be varied through controlling the CQD size, similar to the traditional interband CQDs, and their absorption peak can span a wide range in the mid- to long-wavelength infrared spectral region. The solution processability of these CQDs also allow low-cost, low-temperature, and large-area fabrication of optoelectronic films which can enable high-throughput manufacturing of focal plane arrays or construct sensors on a flexible platform. In addition, suppression of Auger recombination process in intraband CQD system can lead to high temperature operation of photodetectors thereby removing the need for bulky, high-power consuming cryogenic cooling system.

In this dissertation, newly discovered silver selenide (Ag_2Se) CQDs, which are a non-toxic alternative to current state of the art Hg-based CQDs, have been investigated in mid-wavelength infrared spectral region with detailed material, electrical and device characterization. Here, mid-wavelength infrared photodetection has been demonstrated with Ag_2Se CQDs by three device architectures with detailed analysis of detector performance parameters. In the first device architecture (lateral photoconductor), we have obtained responsivity of 200 μA/W (bias voltage 0.2 V) at room temperature (300 K) at 4.5 μm wavelength. There was one prior work by Qu et al [76] on similar device architecture, where they obtained responsivity of 8 μA/W (bias voltage 0.2V) at similar wavelength but at low temperature (<200 K). Next, we have developed vertically stacked quantum dot devices, where PbS QD layer was inserted in between Ag_2Se QD layers. The insertion of barrier layer reduced dark current significantly since $1S_e$ Ag_2Se QD-$1S_e$ PbS QD conduction offset served as a potential barrier, blocking the transport of thermally generated electrons and holes. Additionally, responsivity was improved by 70 times and reached to the value of 13.3 mA/W at 4.5 μm (300 K) with specific detectivity of 3×10^5 Jones. Lastly, we have developed p-n heterojunction diode devices, employing an unique trait of blending two different QDs to control electrical property. The reverse bias operation of p-n junction ensured reduced noise current density, which improved the specific detectivity to reach 10^7 Jones at room temperature. In addition, we have presented a detailed investigation on correlation between effect of surface capping ligands of Ag_2Se CQDs and mid-wavelength infrared responsivities. Hence, this dissertation presents a complete investigation on the prospect of mid-wavelength infrared photodetection with

intraband silver selenide quantum dots, which may introduce new dimensions to the current thermal infrared sensing and imaging applications.

The future work has been planned to improve detector performance more by employing different strategies based on surface chemistry and device design. Two distinct strategies can be adopted to enhance detector responsivity: (1) maintaining ideal doping condition in Ag_2Se CQD ($1S_e$ level fully filled with carriers) and (2) increasing light absorption. To maintain ideal doping, surface passivation is a promising strategy, which can be implemented by growing ZnSe shell around Ag_2Se core. This approach will concentrate the charge carriers in the CQD core and away from the surface. Another approach is to develop hybrid ligand exchange procedure (use of both organic and inorganic ligand) [135].

To increase light absorption, thicker Ag_2Se CQD film should be developed and optimized for device integration. Another approach is to develop optical trapping strategies such as plasmonic nano disk array [56] or matching the carrier diffusion length with inter-electrode spacing [160]. Further improvement can be demonstrated by employing Ag_2Se CQD sandwiched between complimentary electron and hole barrier [113] or increasing depletion width resembling p-i-n structure, resulting in higher light absorption in depletion region [118].

REFERENCES

[1] W. Herschel, "Experiments on the refrangibility of the invisible rays of the sun," *Philosophical Transactions of the Royal Society of London*, vol. 90, pp. 284-292, 1800.

[2] P. Guyot-Sionnest, M. M. Ackerman, and X. Tang, "Colloidal quantum dots for infrared detection beyond silicon," *Journal of Chemical Physics*, vol. 151, no. 6, pp. 060901, 2019.

[3] A. Rogalski and K. Chrzanowski, "Infrared devices and techniques (revision)," *Metrology and Measurement System*, vol. 21, no. 4, pp. 565-618, 2014.

[4] B. P. Rand, J. Xue, F. Yang, and S. R. Forrest, "Organic solar cells with sensitivity extending into the near infrared," *Applied Physics Letters*, vol. 87, no. 23, pp. 233508, 2005.

[5] L. Bready, S. Noorily, and D. Dillman, *Decision Making in Anesthesiology, Fourth Edition*, Maryland Heights, MO: Mosby Elsevier, 2007.

[6] C. Rablau, "LIDAR - A new (self-driving) vehicle for introducing optics to broader engineering and non-engineering audiences," *Proceeding of SPIE: Conference of Education and Training in Optics and Photonics*, vol. 11143, pp. 111430C, 2019.

[7] L. Seravalli, G. Trevisi, and P. Frigeri, "Design and growth of metamorphic InAs/InGaAs quantum dots for single photon emission in the telecom window," *CrystEngComm*, vol. 14, no. 20, pp. 6833-6838, 2012.

[8] J. Wolf, "Low-background far-infrared detectors and arrays," *Optical Engineering.*, vol. 33, no. 5, pp. 1492-1500,1994.

[9] J. Y. Kim, O. Voznyy, D. Zhitomirsky, and E. H. Sargent, "25th anniversary article: Colloidal quantum dot materials and devices: A quarter-century of advances," *Advanced Materials*, vol. 25, no. 36, pp. 4986–5010, 2013.

[10] C. R. Kagan, E. Lifshitz, E. H. Sargent, and D. V. Talapin, "Building devices from colloidal quantum dots," *Science*, vol. 353, no. 6302, pp. aac5523, 2016.

[11] D. A. Neaman, *Semiconductor Physics and Devices: Basic Principles, Fourth Edition*, New York City, NY: McGrawHill, 2012.

[12] J. M. Pietryga, Y.-S. Park, J. Lim, A. F. Fidler, W. K. Bae, S. Brovelli, and V. I. Klimov, "Spectroscopic and device aspects of nanocrystal quantum dots," *Chemical Reviews*, vol. 116, no. 18, pp. 10513-10622, 2016.

[13] E. H. Sargent, "Colloidal quantum dot solar cells," *Nature Photonics*, vol. 6, no. 3, pp. 133-135, 2012.

[14] K. F. Chou and A. M. Dennis, “Förster resonance energy transfer between quantum dot donors and quantum dot acceptors,” *Sensors (Switzerland)*, vol. 15, no. 6, pp. 13288–13325, 2015.

[15] M. C. Weidman, M. E. Beck, R. S. Hoffman, F. Prins, and W. A. Tisdale, “Monodisperse, air-stable PbS nanocrystals via precursor stoichiometry control,” *ACS Nano*, vol. 8, no. 6, pp. 6363-6371, 2014.

[16] A. Rogalski, “Infrared detectors: status and trends,” *Progress in Quantum Electronics*, vol. 27, no. 2–3, pp. 59-210, 2003.

[17] A. Rogalski, J. Antoszewski, and L. Faraone, “Third-generation infrared photodetector arrays,” *Journal of Applied Physics*, vol. 105, no. 9, pp. 091101, 2009.

[18] N. R. Council, *Expanding the Vision of Sensor Materials*. Washington, DC: The National Academies Press, 1995.

[19] C. Downs and T. E. Vandervelde, “Progress in infrared photodetectors since 2000,” *Sensors (Switzerland)*, vol. 13, no. 4, pp. 5054-5098, 2013.

[20] A. Rogalski, “HgCdTe infrared detector material: history, status and outlook,” *Reports on Progress in Physics*, vol. 68, no. 10, p. 2267-2336, 2005.

[21] Q. Huang, G. Xu, Y. Yuan, X. Cheng, and L. Luo, “Development of indium bumping technology through AZ9260 resist electroplating,” *Journal of Micromechanics and Microengineering*, vol. 20, no. 5, pp. 055035, 2010.

[22] E. J. D. Klem, C. Gregory, D. Temple, and J. Lewis, “PbS colloidal quantum dot photodiodes for low-cost SWIR sensing,” *Proceeding of SPIE: Infrared Technology and Applications XLI*, vol. 9451, pp. 945104, 2015.

[23] R. Saran and R. J. Curry, “Lead sulphide nanocrystal photodetector technologies,” *Nature Photonics*, vol. 10, no. 2, pp. 81–92, 2016.

[24] J. P. Clifford, G. Konstantatos, K. W. Johnston, S. Hoogland, L. Levina, and E. H. Sargent, “Fast, sensitive and spectrally tuneable colloidal-quantum-dot photodetectors,” *Nature Nanotechnology*, vol. 4, no. 1, pp. 40–44, 2009.

[25] D. S. Temple, A. Hilton, and E. J. D. Klem, “Towards low-cost infrared imagers: how to leverage Si IC ecosystem,” *Proceeding of SPIE:Technologies for Optical Countermeasures XIII*, vol. 9989, pp. 99890E, 2016.

[26] C. Buurma, R. E. Pimpinella, A. J. Ciani, J. S. Feldman, C. H. Grein, and P. Guyot-Sionnest, “MWIR imaging with low cost colloidal quantum dot films,” *Proceeding of SPIE: Optical Sensing, Imaging, and Photon Counting: Nanostructured Devices and Applications*, vol. 9933, p. 993303, 2016.

[27] A. Rogalski and K. Chrzanowski, “Infrared devices and techniques,” *Opto-Electronics Review*, vol. 10, no. 2, pp. 111–136, 2002.

[28] Xenics Infrared Solutions, “See Through Smoke”, [online] Available:https://www.youtube.com/watch?v=Oj22mr_A20U [Accesssed: July. 6, 2021].

[29] R. D. P. M. Scafutto and C. R. de S. Filho, “Detection of methane plumes using airborne midwave infrared (3-5 μm) hyperspectral data,” *Remote Sensing*, vol. 10, no. 8, pp. 1237, 2018.

[30] S. Bagavathiappan, T. Saravanan, J. Philip, T. Jayakumar, B. Raj, T. M. R. Panicker, M. P. Korath, and K. Jagadeesan, “Infrared thermal imaging for detection of peripheral vascular disorders,” *Journal of Medical Physics*, vol. 34, no. 1, p. 43-47, 2009.

[31] A. Haddadi, S. Adhikary, A. Dehzangi, and M. Razeghi, “Mid-wavelength infrared heterojunction phototransistors based on type-II InAs/AlSb/GaSb superlattices,” *Applied Physics Letters*, vol. 109, no. 2, pp. 021107, 2016.

[32] S. E. Keuleyan, P. Guyot-Sionnest, C. Delerue, and G. Allan, “Mercury telluride colloidal quantum dots: Electronic structure, size-dependent spectra, and photocurrent detection up to 12 μm,” *ACS Nano*, vol. 8, no. 8, pp. 8676–8682, 2014.

[33] P. G-Sionnest and J. A. Roberts, “Background limited mid-infrared photodetection with photovoltaic HgTe colloidal quantum dots,” *Applied Physics Letters*, vol. 107, no. 25, pp. 253104, 2015.

[34] Z. Deng, K. S. Jeong, and P. Guyot-Sionnest, “Colloidal quantum dots intraband photodetectors,” *ACS Nano*, vol. 8, no. 11, pp. 11707–11714, 2014.

[35] E. Lhuillier, M. Scarafagio, P. Hease, B. Nadal, H. Aubin, X. Z. Xu, N. Lequeux, G. Patriarche, S. Ithurria, and B. Dubertret, “Infrared photodetection based on colloidal quantum-dot films with high mobility and optical absorption up to THz,” *Nano Letters*, vol. 16, no. 2, pp. 1282-1286, 2016.

[36] S. Keuleyan, E. Lhuillier, V. Brajuskovic, and P. Guyot-Sionnest, “Mid-infrared HgTe colloidal quantum dot photodetectors,” *Nature Photonics*, vol. 5, no. 8, pp. 489-493, 2011.

[37] E. Lhuillier, S. Keuleyan, P. Rekemeyer, and P. Guyot-Sionnest, “Thermal properties of mid-infrared colloidal quantum dot detectors,” *Journal of Applied Physics*, vol. 110, no. 3, pp. 033110, 2011.

[38] S. Keuleyan, E. Lhuillier, and P. Guyot-Sionnest, “Synthesis of colloidal HgTe quantum dots for narrow mid-IR emission and detection,” *Journal of the American Chemical Society*, vol. 133, no. 41, pp. 16422–16424, 2011.

[39] E. Lhuillier, S. Keuleyan, P. Zolotavin, and P. Guyot-Sionnest, “Mid-infrared HgTe/As2S3 field effect transistors and photodetectors,” *Advanced Materials*, vol. 25, no. 1, pp. 137–141, 2013.

[40] E. Lhuillier, S. Keuleyan, H. Liu, and P. Guyot-Sionnest, “Mid-IR colloidal nanocrystals,” *Chemistry of Materials*, vol. 25, no. 8, pp. 1272–1282, 2013.

[41] X. Tang, X. Tang, and K. W. C. Lai, “Scalable fabrication of infrared detectors with multispectral photoresponse based on patterned colloidal quantum dot films,” *ACS Photonics*, vol. 3, no. 12, pp. 2396–2404, 2016.

[42] M. E. Cryer and J. E. Halpert, “300 nm Spectral Resolution in the Mid-Infrared with Robust, High responsivity flexible colloidal quantum dot devices at room temperature,” *ACS Photonics*, vol. 5, no. 8, pp. 3009–3015, 2018.

[43] A. J. Ciani, R. E. Pimpinella, C. H. Grein, and P. Guyot-Sionnest, “Colloidal quantum dots for low-cost MWIR imaging,” *Proceeding of SPIE: Infrared Technology and Applications XLII*, vol. 9819, pp. 981919, 2016.

[44] C. Buurma, A. J. Ciani, R. E. Pimpinella, J. S. Feldman, C. H. Grein, and P. Guyot-Sionnest, “Advances in HgTe Colloidal quantum dots for infrared detectors,” *Journal of Electronic Materials*, vol. 46, no. 11, pp. 6685–6688, 2017.

[45] Y. Yifat, M. Ackerman, and P. Guyot-Sionnest, “Mid-IR colloidal quantum dot detectors enhanced by optical nano-antennas,” *Applied Physics Letters*, vol. 110, no. 4, pp. 041106, 2017.

[46] M. H. Hudson. M. Chen, V. Kamysbayev, E. M. Janke, X. lan, G. Allan, C. Delerue, B. Lee, P. Guyot-Sionnest, and D. V. Talapin, “Conduction band fine structure in colloidal HgTe quantum dots,” *ACS Nano*, vol. 12, no. 9, p. 9397-9404, 2018.

[47] W. E. Tennant, D. Lee, M. Zandian, E. Piquette, and M. Carmody, “MBE HgCdTe technology : A very general solution to IR detection , described by "Rule 07", a very convenient heuristic,” *Journal of Electronic Materials*, vol. 37, no. 9, pp. 1406–1410, 2008.

[48] M. M. Ackerman, X. Tang, and P. Guyot-Sionnest, “Fast and sensitive colloidal quantum dot mid-wave infrared photodetectors,” *ACS Nano*, vol. 12, no. 7, pp. 7264–7271, 2018.

[49] X. Tang, M. M. Ackerman, and P. Guyot-Sionnest, “Thermal imaging with plasmon resonance enhanced HgTe colloidal quantum dot photovoltaic devices,” *ACS Nano*, vol. 12, no. 7, pp. 7362–7370, 2018.

[50] A. Robin, C. Livache, S. Ithurria, E. Lacaze, B. Dubertret, and E. Lhuillier, “Surface control of doping in self-doped nanocrystals,” *ACS Applied Materials and Interfaces*, vol. 8, no. 40, pp. 27122–27128, 2016.

[51] B. Martinez, C. livache, E. Meriggio, X. Z. Xu, H. Cruguel, E. Lacaze, A. Proust, S. Ithurria, M. G. Silly, G. Cabailh, F. Volatron, and E. Lhuillier, “Polyoxometalate as control agent for the doping in HgSe self-doped nanocrystals,” *Journal of Physical Chemistry C*, vol. 122, no. 46, pp. 26680-26685, 2018.

[52] C. Livache, B. Martinez, A. Robin, N. Goubet, B. Dubertret, H. Wang, S. Ithurria, H. Aubin, and E. Lhuillier, “Investigation of the self-doping process in HgSe nanocrystals,” *Physica Status Solidi (A)*, vol. 215, no. 3, pp. 17700294, 2018.

[53] N. Goubet, C. Livache, B. Martinez, X. Z. Xu, S. Ithurria, S. Royer, H. Cruguel, G. Patriarche, A. Ouerghi, M. Silly, B. Dubertret, and E. Lhuillier, "Wave-function engineering in HgSe/HgTe colloidal heterostructures to enhance mid-infrared photoconductive properties," *Nano Letters*, vol. 18, no. 7, pp. 4590–4597, 2018.

[54] Z. Deng and P. Guyot-Sionnest, "Intraband luminescence from HgSe/CdS core/shell quantum dots," *ACS Nano*, vol. 10, no. 2, pp. 2121-2127, 2016.

[55] L. K. Sagar, W. Walravens, J. Maes, P. Geiregat, and Z. Hens, "HgSe/CdE (E = S, Se) core/shell nanocrystals by colloidal atomic layer deposition," *Journal of Physical Chemistry C*, vol. 121, no. 25, pp. 13816–13822, 2017.

[56] X. Tang, G. fu Wu, and K. W. C. Lai, "Plasmon resonance enhanced colloidal HgSe quantum dot filterless narrowband photodetectors for mid-wave infrared," *Journal of Materials Chemistry C*, vol. 5, no. 2, pp. 362-369, 2017.

[57] S. B. Hafiz, M. R. Scimeca, A. Sahu, and D.-K. Ko, Colloidal quantum dots for thermal infrared sensing and imaging," *Nanoconvergence*, vol. 6, no. 7, pp. 1-22, 2019.

[58] P. Martyniuk and A. Rogalski, "HOT infrared photodetectors," *Opto-Electronics Review*, vol. 21, no. 2, pp. 239-257, 2013.

[59] J. Piotrowski, J. Pawluczyk, A. Piotrowski, W. Gawron, M. Romanis, and K. Kłos, "Uncooled MWIR and LWIR photodetectors in Poland," *Opto-Electronics Review*, vol. 18, no. 3, pp. 318-327, 2010.

[60] C. Melnychuk and P. Guyot-Sionnest, "Auger suppression in n-Type HgSe colloidal quantum dots," *ACS Nano*, vol. 13, no. 9, pp. 10512-10519, 2019.

[61] G. Konstantatos and E. H. Sargent, "Solution-processed quantum dot photodetectors," *Proceedings of the IEEE*, vol. 97, no. 10, pp. 1666-1683, 2009.

[62] V. K. Lamer and R. H. Dinegar, "Theory, production and mechanism of formation of monodispersed hydrosols," *Journal of the American Chemical Society*, vol. 72, no. 11, pp. 4847-4854, 1950.

[63] C. Murray, D. Norris, and M. Bawendi, "Synthesis and characterization of nearly monodisperse CdE (E=sulfur, selenium, tellurium) semiconductor nanocrystallites," *Journal of the American Chemical Society*, vol. 115, no. 4, pp. 8706-8715, 1993.

[64] S. Tamang, C. Lincheneau, Y. Hermans, S. Jeong, and P. Reiss, "Chemistry of InP nanocrystal syntheses," *Chemistry of Materials*, vol. 28, no. 8, pp. 2491-2506, 2016.

[65] D. Wang, T. Xie, Q. Peng, and Y. Li, "Ag, Ag2S, and Ag2Se nanocrystals: Synthesis, assembly, and construction of mesoporous structures," *Journal of the American Chemical Society*, vol. 130, no. 12, pp. 4016-4022, 2008.

[66] M. Yarema, S. Pichler, M. Sytnyk, R. Seyrkammer, R. T. Lechner, G. Fritz-Popovski, D. Jarzab, K, Szendrei, R. Resel, O. Korovyanko, M. A. Loi, O. Paris, G. Hesser, and W. Heiss, "Infrared emitting and photoconducting colloidal silver chalcogenide nanocrystal quantum dots from a silylamide-promoted synthesis," *ACS Nano*, vol. 5, no. 5, pp. 3758–3765, 2011.

[67] A. Sahu, A. Khare, D. D. Deng, and D. J. Norris, "Quantum confinement in silver selenide semiconductor nanocrystals," *Chemical Communications*, vol. 48, no. 44, pp. 5458–5460, 2012.

[68] O. Madelung, U. Rössler, M. Schulz, *Non-Tetrahedrally Bonded Elements and Binary Compounds I*, Berlin, Heidelberg: Springer-Verlag, 1998.

[69] A. Sahu, D. Braga, O. Waser, M. S. Kang, D. Deng, and D. J. Norris, "Solid-phase flexibility in Ag2Se semiconductor nanocrystals," *Nano Letters*, vol. 14, no. 1, pp. 115-121, 2014.

[70] R. Dalven and R. Gill, "Energy gap in β-Ag2Se," *Physical Review*, vol. 159, no. 3, pp. 645-649, 1967.

[71] A. G. Abdullayev, R. B. Shafizade, E. S. Krupnikov, and K. V. Kiriluk, "Phase formation and kinetics of the phase transition in Ag2Se thin films," *Thin Solid Films*, vol. 106, no. 3, pp. 175–184, 1983.

[72] S. B. Hafiz, M. R. Scimeca, A. Sahu, and D.-K. Ko, "Mid-infrared colloidal quantum dot based nanoelectronics and nano-optoelectronics," *ECS Transactions*, vol. 92, no 1, p. 11-16, 2019.

[73] M. Park, D. Choi, Y. Choi, H. B. Shin, and K. S. Jeong, "Mid-infrared intraband transition of metal excess colloidal Ag_2Se nanocrystals," *ACS Photonics*, vol. 5, no. 5, pp. 1907–1911, 2018.

[74] D.-K. Ko and C. B. Murray, "Probing the fermi energy level and the density of states distribution in PbTe nanocrystal (Quantum Dot) solids by temperature-dependent thermopower measurements," *ACS Nano*, vol. 5, no. 6, pp. 4810-4817, 2011.

[75] D.-K. Ko, J. J. Urban, and C. B. Murray, "Carrier distribution and dynamics of nanocrystal solids doped with artificial atoms," *Nano Letters*, vol. 10, no. 5, pp. 1842-1847, 2010.

[76] J. Qu, N. Goubet, C. Livache, B. Martinez, D. Amelot, C. Greboval, A. Chu, J. Ramade, H. Cruguel, S. Ithurria, M. G. Silly, and E. Lhuillier, "Intraband mid-infrared transitions in Ag_2Se nanocrystals: potential and limitations for Hg-free low-cost photodetection," *Journal of Physical Chemistry C*, vol. 122, no. 31, pp. 18161-18167, 2018.

[77] Y. Liu, M. Gibbs, J. Puthussery, S. Gaik, R. Ihly, H. W. Hillhouse, and M. Law, "Dependence of carrier mobility on nanocrystal size and ligand length in PbSe nanocrystal solids," *Nano Letters*, vol. 10, no. 5, pp. 1960-1969, 2010.

[78] P. Guyot-Sionnest, “Electrical transport in colloidal quantum dot films,” *Journal of Physical Chemistry Letters*, vol. 3, no. 9. pp. 1169-1175, 2012.

[79] J. A. Dahl, B. L. S. Maddux, and J. E. Hutchison, “Toward greener nanosynthesis,” *Chemical Reviews*, vol. 107, no. 6. pp. 2228–2269, 2007.

[80] Y. Zhang, D. J. Hellebusch, N. D. Bronstein, C. Ko, D. F. Ogletree, M. Salmeron, and A. P. Alivisatos, “Ultrasensitive photodetectors exploiting electrostatic trapping and percolation transport,” *Nature Communications*, vol. 7, pp. 11924, 2016.

[81] G. Konstantatos, I. Howard, A. Fischer, S. Hoogland, J. Clifford, E. Klem, L. Levina, and E. H. Sargent, “Ultrasensitive solution-cast quantum dot photodetectors,” *Nature*, vol. 442, no. 7099, pp. 180–183, 2006.

[82] J. M. Luther, M. Law, Q. Song, C. L. Perkins, M. C. Beard, and A. J. Nozik, “Structural, optical, and electrical properties of self-assembled films of PbSe nanocrystals treated with 1,2-ethanedithiol,” *ACS Nano*, vol. 2, no. 2, pp. 271-280, 2008.

[83] E. J. D. Klem, H. Shukla, S. Hinds, D. D. MacNeil, L. Levina, and E. H. Sargent, “Impact of dithiol treatment and air annealing on the conductivity, mobility, and hole density in PbS colloidal quantum dot solids,” *Applied Physics Letters*, vol. 92, no. 21, pp. 212105, 2008.

[84] X. Tang and K. W. C. Lai, “Detection of mid-infrared by HgTe colloidal quantum dots at room temperature,” *Proceedings of the 16th International Conference on Nanotechnology-IEEE NANO*, pp. 494–497, 2016.

[85] J. Phillips, “Evaluation of the fundamental properties of quantum dot infrared detectors,” *Journal of Applied Physics*, vol. 91, no. 7, pp. 4590–4594, 2002.

[86] S. B. Hafiz, M. R. Scimeca, P. Zhao, I. J. Paredes, A. Sahu, and D. K. Ko, “Silver selenide colloidal quantum dots for mid-wavelength infrared photodetection,” *ACS Applied Nano Materials*, vol. 2, no. 3, pp. 1631-1636, 2019.

[87] S.-A. Gopalan, M.-H. Seo, G.A. -Iyengar, B. Han, S.-W. Lee, D.-H. Kwon, S.-H. Lee, S.-W. Kang, "Mild wetting poor solvent induced hydrogen bonding interactions for improved performance in bulk heterojunction solar cells,” *Journal of Materials Chemistry A*, vol. 2, no. 7, pp. 2174-2186, 2014.

[88] J. Maibach, E. Mankel, T. Mayer, and W. Jaegermann, “The band energy diagram of PCBM-DH6T bulk heterojunction solar cells: Synchrotron-induced photoelectron spectroscopy on solution processed DH6T:PCBM blends and in situ prepared PCBM/DH6T interfaces,” *Journal of Materials Chemistry C*, vol. 1, no. 45, pp. 7635-7642, 2013.

[89] D. S. Chung, Y. H. Kim, and J. S. Lee, “Achieving high sensitivity in hybrid photodetectors based on an organic single crystal and an inorganic nanocrystal array,” *Nanotechnology*, vol. 25, no. 3, pp. 035202, 2014.

[90] D. V. Talapin, J. S. Lee, M. V. Kovalenko, and E. V. Shevchenko, “Prospects of colloidal nanocrystals for electronic and optoelectronic applications,” *Chemical Reviews*, vol. 110, no. 1, pp. 389-458, 2010.

[91] K.S. Jeong, J. Tang, H. Liu, J. Kim, A. Schaefer, K. Kemp, L. Levina, X. Wang, S. Hoogland, R. Debnath, L. Brzozowski, E. H. Sargent, and J. B. Asbury, "Enhanced mobility-lifetime products in PbS colloidal quantum dot photovoltaics,” *ACS Nano*, vol. 6, no. 1, pp. 89-99, 2012.

[92] E. Lhuillier, S. Keuleyan, and P. Guyot-Sionnest, “Optical properties of HgTe colloidal quantum dots,” *Nanotechnology*, vol. 23, no. 17, pp. 175705, 2012.

[93] C. R. Kagan, “Flexible colloidal nanocrystal electronics,” *Chemical Society Reviews*, vol. 48, no. 6. pp. 1626-1641, 2019.

[94] D. Emin, “The sign of the Hall effect in hopping conduction,” *Philosophical Magazine*, vol. 35, no. 5, pp. 1189-1198, 1977.

[95] N. F. Mott, “The sign of the Hall effect in amorphous silicon,” *Philosophical Magazine B*, vol. 63, no. 1, pp. 1-3, 1991.

[96] F. Werner, “Hall measurements on low-mobility thin films,” *Journal of Applied Physics*, vol. 122, no. 13, pp. 135306, 2017.

[97] X. Lan, M. Chen, M. H. Hudson, V. Kamysbayev, Y. Wang, P. Guyot-Sionnest, and D. V. Talapin, “Quantum dot solids showing state-resolved band-like transport,” *Nature Materials*, vol 19, no. 3, pp. 323-329, 2020.

[98] J. S. Lee, M. V. Kovalenko, J. Huang, D. S. Chung, and D. V. Talapin, “Band-like transport, high electron mobility and high photoconductivity in all-inorganic nanocrystal arrays,” *Nature Nanotechnology*, vol. 6, no. 6, pp. 348-352, 2011.

[99] J. -H. Choi, A. T. Fafarman, S. J. Oh, D.-K. Ko, D. K. Kim, B. T. Diroll, S. Muramoto, J. G. Gillen, C. B. Murray, C. R. Kagan, “Bandlike transport in strongly coupled and doped quantum dot solids: A route to high-performance thin-film electronics,” *Nano Letters*, vol. 12, no. 5, pp. 2631-2638, 2012.

[100] B. Martinez, C. Livache, N, Goubet, A. Jagtap, H. Cruguel, A. Ouerghi, E. Lacaze, M. G. silly, and E. Lhuillier, “Probing charge carrier dynamics to unveil the role of surface ligands in HgTe narrow band gap nanocrystals,” *Journal of Physical Chemistry C*, vol. 122, no. 1, pp. 859-865, 2018.

[101] M. V. Kovalenko, M. Scheele, and D. V. Talapin, “Colloidal nanocrystals with molecular metal chalcogenide surface ligands,” *Science*, vol. 324, no. 5933, pp. 1417-1420, 2009.

[102] J. Jang, D. S. Dolzhnikov, W. Liu, S. Nam, M. Shim, and D. V. Talapin, “Solution-processed transistors using colloidal nanocrystals with composition-matched molecular ‘solders’: approaching single crystal mobility,” *Nano Letters*, vol. 15, no. 10, pp. 6309-6317, 2015.

[103] G. Konstantatos and E. H. Sargent, "PbS colloidal quantum dot photoconductive photodetectors: Transport, traps, and gain," *Applied Physics Letters*, vol. 91, no. 17, pp. 1735005, 2007.

[104] J. Tang, K. W. Kemp, S. Hoogland, K. S. Jeong, H. Liu, L. Levina, M. Furukawa, X. Wang, R. Debnath, D. Cha, K. W. Chou, A. Fischer, A. Amassian, J. B. asbury, and, E. H. Sargent, "Colloidal-quantum-dot photovoltaics using atomic-ligand passivation," *Nature Materials*, vol. 10, no. 10, pp. 765-771, 2011.

[105] D.-K. Ko, A. Maurano, S. K. Suh, D. Kim, G. W. Hwang, J. C. Grossman, V. Bulovic, and M. Bawendi, "Photovoltaic performance of PbS quantum dots treated with metal salts," *ACS Nano*, vol. 10, no. 3, pp. 3382-3388, 2016.

[106] D. M. Balazs, D. N. Dirin, H.-H. Fang, L. Protesescu, G. H. T. Brink, B. J. Kooi, M. V. Kovalenko, and M. A. Loi, "Counterion-mediated ligand exchange for PbS colloidal quantum dot superlattices," *ACS Nano*, vol. 9, no. 12, pp. 11951-11959, 2015.

[107] W. Walravens, J. D. Roo, E. Drijvers, S. T. Brinck, E. Solano, J. Dendooven, C. Detavernier, I. Infante, and Z. Hens, "Chemically triggered formation of two-dimensional epitaxial quantum dot superlattices," *ACS Nano*, vol. 10, no. 7, pp. 6861-6870, 2016.

[108] K. Somogyi and G. Sáfrán, "Mobility variations in semiconducting Ag_2Se layers," *Vacuum*, vol. 46, no. 8–10, pp. 1055-1058, 1995.

[109] Y. Ding, Y. Qiu, K. Cai, Q. Yao, S. Chen, L. Chen, and J. He, "High performance n-type Ag_2Se film on nylon membrane for flexible thermoelectric power generator," *Nature Communicantions.*, vol. 10, no. 1, pp. 841, 2019.

[110] D. A. R. Barkhouse, A. G. Pattantyus-Abraham, L. Levina, and E. H. Sargent, "Thiols passivate recombination centers in colloidal quantum dots leading to enhanced photovoltaic device efficiency," *ACS Nano*, vol. 2, no. 11, pp. 2356-2362, 2008.

[111] A. H. Ip, S. M. Thon, S. Hoogland, O. Voznyy, D. Zhitomirsky, R. Debnath, L. Levina, L. R. Rollny, G. H. Carey, A. Fischer, K. W. Kemp, I. J. Kramer, Z. Ning, A. J. Labelle, K. W. Chou, A. Amassian, and E. H. Sargent, "Hybrid passivated colloidal quantum dot solids," *Nature Nanotechnology*, vol. 7, no. 9, pp. 577-582, 2012.

[112] M. Chen, G. Shen, and P. Guyot-Sionnest, "Size distribution effects on mobility and intraband gap of HgSe quantum dots," *Journal of Physical Chemistry C*, vol. 124, no. 29, pp. 16216–16221, 2020.

[113] P. Martyniuk, M. Kopytko, and A. Rogalski, "Barrier infrared detectors," *Opto-Electronics Review*, vol. 22, no. 2, pp. 127-146, 2014.

[114] A. Evirgen, J. Abautret, J. P. Perez, A. Cordat, A. Nedelcu, and P. Christol, "Midwave infrared InSb nBn photodetector," *Electronics Letters*, vol. 50, no. 20, pp. 1472-1473, 2014.

[115] M. Kopytko, A. Kębłowski, W. Gawron, P. Madejczyk, A. Kowalewski, and K. Jóåwikowski, "High-operating temperature MWIR nBn HgCdTe detector grown by MOCVD," *Opto-Electronics Review*, vol. 21, no. 4, pp. 402-405, 2013.

[116] J. B. Rodriguez, E. Plis, G. Bishop, Y. D. Sharma, H. Kim, L. R. Dawson, and S. Krishna, "NBn structure based on InAs/GaSb type-II strained layer superlattices," *Applied Physics Letters*, vol. 91, no. 4, pp. 053414, 2007.

[117] S. B. Hafiz, M. M. A. Mahfuz, M. R. Scimeca, S. Lee, S. J. Oh, A. Sahu and D.-K. Ko "Ligand engineering of mid-infrared Ag2Se colloidal quantum dots," *Physica E Low-Dimensional Systems and Nanostructures*, vol. 124, pp. 114223, 2020.

[118] D.-K. Ko, P. R. Brown, M. G. Bawendi, and V. Bulovič, "P-i-n heterojunction solar cells with a colloidal quantum-dot absorber layer," *Advanced Mater*ials, vol. 26, no. 28, pp. 4845-4850, 2014.

[119] G. H. Carey, A. L. Abdelhady, Z. Ning, S. M. Thon, O. M. Bakr, and E. H. Sargent, "Colloidal quantum dot solar cells," *Chemical Reviews*, vol. 115, no. 23, pp. 12732-12763, 2015.

[120] S. Pradhan, F. D. Stasio, Y. Bi, S. Gupta, S. Christooulou, A. Stavrinadis, and G. Konstantatos, "High-efficiency colloidal quantum dot infrared light-emitting diodes via engineering at the supra-nanocrystalline level," *Nature Nanotechnology*, vol. 14, no. 1, pp. 72-79, 2019.

[121] C. M. Evans, M. E. Evans, and T. D. Krauss, "Mysteries of TOPSe revealed: Insights into quantum dot nucleation," *Journal of the American Chemical Society*, vol. 132, no. 32, pp. 10973-10975, 2010.

[122] J. S. Steckel, B. K. H. Yen, D. C. Oertel, and M. G. Bawendi, "On the mechanism of lead chalcogenide nanocrystal formation," *Journal of the American Chemical Society*, vol. 128, no. 40, pp. 13032-13033, 2006.

[123] M. A. Hines and G. D. Scholes, "Colloidal PbS nanocrystals with size-tunable near-infrared emission: observation of post-synthesis self-narrowing of the particle size distribution," *Advanced Materials*, vol. 15, no. 21, pp. 1844-1849, 2003.

[124] K.-A. Son, D. Wong, H. Sharifi, H. C. Seo, T. D. Lyon, S. Terterian, J. S. Moon, and T. Hussain, "Silver nanowire-based infrared-transparent contacts for future high-density format focal plane arrays," *IEEE Transactions on Nanotechnology*, vol. 14, no. 1, pp. 10-14, 2015.

[125] R. Zhang and M. Engholm, "Recent progress on the fabrication and properties of silver nanowire-based transparent electrodes," *Nanomaterials*, vol. 8, no. 8, pp. 628, 2018.

[126] Y. Liu, J. Zhang, H. Gao, Y. Wang, Q. Liu, S. Huang, C. F. Guo, and Z. Ren, "Capillary-force-induced cold welding in silver-nanowire-based flexible transparent electrodes," *Nano Letters*, vol. 17, no. 2, pp. 1090-1096, 2017.

[127] J. Jasieniak, M. Califano, and S. E. Watkins, "Size-dependent valence and conduction band-edge energies of semiconductor nanocrystals," *ACS Nano*, vol. 5, no. 7, pp. 5888-5902, 2011.

[128] J. Gao, J. M. Luther, O. E. Semonin, R. J. Ellingson, A. J. Nozik, and M. C. Beard, "Quantum dot size dependent J - V characteristics in heterojunction ZnO/PbS quantum dot solar cells," *Nano Letters*, vol. 11, no. 3, pp. 1002-1008, 2011.

[129] J. Wuesten, C. Ziegler, and T. Ertl, "Electron transport in pristine and alkali metal doped perylene-3,4,9,10- tetracarboxylicdianhydride (PTCDA) thin films," *Physical Review B*, vol. 74, no. 12, pp. 125205, 2006.

[130] W. J. Baumgardner, K. Whitham, and T. Hanrath, "Confined-but-connected quantum solids via controlled ligand displacement," *Nano Letters*, vol. 13, no. 7, pp. 3225-3231, 2013.

[131] T. S. Mentzel, V. J. Porter, S. Geyer, K. MacLean, M. G. Bawendi, and M. A. Kastner, "Charge transport in PbSe nanocrystal arrays," *Physical Review B*, vol. 77, no. 7, pp. 075316, 2008.

[132] D. Yu, C. Wang, B. L. Wehrenberg, and P. Guyot-Sionnest, "Variable range hopping conduction in semiconductor nanocrystal solids," *Physical Review Letters*, vol. 92, no. 21, pp. 216802, 2004.

[133] M. S. Kang, A. Sahu, D. J. Norris, and C. D. Frisbie, "Size- and temperature-dependent charge transport in PbSe nanocrystal thin films," *Nano Letters*, vol. 11, no. 9, pp. 3887-3892, 2011.

[134] S. B. Hafiz, M. M. A. Mahfuz and D.-K. Ko, "Vertically stacked intraband quantum dot devices for mid-wavelength infrared photodetection," *ACS Applied Materials and Interfaces*, vol. 13, no. 1, pp. 937-943, 2021.

[135] M. Chen, X. Lan, X. Tang, Y. Wang, M. H. Hudson, D. V. Talapin, and, P. Guyot-Sionnest, "High carrier mobility in HgTe quantum dot solids improves mid-IR photodetectors," *ACS Photonics*, vol. 6, no. 9, pp. 2358-2365, 2019.

[136] C. Livache, B. Martinez, N, Goubet, C. Greboval, J. Qu, A. Chu, S. Royer, S. Ithurria, M. G. Silly, B. Dubertret, and. E. Lhuillier, "A colloidal quantum dot infrared photodetector and its use for intraband detection," *Nature Communications*, vol. 10, no. 1, pp. 2125, 2019.

[137] B. Streetman, S. Banerjee, *Solid State Electronic Devices*, *Seventh Edition*, Essex, England: Pearson, 2014.

[138] S. B. Hafiz, M. M. A. Mahfuz and D.-K. Ko, "Intraband quantum dot barrier devices - optimization of energy level alignment," *ECS Transactions*, vol. 102, no. 1, pp. 45-51, 2021.

[139] S. M. Sze and K. K. Ng, *Physics of Semiconductor Devices. Third Edition*, Hoboken, NJ: John Wiley and Sons, 2006.

[140] I. Moreels, K. Lambert, D. Smeets, D. D. Muynck, T. Nollet, J. C. Martins, F. Vanhaecke, A. Vantomme, C. Delerue, G. Allan, and Z. Hens, "Size-dependent optical properties of colloidal PbS quantum dots," *ACS Nano*, vol. 3, no. 10, pp. 3023-3030, 2009.

[141] P. R. Brown, R. R. Lunt, N. Zhao, T. P. Osedach, D. D. Wanger, L.-Y. Chang, M. G. Bawendi, and B. Bulovic, "Improved current extraction from ZnO/PbS quantum dot heterojunction photovoltaics using a MoO3 interfacial layer," *Nano Letters*, vol. 11, no. 7, pp. 2955-2961, 2011.

[142] J. Gao, C. L. Perkins, J. M. Luther, M. C. Hanna, H.-Y. Chen, O. E. Semonin, A. J. Nozik, R. J. Ellingson, and M. C. Beard, "N-type transition metal oxide as a hole extraction layer in PbS quantum dot solar cells," *Nano Letters*, vol. 11, no. 8, pp. 3263-3266, 2011.

[143] W. J. E. Beek, M. M. Wienk, M. Kemerink, X. Yang, and R. A. J. Janssen, "Hybrid zinc oxide conjugated polymer bulk heterojunction solar cells," *Journal of Physical Chesmitry B*, vol. 109, no. 19, pp. 9505–9516, 2005.

[144] H. K. Woo, M. S. Kang, T. Park, J. Bang, S. Jeon, W. S. Lee, J. Ahn, G. Cho, D.-K. Ko, Y. Kim, D.-H. ha, and S. J. Oh, "Colloidal-annealing of ZnO nanoparticles to passivate traps and improve charge extraction in colloidal quantum dot solar cells," *Nanoscale*, vol. 11, no. 37, pp. 17498-17505. 2019.

[145] G. Shi, Y. Wang, Z. Liu, L. Han, J. Liu, Y. Wang, K. Lu, S. Chen, X. Ling, Y. Li, S. Cheng, and W. Ma, "Stable and highly efficient PbS quantum dot tandem solar cells employing a rationally designed recombination layer," *Advanced Energy Materials*, vol. 7, no. 15, pp. 1602667, 2017.

[146] P. Martyniuk and A. Rogalski, "Quantum-dot infrared photodetectors: Status and outlook," *Progress in Quantum Electronics*, vol. 32, no. 3–4, pp. 89-120, 2008.

[147] Z. Ye, J. C. Campbell, Z. Chen, E. T. Kim, and A. Madhukar, "InAs quantum dot infrared photodetectors with In0.15Ga0.85As strain-relief cap layers," *Journal of Applied Physics*, vol. 92, no. 12, pp. 7462, 2002.

[148] K. Lefatshe, C. M. Muiva, and L. P. Kebaabetswe, "Extraction of nanocellulose and in-situ casting of ZnO/cellulose nanocomposite with enhanced photocatalytic and antibacterial activity," *Carbohydrate Polymers*, vol. 164, pp. 301-308, 2017.

[149] S. Mahalakshmi, N. Hema, and P. P. Vijaya, "In vitro biocompatibility and antimicrobial activities of zinc oxide nanoparticles (ZnO NPs) prepared by chemical and green synthetic route-a comparative study," *Bionanoscience*, vol. 10, no. 1, pp. 112-121, 2020.

[150] E. Q. B. Macabebe and E. E. Van Dyk, "Parameter extraction from dark current-voltage characteristics of solar cells," *South African Journal of Science*, vol. 104, no. 9–10, pp. 401-404, 2008.

[151] Y. Cheng, M. D. C. Whitaker, R. Makkia, S. Cocklin, V. R. Whiteside, L. A. Bumm, E. A. Smith, K. P. Roberts, P. Hari, and, I. R. Sellers, "Role of defects and surface states in the carrier transport and nonlinearity of the diode characteristics in PbS/ZnO quantum dot solar cells," *ACS Applied Materials and Interfaces*, vol. 9, no. 15, pp. 13269-13277, 2017.

[152] J. M. Shah, Y. L. Li, T. Gessmann, and E. F. Schubert, "Experimental analysis and theoretical model for anomalously high ideality factors (n≫2.0) in AlGaN/GaN p-n junction diodes," *Journal of Applied Physics*, vol. 94, no. 4, pp. 2627, 2003.

[153] D. Zhu, J. Xu, A. N. Noemaun, J. K. Kim, E. F. Schubert, M. H. Crawford, and D. D, Koleske, "The origin of the high diode-ideality factors in GaInN/GaN multiple quantum well light-emitting diodes," *Applied Physics Letters*, vol. 94, no. 8, pp. 081113, 2009.

[154] R. Corkish, M. A. Green, M. E. Watt, and S. R Wenham, *Applied Photovoltaics, Second Edition*, Sterling, VA: Earthscan, 2013.

[155] C. Li, Z. Song, D. Zhao, C. Xiao, B. Subedi, N. Shrestha, M. M. Junda, C. Wang, C.-S. Wang, M. A. Jassim, R. J. Ellingson, N. J. Podraja, K. Zhu, and Y. Yan, "Reducing saturation-current density to realize high-efficiency low-bandgap mixed tin–lead halide perovskite solar cells," *Advanced Energy Materials*, vol. 9, no. 3, pp. 1803135, 2019.

[156] C. M. Proctor and T. Q. Nguyen, "Effect of leakage current and shunt resistance on the light intensity dependence of organic solar cells," *Applied Physics Letters*, vol. 106, no. 8, pp. 083301, 2015.

[157] D. Bederak, D. M. Balazs, N. V. Sukharevska, A. G. Shulka, M. A. Aguye, D. N. Dirin, M. V. Kovalenko, and M. A, Loi, "Comparing halide ligands in PbS colloidal quantum dots for field-effect transistors and solar cells," *ACS Applied Nano Materials*, vol. 1, no. 12, pp. 6882-6889, 2018.

[158] P. C. J. Clark, D. C. J. Neo, R. A. Lazo, A. I. Williamson, I. Pis, S. Nappini, A. A. R. Watt, and W. R. flavell, "Influence of multistep surface passivation on the performance of PbS colloidal quantum dot solar cells," *Langmuir*, vol. 34, no. 30, pp. 8887-8897, 2018.

[159] A. Nag, M. V. Kovalenko, J. S. Lee, W. Liu, B. Spokoyny, and D. V. Talapin, "Metal-free inorganic ligands for colloidal nanocrystals: S2-, HS-, Se2-, HSe-, Te2-, HTe-, TeS32-, OH-, and NH2- as surface ligands," *Journal of the American Chemical Society*, vol. 133, no. 27, pp. 10612–10620, 2011.

[160] A. Chu, C. Greboval, Y. Prado, H. Majjad, C. Delerue, J.-F. Dayen, G. Vincent, and E. Lhuillier, "Infrared photoconduction at the diffusion length limit in HgTe nanocrystal arrays," *Nature Communications*, vol. 12, no. 1, pp. 1794, 2021.